Beam Loss Reduction by Barrier Buckets in the CERN Accelerator Complex

Mihaly Vadai

Submitted in partial fulfillment of the requirements
of the Degree of Doctor of Philosophy

Antennas and Electromagnetics Research Group
School of Electronic Engineering and Computer Science
Queen Mary University of London
Systems Department - Radiofrequency Group
CERN, Geneva

2021

Statement of originality

I, Mihaly Vadai, confirm that the research included within this thesis is my own work or that where it has been carried out in collaboration with, or supported by others, that this is duly acknowledged below and my contribution indicated. Previously published material is also acknowledged below.

I attest that I have exercised reasonable care to ensure that the work is original, and does not to the best of my knowledge break any UK law, infringe any third party's copyright or other Intellectual Property Right, or contain any confidential material.

I accept that the College has the right to use plagiarism detection software to check the electronic version of the thesis.

I confirm that this thesis has not been previously submitted for the award of a degree by this or any other university.

Signature: Mihaly Vadai
Date: 29-01-2021

Details of collaboration and publications

The initial beam tests reported in Section 4.3 were conducted by H. Damerau and myself. My contribution was the control of the new barrier bucket drive that I developed for the studies. Tests carried out later, especially the tests optimising the flatness of the profiles and the tests with moving barriers are only my work.

The beam tests reported in Section 4.4 were conducted in a team due to their complexity by H. Damerau, M. Giovannozzi, A. Huschauer and myself. My main contribution to the practical tests was the expert control of the newly installed barrier bucket RF system.

For section 4.4.5, the logging and initial analysis of the beam loss monitor data was provided by A. Huschauer for our joint publication [1].

Abstract

For a future intensity increase of the fixed-target beam in the accelerator complex at CERN, new techniques to reduce beam loss are required. A major fraction of the losses during extraction of the coasting beam from the PS towards the SPS originate from poorly kicked particles during the Multi-Turn Extraction.

A line density depletion, synchronised with the extraction kickers, decreases these losses significantly when successfully combined with the present extraction scheme involving the transverse splitting of the beam. The Finemet® wide-band cavity recently installed in the PS as a longitudinal feedback kicker was used to generate a so-called barrier bucket, which is utilised to deplete the line density and reduce the losses.

The drive to generate the barrier bucket waveform synchronously with the beam was developed and installed by the radiofrequency cavity as part of these studies. The effectiveness of the combination of the Multi-Turn Extraction and the barrier bucket was evaluated with beam. This manipulation was performed for the first time in a particle accelerator.

The measured data with beam in the CERN PS shows a substantial, up to an order of magnitude beam loss reduction at extraction, even well beyond the standard operational beam intensity. This means that the combination of the Multi-Turn Extraction with the barrier buckets achieves a practically loss-less extraction for the fixed target beam from the PS.

Based on the results of the measurements and simulations with beam, a concept for the synchronisation between the CERN PS and SPS accelerators is also presented to realise the beam loss reduction in future operation.

Author's publications

Portions of the work detailed in this thesis have been presented in international scholarly publications with the author of this report listed as main author, as follows:

- Parts of Chapters 1, 4 and 6 are published in the journal article [1] titled Barrier bucket and transversely split beams for loss-free multi-turn extraction in synchrotrons. Authors: M. Vadai, A. Alomainy, H. Damerau, S. Gilardoni, M. Giovannozzi and A. Huschauer
- Parts related to the low and high energy beam tests without the MTE in Chapters 4 and 6 were published in the peer-reviewed 2019 Journal of Physics Conference Series [2]. Title: Beam manipulations with barrier buckets in the CERN PS. Authors: M. Vadai, A. Alomainy, H. Damerau, S. Gilardoni, M. Giovannozzi and A. Huschauer.
- Parts related to the hardware implementation of Chapters 3 and 6 were presented at the International Particle Accelerator Conference 2019. Title: Barrier Bucket Studies in the CERN PS [3]. Authors as it appears on the paper: M. Vadai, A. Alomainy, H. Damerau.

Acknowledgements

I would like to thank for the opportunity and financial support provided by the CERN Doctoral Student Programme that allowed me to work on this project at CERN.

I would like to thank Queen Mary University of London for the flexibility in the administration of this unusual project and the financial support provided in form of a fee waiver.

I would like to thank both of my supervisors, A. Alomainy and H. Damerau for creating an efficient structure and supporting atmosphere that allowed me to work on the PhD.

I would like to thank the CERN PS Operations team for going the extra mile in fulfilling the requests during the machine development sessions on weekdays and weekends. Special thanks to the colleagues in the SPS island in the CCC to having allowed the preliminary SPS beam tests on the very last day of the proton run before LS2.

I would like to thank M. Giovannozzi and A. Huschauer for the discussions and active participation in the setup and measurements sessions during the high energy beam tests.

This thesis could only be a reality, because while I was working on it I was surrounded by a positive environment of building 864 and the inspiring people working in the ATS sector of CERN. Thanks to all of you for the feedback provided during my presentations and informal chats.

Relocations are exciting, but hardly ever convenient. They are definitely easier with help, so I would like to thank my wife and my family for the support they provided in this and for the continuing support and enthusiasm for the project ever since.

Contents

List of Tables

List of Figures

Chapter 1

Introduction

The CERN hadron accelerator complex consisting of two linear accelerators, seven rings and connecting transfer lines at multiple sites serves a considerable number of physics experiments, as Fig. 1.1 illustrates. Among these are fixed target experiments [4–9] served by the Super Proton Synchrotron (SPS) in the North Area [10]. The beams for these experiments are passing though several accelerators before arriving at their targets. The figure of merit for most experiments is the total number of protons on target, which can be improved by increasing the intensity of the beam. However, such increase is limited by beam losses in the upstream accelerator chain, which the present study intends to reduce.

Section 1.1 summarises the path of the beam to fixed target experiments of the North Area of the SPS and Section 1.2 outlines the proposed method of the loss reduction motivating the studies.

Since the beam loss reduction is to be achieved using a radiofrequency manipulation called the barrier bucket, Section 1.3 gives a brief overview of barrier bucket use cases and implementations in particle accelerators.

The main contributions of the work are listed in Section 1.4 and the structure of the thesis is outlined in Section 1.5.

1.1 Review of the extraction of fixed target beams from the PS

The protons for fixed target experiments served by the SPS follow the path as indicated by the thick lines in Fig. 1.1. The particles start their journey in Linac 2, (Linac 4 from 2020 [11]) accelerated from rest to 50 MeV kinetic energy (160 MeV in Linac 4), being again accelerated in the PS Booster to 1.4 GeV kinetic energy (2.0 GeV from 2021), then extracted to the PS. A further acceleration takes place in the PS up to 14 GeV/c momentum for fixed target beams in the present study.

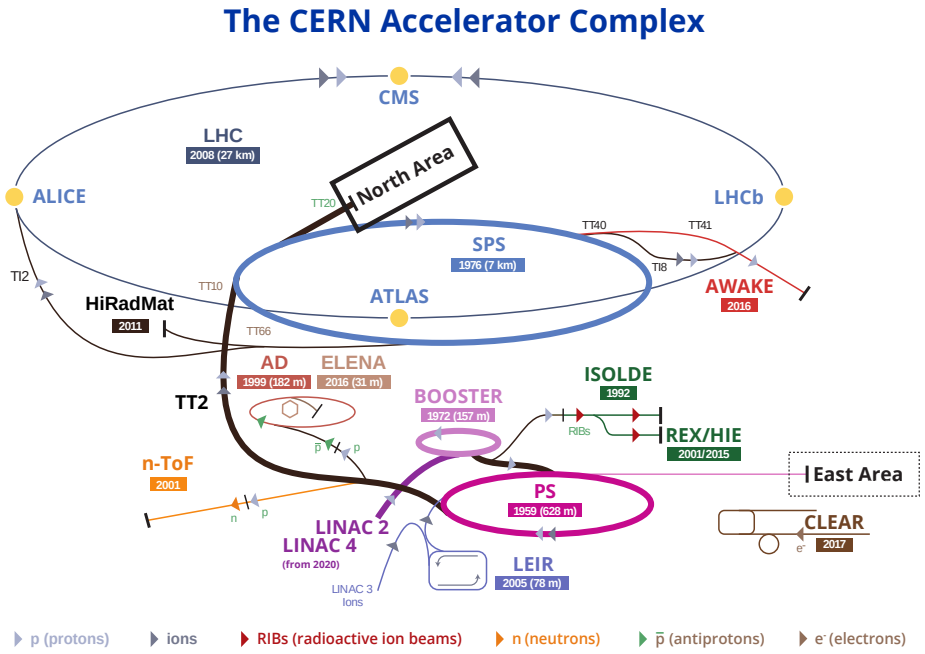

Figure 1.1: The CERN Accelerator Complex. The original image by E. Mobs [12] was simplified and the path of the fixed target beam associated with in these studies was highlighted using thick lines. Copyright CERN.

The main fraction of beam loss happens at the extraction of the fixed target beams from the PS to the SPS. This extraction process occurs in five turns due to the circumference ratio of 1/11 between the synchrotrons, thus two PS cycles are needed to fill the SPS. Extracting the beam in five turns in the PS means that the beam must be cut transversely along the cross-section of the accelerator.

This was first implemented by the Continuous Transfer (CT) [13–15] extraction method, which utilised a physical septum blade to slice the beam and

extract it during five turns. This method, while effective and operated for many years, induced beam losses in several parts of the PS as the beam loss monitor (BLM) readings show in Fig. 1.2. This lead to high activation and reduced lifetime of equipment in the ring.

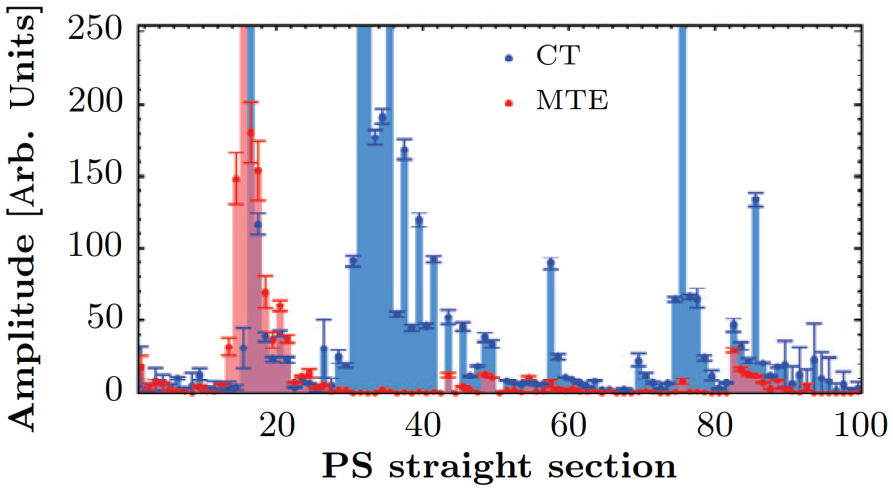

Figure 1.2: The beam loss along the circumference of the PS. The goal of this study is to eliminate the residual losses represented with the red area to improve the performance of the extraction after the implementation of MTE. As a short summary of the results of the present studies, this figure is to be compared with Fig. 4.37, which shows the significantly reduced losses in straight sections 14-18, when the barrier bucket manipulation is added. Present figure taken from [16], Figure 9. Copyright CERN, 2016 CC-BY licence.

To lower these losses, the Multi-Turn Extraction (MTE) method was developed [17]. This operates on the principle of splitting the beam transversely based on a magnetic resonance induced by sextupoles and octopoles [18–20] thereby avoiding the direct contact of the beam with the mechanical septum blade. Thus, the beam loss in the ring has been significantly reduced [16, 18, 21–23] as shown by Fig. 1.2 with the exceptions of straight sections 14-18. This part of the accelerator is what the photo in Fig. 1.3 shows from the fast bumper magnet towards the ejection region in the direction of the beam. During the initial operation of the MTE important localised losses occurred at the extraction septum in SS16 [24]. A dummy septum, a movable absorber [25–29] was therefore installed to protect the blade of the magnetic extraction septum by physically intercepting the particles during the rise time of the kicker dipoles. This interception results in a beam loss in straight sections 14-18, and as a result, the dummy septum becomes highly radioactive.

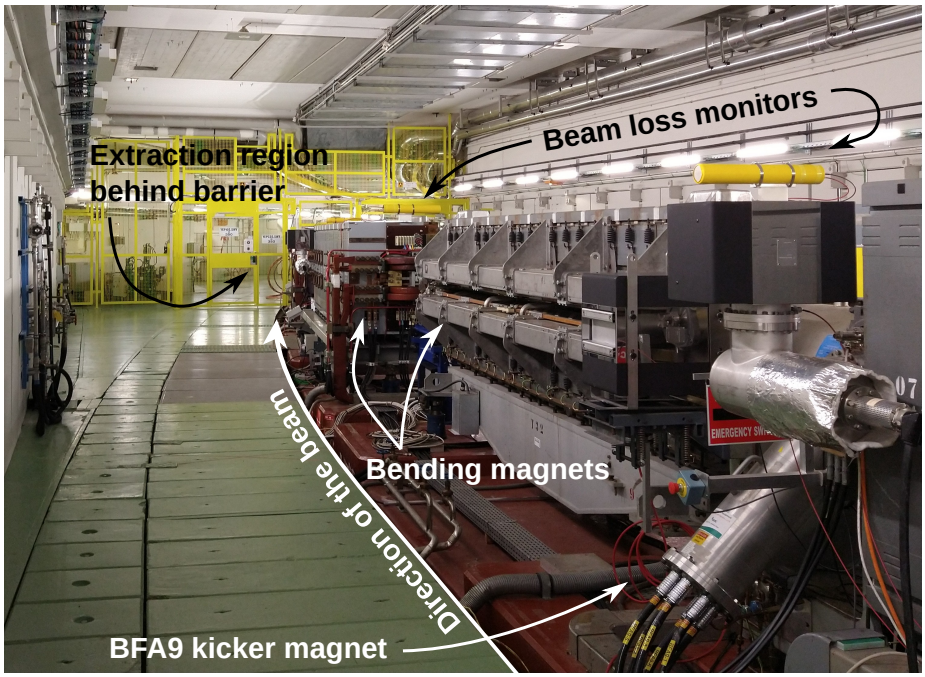

Figure 1.3: The extraction region behind the barrier and the preceding sections seen from the direction of the beam with the last kicker in the foreground. BFA9 is one of the kickers used in the Multi-Turn Extraction. The main PS dipole magnets, two beam loss monitors (BLM) are also indicated. The data from the BLM system was used to evaluate the loss reduction in Chapter 4.

1.2 Motivation

The motivation of the present studies is to significantly reduce this residual beam loss, while maintaining the beneficial properties of the MTE. This goal was achieved at the end of the studies as Fig. 4.37 shows at the end of Chapter 4.

In the spirit of reducing beam losses by avoiding beam interception, a radiofrequency manipulation is proposed to remove particles during the rise time of the kickers from the extraction region by creating a gap in the longitudinal profile. If the length of this gap in time matches this rise time, the extraction losses are reduced virtually to zero. Such a gap can be generated by the means of a so-called barrier bucket. Figure 1.4 illustrates the longitudinal gaps in the beams as a result of the RF manipulation.

1.2.1 RF barrier buckets for loss reduction

Since the beam consists of charged particles, the potential created by RF fields is suitable to confine and accelerate it. These containers for the beam of charged

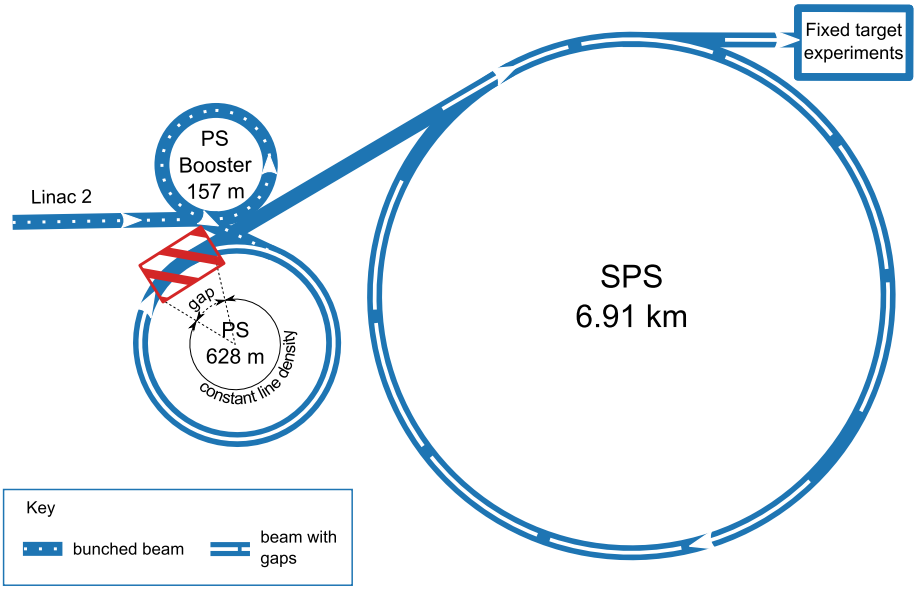

Figure 1.4: Illustration of the beam loss reduction scheme. Gaps are generated in the coasting beam in the PS with upstream and downstream accelerator connections. The diagram only shows parts of the CERN injector chain and it is not to scale.

particles created by the RF systems are called radiofrequency buckets, which cover areas in the longitudinal phase space with closed trajectories, hence particles are trapped in them. These buckets are normally created using sinusoidal pulses and are used for particle acceleration and elaborate RF manipulations [30]. Chapter 2 elaborates on the longitudinal beam dynamics in radiofrequency buckets further which is necessary to introduce the RF manipulations. An isolated sine pulse as further detailed in Chapters 2 and 3 can generate a long, flat stable region for the beam called a barrier bucket. A wide-band radiofrequency system is required to generate such pulses at the accelerating gap of a cavity.

Such a wide-band cavity has been installed in the PS accelerator in 2014 [31]. The cavity is filled with the Finemet® [32] material which makes it usable in from frequency range 400 kHz to about 10 MHz. Its frequency range makes this cavity and its power system ideal to generate barrier buckets. Chapter 3 describes the requirements for the scheme.

Although the cavity and the power amplifiers were installed in the ring already [33], the low power level signal generation was not suitable to produce pulses for the barrier buckets. A new low-level RF system was therefore developed as part of these studies.

1.3 Overview of barrier buckets in synchrotrons

Lengthening the stable phase region of ordinary buckets employing multi-harmonic RF systems has been studied since the early 1960s [34]. The suggestion was to extend the phase stable region in a radiofrequency bucket by using multi-harmonic RF systems to nearly a full accelerator turn to reduce space charge effects, which limit the beam intensity in low energy accelerators. The extreme case of a long bucket, formed by a potential barrier was called barrier bucket in the early 1980s [35].

1.3.1 Use cases of barrier buckets

With the increased availability of wide-band RF systems, barrier buckets [36] became a routine operation at many facilities, first at Fermilab [35, 36] where multiple injection schemes [37, 38] involving moving barriers were studied and used for the accumulation of intense beams [39, 40]. The creation of flat bunches was improved with the development of RF systems [41–43] reaching even longitudinal profiles [44]. Early barrier bucket studies were also performed in the Brookhaven AGS in collaboration with KEK to accumulate a debunched beam [45–49]. In the framework of the AGS studies the use of both, conventional ferrite-loaded cavities and Finemet® cavities was validated [50–55] providing an important milestone to enable the present studies.

Low emittance beamlets at a well defined momentum can be extracted in a process called longitudinal momentum mining [39, 56, 57]. Associated with this operation a unique feature of the beam dynamics in square wave barriers [58] was explored, which highlights the importance of smooth waveforms in barrier bucket generation.

To overcome the limitation of low synchrotron frequencies, which makes an adiabatic bunch length changes slow, shock compression benefiting from space charge was also proposed [59, 60].

Barrier buckets found one of their main use case in low energy storage rings, where high intensity beams need to be kept for longer durations. In particular heavy ion facilities, where space charge effects are dominant have become reliant on this RF structure, see for example [61–64] and references therein. Barrier buckets are often combined with stochastic cooling to compensate for the mean energy loss [65] after the interaction with the target [66–78] and mitigate against electron cloud build up [79]. Preparatory studies for the FAIR accelerator complex for barrier buckets with stochastic cooling were performed at COSY [80–84]. In the ESR at GSI barrier buckets were also experimentally tested to ac-

cumulate multiple injections. The NICA collider, currently in its final phase of its construction [85–92] will also accumulate beam in barrier buckets.

Accelerating beam in barrier buckets is a challenging task. It was proposed and studied in detail at the KEK PS [93–103].

The feasibility of a super-bunch hadron collider [104, 105] was also explored. The super-bunch collider is an induction synchrotron concept [106], where wide-band induction devices for acceleration and beam confinement separately would be used. Such a device, the Finemet® cavity generates barrier buckets in the present studies, too.

Thick barrier buckets using narrow band RF systems were studied in the CERN SPS [107, 108].

1.3.2 Brief overview of barrier bucket implementations

Two main strategies can be employed to generate barrier bucket waveforms, which depend on the shape of the pulse they generate. The waveforms are further compared in Chapter 3 in detail.

The frequency domain approach is to use multiple harmonics [35]. This is well suited to isolated sinusoidal shaped pulses, since these have lower bandwidth requirement compared to isolated square waves. Arbitrary waveform generators [41, 109–111] are also typically employed to generate barrier buckets. Custom waveform generators in programmable logic [44, 112, 113] are also a typical approach, especially when great flexibility is needed. The present study uses the latter for reasons detailed in Chapter 3.

Isolated square pulses generate a higher bucket area for the same pulse duration and peak voltage compared to the sine, at the expense of a higher bandwidth. These can be generated either via the arbitrary waveform generation method, but via a pulsed power modulator [93, 114–118] as a waveform generator.

A common problem in barrier bucket systems is the distortion of the wide band pulse as it is transmitted through the high power system [119] to the cavity gap. Therefore an important part of the implementation of the waveform generator is a compensation method for the non-linear transfer characteristics, such that the desired shape appears at the cavity gap. For this, the modelling of the high power level RF system is essential. Linear models can compensate [109, 119] around a well defined working point reasonably well. If the working point or the system behaviour changes more significantly, adding a feedback system could improve the quality of the waveforms at the cavity gap [44]. Non-linear models [110, 120, 121] are needed if the cavity behaviour is time and power dependent to a larger degree. In addition, in the case of an integrated analogue

solution, the transfer characteristics have to be sufficiently linearised [114]. Since the behaviour of the cavity in the CERN PS does not change with time or beam intensity in a significant way, a linear approach was sufficient for the present implementation as shown in Chapter 3.

1.4 Main contributions

The barrier bucket manipulation is daily routine in many accelerators as described in the previous section. The MTE is a standard operational technique of extracting beams from the PS. However, the combination of both sophisticated beam manipulations, the barrier bucket with transversely split beams was performed for the first time as the part of these studies [1].

The combination showed that the barrier bucket preserved the transverse beam quality, which is not trivial since the transverse and longitudinal beam dynamics are not necessarily decoupled in all cases. This result has an important practical consequence, since the combined beam manipulation can achieve a virtually loss-less extraction of fixed target beams from the PS.

In order to achieve these results, an electronic design for the barrier bucket drive was conceived, implemented and commissioned in the lab and with beam first as part of these studies. This included the development of the concept and writing the firmware for a field programmable gate array (FPGA). Developing a waveform generation method with a smoothing scheme was important to avoid the consequences of a discontinuous waveform on the beam dynamics in narrow barrier buckets [58], produce a flatter waveform and limit the bandwidth.

The studies in this thesis show that a significant beam loss reduction in the PS can be achieved by using barrier buckets at extraction.

For the fixed target experiments to benefit from this, the barrier bucket generation has to be synchronous with the circulating beam in the SPS. A concept is developed in Chapter 5 supported by analytical calculations and benchmarked macroparticle simulations. It is also shown that the conventional adiabaticity criterion based on the change of the synchrotron frequency can not be applied in all cases to the re-phasing operation, which is a central part of the synchronisation, instead, a different criterion is developed.

1.5 Structure of the thesis

Chapter 1 The present chapter. Briefly summarises the state of the art in barrier bucket apparatus in particle accelerators. Details the motivations and highlights the contributions of the thesis to this.

Chapter 2 A study of longitudinal beam dynamics was carried out to introduce barrier buckets used in these studies in an analytical way.

Chapter 3 Contains the analysis of the requirements, the development of the concept, the implementation, validation, installation and commissioning of a beam synchronous arbitrary waveform generator for the barrier buckets. Includes details from the publication [3]. The chapter summarises the technical contribution of the work.

Chapter 4 Contains the main contribution of the work. The combination of the barrier buckets with transversely split beams, a first in the field, lead to a proven, significant beam loss reduction at extraction from the PS. Several steps were needed to reach this conclusion, hence this chapter also presents the initial results of the tests with beam. Additionally, it contains longitudinal beam dynamics simulations to explain the main features of the observed beam profiles at extraction. The chapter presents the experimental evidence of the beam loss reduction and includes details from the publications [1, 2].

Chapter 5 In order to put the barrier bucket scheme into operation the generation of the barrier buckets has to be synchronised with the injection of the beam into the SPS. This chapter presents a conceptual design for this synchronisation.

Chapter 6 Summarises the main contributions and outlines the future work related to the barrier bucket studies in the PS.

Appendix A Presents an alternative synthesis method for the barrier waveform from a series of two harmonics at half of the revolution frequency.

Appendix B Contains the location of the firmware and software developed during this project.

Chapter 2

Longitudinal beam dynamics

2.1 Introduction

This chapter provides a brief theoretical background for the contributions of the subsequent chapters. The main purpose is to introduce the basic parameters to describe the motion of charged particles under the influence of a periodic longitudinal electric field. This is needed to understand the fundamental beam dynamics in barrier buckets. Section 2.2 introduces a continuous time approach to solve the non-linear equations of motion of particles in a synchrotron in the longitudinal direction. Section 2.3 applies the concepts outlined in section 2.2 to the case of stationary barrier buckets, which are of central importance in the beam loss reduction. An estimation of emittance growth when the potential barriers are moved is found in Section 2.3.2 which is confirmed by beam tests in Chapter 4.

The particle motion can also be described in discrete time using difference equations. This approach is called (macro-)particle tracking. The techniques used in thesis are summarised in Section 2.4.

Finally, section 2.5 briefly describes different sources of the longitudinal impedance to provide a background to the results of simulations in Chapter 4.

2.2 Continuous time approach

Subsections 2.2.1 and 2.2.2 deal with the description of the mechanical system of classical, relativistic particles circulating in a synchrotron [122]. The treatment is restricted to the longitudinal aspect of the dynamics of particles approximated

as circular motion in the accelerator illustrated by Fig. 2.1 (top). It is assumed that the particles are not interacting with each other or the environment other than with an ideal, arbitrary, radiofrequency (RF) source. Fig. 2.1 (bottom) illustrates two harmonics of the RF voltage. This voltage generates a potential which confines the charged particles of the beam.

2.2.1 Longitudinal phase space

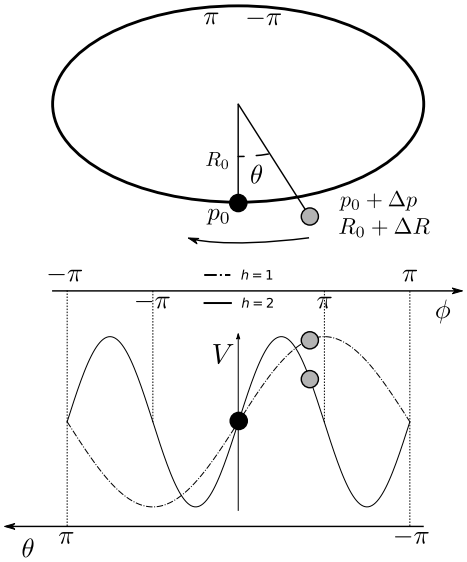

Figure 2.1: Illustration of the azimuth θ, radius R, momentum p and phase ϕ variables. The phase is to be interpreted with respect to the RF voltage for two harmonics: $h = 1$ and $h = 2$ in this example. Note that the phase and azimuth angles are the opposite sign following the usual convention E.g. [123, 124].

The momentum and/or the distribution of the particles along a synchrotron ring is manipulated by RF systems [30, 123, 125] in the longitudinal direction. Since these studies require a wide-band RF waveform, an arbitrary amplitude function $g(\phi)$ is defined following [125]. ω_0 is the angular frequency of the particle moving along a circle with R_0 radius. The multiples of the revolution frequency, $h\omega_0$ are called its harmonics, with h denoting the harmonic number. Figure 2.1 (bottom) illustrates two RF waveforms for $h = 1$ and $h = 2$, with the associated azimuthal position, θ, RF phase, ϕ, with the sign conventions.

The energy change of a particle in a synchrotron is largely due to RF systems. For the particle having E energy, p momentum and q charge, revolving with R radius, the change of energy, ΔE, during one interaction with the RF system is

$$\Delta E = qVg(\phi) \ . \tag{2.1}$$

For a more complete derivation which takes the details of this interaction into account see [124, 125]. To link the energy change, ΔE, to the momentum change, Δp, it is useful to express Δp in the form of the rest energy, m_0c^2,

which is invariant:

$$\Delta p = m_0 c \Delta(\beta\gamma) \rightarrow m_0 c^2 = \frac{c\Delta p}{\Delta(\beta\gamma)} \ , \tag{2.2}$$

where $1/\gamma^2 + \beta^2 = 1$, m_0 is the rest mass of the particle and c is the speed of light in vacuum. The differential change of the relativistic parameters, $\Delta(\beta\gamma)$, with respect to $\Delta\gamma$, see Eqs. 2.2 and 2.4 for the motivation, can be written as

$$\frac{\Delta(\beta\gamma)}{\Delta\gamma} = \frac{\Delta\beta\gamma}{\Delta\gamma} + \frac{\beta\Delta\gamma}{\Delta\gamma} \text{ with } \frac{\Delta\beta}{\Delta\gamma} = \frac{1}{\beta\gamma^3} \rightarrow \frac{\Delta(\beta\gamma)}{\Delta\gamma} = \frac{1}{\beta}\left(\frac{1}{\gamma^2} + \beta^2\right) = \frac{1}{\beta} \ . \tag{2.3}$$

The energy change per revolution becomes using Eq. 2.2 and 2.3:

$$\Delta E = \Delta\gamma m_0 c^2 = \frac{\Delta\gamma}{\Delta(\beta\gamma)} c\Delta p = c\beta\Delta p = \omega R \Delta p \ , \tag{2.4}$$

with $\beta c = v = \omega R$ from the circular motion of the particles in the synchrotron. The average rate of momentum change in time using Eq. 2.1 and 2.4 with the approximation that the change of momentum is small over a revolution period, T, is the following:

$$\frac{\Delta p}{T} = \Delta p \frac{\omega}{2\pi} \approx \frac{dp}{dt} = \frac{qV}{2\pi R} g(\phi) \ . \tag{2.5}$$

One can write 2.5 twice, for two particles, one having parameters with the index 0, called the synchronous particle and another particle with parameters having no index. Multiplying these equations by R and subtracting the equation with 0 index expressions from the other

$$\Delta(R\dot{p}) = \frac{qV}{2\pi}\left[g(\phi) - g(\phi_0)\right] \tag{2.6}$$

is obtained. To the first order $\Delta(R\dot{p}) = d(R_0\Delta p)/dt$ [123]. Then using Eq. 2.4 and 2.6 the first equation of synchrotron motion is obtained:

$$\frac{d}{dt}\left(\frac{\Delta E}{\omega_0}\right) = \frac{qV}{2\pi}\left[g(\phi) - g(\phi_0)\right] \ . \tag{2.7}$$

The particles that have different energies to the synchronous particle arrive at different times from turn to turn. The relative time and angular frequency differences are linked to the relative momentum difference through the phase slip factor, η, which is approximated to the first order as [124, p. 129]:

$$\frac{\Delta\omega}{\omega_0} = -\frac{\Delta T}{T} = -\left(\alpha_c - \frac{1}{\gamma^2}\right)\frac{\Delta p}{p} = -\eta\delta. \tag{2.8}$$

Using the following definitions $\eta = \alpha_c - 1/\gamma^2$, $\alpha_c = 1/\gamma_{\mathrm{tr}}^2$, $\delta = \Delta p/p$. The momentum compaction factor, α_c, and subsequently γ_{tr} is derived from the optics of the ring. The transverse aspects of the particle motion in a synchrotron are out of the scope of this thesis, for further details on α_c see [124, pp. 122–30]. The singularity, when $\alpha_c = 1/\gamma^2$, called transition, is not treated in this thesis, either.

The change of the revolution angular frequency is $\Delta\omega = d\theta/dt = -1/h \;\; d\phi/dt$. The negative sign comes from the definition [123] of the phase with respect to the measurement of azimuth, see Fig. 2.1. Note that this is also in agreement with the definition of the time difference in Eq. 2.8. When the RF waveform is defined for the whole ring, a simplification of $h = 1$ in the equations below can be made. In this case $g(\phi) = g(-\theta)$ as per Fig. 2.1. The equation expressing the change of the phase in time is the following

$$\frac{d\phi}{dt} = \frac{h\omega_0\eta}{pR_0}\left(\frac{\Delta E}{\omega_0}\right) \;, \tag{2.9}$$

which is the second equation of the synchrotron motion. Equations 2.9 and 2.7 can be combined to a single second order differential equation involving ϕ as the single variable assuming a small change for the parameters of the synchronous particle.

$$\frac{d^2\phi}{dt^2} = \frac{h\omega_0\eta qV}{2\pi pR_0}\left[g(\phi) - g(\phi_0)\right] \tag{2.10}$$

The slowly varying machine parameters can be lumped in one term:

$$\zeta = -\frac{h\omega_0\eta qV}{2\pi pR_0} \;. \tag{2.11}$$

Since Eq. 2.10 usually does not have a solution in closed form, it is useful to investigate the types of solutions in two dimensional phase space [126]. This allows to study the stability of the motion even if the exact analytical solution is not known.

An example solution of the two, first order equations 2.7 and 2.9 for the case of $g(\phi) = \sin\phi$ is shown in Fig. 2.2 (bottom) in the ϕ, $\dot{\phi}$ phase space. The set of closed trajectories corresponding to a bounded, stable motion is called the radiofrequency bucket. The points making up the trajectories revolve around a centre in phase space following the evolution of the motion in time. The particle, whose parameters are in the centre of this revolution is the synchronous particle, since it has the phase ϕ_0. It is worth noting that ϕ_0 does not necessarily correspond to a single value, see Section 2.3, but $g(\phi_0)$ obviously does.

Depending on the value of $g(\phi_0)$, three kinds of buckets are defined. In case $g(\phi_0)$ corresponds to an energy increase over a turn for the synchronous particle,

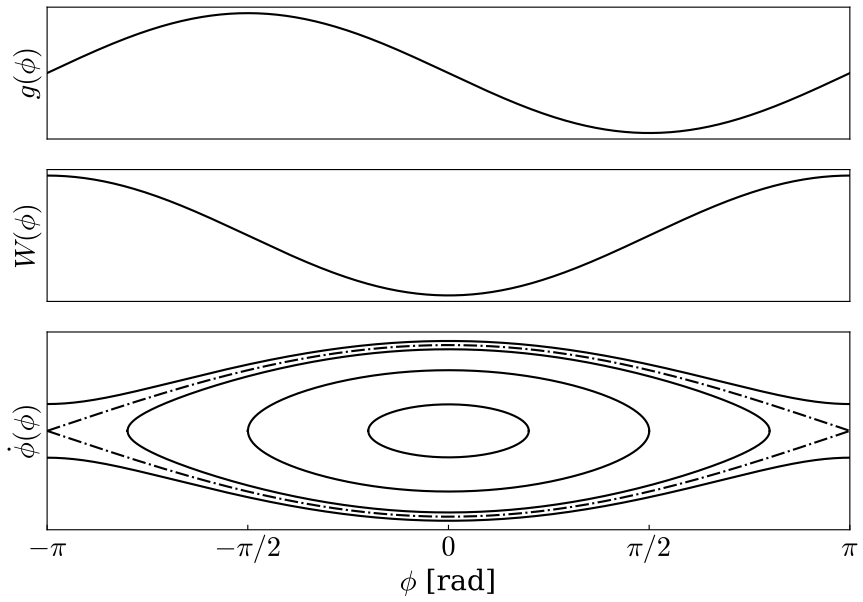

Figure 2.2: Illustration of sinusoidal RF voltage (top), corresponding potential (middle) and a conventional, stationary RF bucket (bottom).

as per Eq. 2.1, then the resulting RF bucket is an accelerating bucket. When $g(\phi_0) = 0$, as seen in Fig 2.2 (bottom), the resulting RF bucket is a stationary bucket. Finally, when $g(\phi_0)$ contributes to an energy decrease over a turn, the RF bucket is a decelerating bucket.

If $g(\phi) = \sin\phi$, then the angular frequency of oscillations of the particles in the centre of the bucket, called the synchrotron frequency, ω_s, can be expressed as:

$$\omega_\mathrm{s}^2 = \zeta \cos\phi_0 = -\frac{h\omega_0 \eta q V \cos\phi_0}{2\pi p R_0} \ . \tag{2.12}$$

One can also describe the system using Hamilton's method with two variables [127, pp. 172–92], which allows an analytical calculation of the revolution periods for all particles in RF buckets. Hamilton's equations for two coordinates are the following [127, p. 167]:

$$\dot{q} = \frac{\partial H}{\partial p}, \quad \dot{p} = -\frac{\partial H}{\partial q} \ , \tag{2.13}$$

where the function $H(p, q)$ is called the Hamiltonian. Using the variables ϕ and $\dot{\phi}$ one can define the following Hamiltonian:

$$H(\phi, \dot{\phi}) = \frac{1}{2}\dot{\phi}^2 + \zeta W(\phi) \ . \tag{2.14}$$

Where the $W(\phi)$ potential is defined as the following:

$$W(\phi) = \int g(\phi)d\phi - g(\phi_0)\phi \tag{2.15}$$

Using Eqs. 2.13 with $p = \dot{\phi}$ and $q = \phi$ one obtains Eq. 2.7 and Eq. 2.9. Figure 2.2 shows $g(\phi)$ on the top, a corresponding $W(\phi)$ in the middle and trajectories in phase space associated with Eq. 2.14 at the bottom. These are obtained from the Hamiltonian formulation by picking a few pairs of values of the coordinates and substituting them to Eq. 2.14. This gives a constant H, corresponding to a constant energy. Then for all values of ϕ, the solution for $\dot{\phi}$ according to

$$\dot{\phi}(\phi) = \pm\sqrt{2\left[H - \zeta W(\phi)\right]}\ , \tag{2.16}$$

can be found, with the condition $H - \zeta W(\phi) > 0$. Note that the same trajectories can be obtained from the Eqs. 2.7 and 2.9. The equation of the separatrix can be obtained from Eq. 2.14 by finding the phase corresponding to the unstable fixed point [126, pp. 168–170], ϕ_{U}. The phase velocity should be zero at this point. Therefore a value $H_0 = H(\phi_U, 0) = \zeta W(\phi_{\mathrm{U}})$ can be calculated. Then using this value the separatrix is obtained by

$$\dot{\phi}(\phi) = \pm\sqrt{2\zeta\left[W(\phi_{\mathrm{U}}) - W(\phi)\right]}\ . \tag{2.17}$$

The bucket half height is the maximum of this value at the stable phase ϕ_{s}:

$$\dot{\phi}(\phi_{\mathrm{s}}) = \sqrt{2\zeta\left[W(\phi_{\mathrm{U}}) - W(\phi_{\mathrm{s}})\right]}\ . \tag{2.18}$$

The bucket area is the area enclosed by the separatrix and is calculated by the following integral:

$$A_{\mathrm{B}} = 2\int_{\phi_{\min}}^{\phi_{\max}} \sqrt{2\zeta\left[W(\phi_{\mathrm{U}}) - W(\phi)\right]}d\phi\ , \tag{2.19}$$

where $\phi_{\min}$ and $\phi_{\max}$ are defined by $W(\phi_{\mathrm{U}}) - W(\phi) = 0$.

For sinusoidal RF voltages, the Hamiltonian becomes:

$$H(\phi, \dot{\phi}) = \frac{1}{2}\dot{\phi}^2 + \omega_{\mathrm{s}}^2 W_{\mathrm{s}}(\phi)\ . \tag{2.20}$$

This formalism is useful, because the Hamiltonian contains the synchrotron frequency corresponding to the stable phase in the bucket, but $W_{\mathrm{s}}(\phi)$ is required

to have a scaling factor $1/\cos\phi_0$ compared to $W(\phi)$:

$$W_{\mathrm{s}}(\phi) = \frac{1}{\cos\phi_0} W(\phi) \ . \tag{2.21}$$

2.2.2 Synchrotron frequency spread

The function describing the revolution frequencies for particles in phase space as a function of one of the variables is called the synchrotron frequency distribution or synchrotron frequency spread. In the Hamiltonian formalism this can be calculated based on a method first introduced in astronomy [127, pp. 243–57]. The technique involves a transformation of the Hamiltonian to action-angle variables. This transformation reveals the periodicity of the trajectories in phase space [127, pp. 249–50]. The action, J, is introduced as one of the variables of the transformed Hamiltonian H'.

Following the general procedure of [127, p. 247], J becomes

$$J = \oint p dq \ \rightarrow J = \oint \dot{\phi}(\phi) d\phi \ . \tag{2.22}$$

The value of the line integral is equal to the area enclosed by the trajectory over a period of oscillation in phase space [127, p. 247]. The frequency, f_{s}, or angular frequency, ω_{s}, of the oscillation belonging to one trajectory is directly given [127, p. 251] by

$$f_{\mathrm{s}} = \frac{\partial H'}{\partial J} \text{ or } J' = \frac{1}{2\pi} J \rightarrow \omega_{\mathrm{s}} = \frac{\partial H'}{\partial J'} \ . \tag{2.23}$$

The value of the Hamiltonian during the transformation is constant $H' = H$, since it is assumed that this value is not explicitly dependent on time. Therefore by calculating the values of $H' = H$ and J and forming the derivative, the synchrotron frequencies for each trajectory can be calculated. The result of such calculation is Fig. 2.3, calculated for a conventional, stationary bucket.

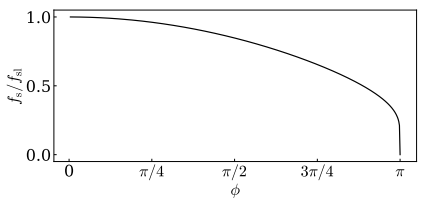

Figure 2.3: Synchrotron frequency spread in a conventional, stationary bucket as a function of phase.

A different reasoning can be found in [124, pp. 247–8], which calculates the revolution period, T, and derives a specific J for conventional buckets using $g(\phi) = \sin\phi$. Similar calculations in different variables are found for example

in [128, pp. 115–6] or [124, pp. 256–8] with analytical estimations for the case of the conventional, stationary bucket.

An equivalent method of finding the synchrotron frequency spread is to Fourier transform the time evolution of one of the variables, which can be performed based on the discrete, tracking method as mentioned in Section 2.4.

2.3 Barrier buckets

A gap in the otherwise constant longitudinal line density can be made by two isolated pulses as illustrated by Fig. 2.4 (top). This generates two distinct regions based on the value of $g(\phi)$. When $g(\phi) \neq 0$, the trajectory of the particles changes direction. If their phase velocity is sufficiently low, they reflect off the potential barriers, hence this is called the reflection region, with its length in phase being ϕ_r. If their phase velocity is too high, they are not trapped by the potential barriers as shown by the outer trajectories of Fig. 2.4 (bottom), which in our application would cause beam loss. When $g(\phi) = 0$, the particles drift along straight trajectories in phase space called the drift space. ϕ_d is the length of the drift space in phase.

Comparing the fundamental behaviour of the beam in stationary barrier buckets with conventional stationary buckets can be done by comparing their synchrotron frequency distributions as calculated from the action J according to Eq. 2.23. Figure 2.5 shows the synchrotron frequency spread in barrier buckets having different $\phi_\mathrm{d}/\phi_\mathrm{r}$ aspect ratios, but the same bucket height versus the phase velocity. The synchrotron frequency spread was normalised to the one of the conventional bucket, denoted f_sl and calculated from Eq. 2.12. The maximum of the synchrotron frequency becomes significantly lower compared to a conventional bucket as the drift space increases for the same bucket height. The consequences of this with respect to the barrier bucket manipulations will be explored in Section 2.3.2 and Chapter 4.

2.3.1 Bucket height and area for sine based barrier buckets

An isolated sine pulse as illustrated by Fig. 2.6 is a good approximation of the realistic pulses shown in Fig 2.4 (top) with the advantage, that it allows for the analytical calculation of the bucket parameters. These are given in the variables energy and voltage, such that they can be used to estimate the requirements of the barrier bucket RF system in Chapter 3.

The normalised RF voltage is defined as the following using the notations of

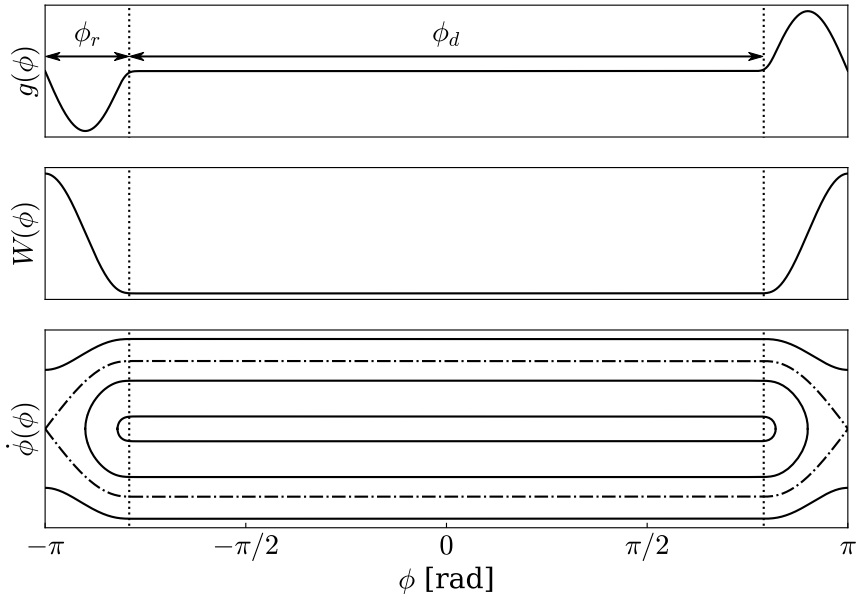

Figure 2.4: Normalised RF voltage (top) of the pulsed RF system generating a barrier bucket, together with an illustration of corresponding trajectories (bottom) in the longitudinal phase space, including the separatrix (dashed). Barrier bucket parameters in barrier RF phase. ϕ_d corresponds to the drift space, where the particles do not experience any RF voltage. ϕ_r corresponds to the reflection region on one side of the barrier.

Fig. 2.6:

$$g(\phi) = \begin{cases} \mathrm{sgn}(\eta)\sin\left(\phi\frac{2\pi}{\phi_\mathrm{r}}\right), & \text{if} \quad -\phi_\mathrm{r}/2 \leq \phi < \phi_\mathrm{r}/2 \\ 0, & \text{otherwise.} \end{cases} \tag{2.24}$$

This is scaled with the peak voltage, V.

It is convenient to define the harmonic number corresponding to the reflection region generating the gap, because the form of the bucket height and area expressions become similar to ones of the conventional buckets:

$$h_\mathrm{r} = \frac{\pi}{\phi_\mathrm{r}} \ . \tag{2.25}$$

Note that this is not the same as the conventional harmonic number, h, of the wide-band RF system. The latter is fixed at $h = 1$ for the barrier bucket waveforms used in these studies, meaning that the wide-band waveform is defined for one revolution of the accelerator.

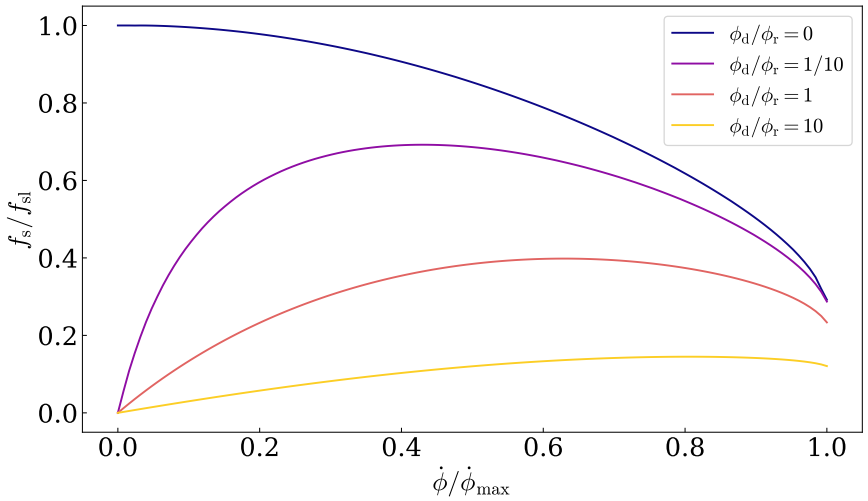

Figure 2.5: Synchrotron frequency spread as the function of the relative phase velocity in barrier buckets made by the same sinusoidal pulses with different drift space ratios. $\phi_d/\phi_r = 0$ corresponds to a conventional bucket, see also Fig. 2.3.

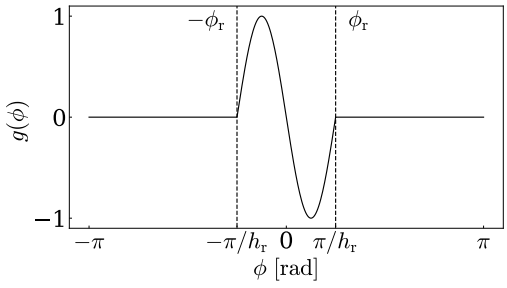

Figure 2.6: Illustration of the normalised amplitude $g(\phi)$ and the gap harmonic h_r parameters for a barrier bucket waveform. The $[-\pi, \pi)$ interval represents the whole circumference of the accelerator.

The frequency associated with isolated sine is defined as:

$$f_r = h_r f_{rev} \ . \tag{2.26}$$

The drift region, where the RF amplitude is zero covers the remaining part of the circumference:

$$t_d = \frac{1}{f_{rev}} \left(1 - \frac{1}{h_r}\right) \quad \text{and} \quad t_g = \frac{1}{f_{rev} h_r} \ . \tag{2.27}$$

This also means that $1/f_{rev} = T_{rev} = t_r + t_d$.

Following the definitions above, the bucket half height of the barrier bucket can be expressed as the bucket height of the conventional sinusoidal bucket

obtained from Eq. 2.18:

$$\Delta E_{\max} = \beta \sqrt{\frac{2eVE}{\pi h_{\mathrm{r}} |\eta|}} \ . \tag{2.28}$$

The barrier bucket area consists of the area of the reflection region and the drift region. According to Eq. 2.19, the total area of the reflection region is the area of a single, conventional, stationary bucket:

$$A_{\mathrm{g}} = \frac{16\beta}{(2\pi)^{2/3} f_{\mathrm{r}}} \sqrt{\frac{eVE}{h_{\mathrm{r}} |\eta|}} \ . \tag{2.29}$$

The area of the drift space is the bucket height times the duration of the drift space in time:

$$A_{\mathrm{d}} = 2\beta \sqrt{\frac{2eVE}{\pi h_{\mathrm{r}} |\eta|}} \ t_{\mathrm{d}} \ . \tag{2.30}$$

The barrier bucket area is the sum of the reflection regions and the drift space and it is obtained by adding Eqs. 2.29 and 2.30:

$$A_{\mathrm{B}} = A_{\mathrm{g}} + A_{\mathrm{d}} \ . \tag{2.31}$$

It is also useful to express the peak RF voltage needed for a given bucket area. Expressing V from Eqs. 2.29, 2.30 and 2.31 results in

$$V = \frac{A_{\mathrm{B}}^2}{4e} \ \frac{|\eta| f_{\mathrm{rev}}^2}{\beta^2 E} \ \frac{h_{\mathrm{r}}^3}{\left[\frac{8}{(2\pi)^{2/3}} + \sqrt{\frac{2}{\pi}} \left(h_{\mathrm{r}} - 1 \right) \right]^2} \ , \tag{2.32}$$

where the first group of terms on the right-hand-side are constants, the second group are dependent on the energy of the beam and the third only on the width of the gap.

2.3.2 Estimation of phase-space area growth due to barrier bucket compression and expansion

To estimate the emittance growth during the barrier bucket compression and expansion, the trajectory of a particle encircling the entire bunch is studied. The surface inside this trajectory represents the initial value of its invariant. The following derivation has two parts corresponding to the two regions of the stationary barrier bucket. The first part describes the changes in the drift space by looking at the nature of reflection of particles off a moving potential barrier. The second part describes the changes in the reflection region. Together these provide a basis for the estimates of the emittance growth and barrier speed limits.

The drift speed of the particle outside of the reflection region in phase space is the phase velocity $\dot{\phi}$. The phase velocity of the barrier is denoted as $\dot{\phi}_\mathrm{b}$, which also moves along the ϕ axis. The barrier speed is taken to be constant, as it was the case in the tests reported in further parts of this section.

Looking at the dynamics of a single reflection, it is evident that the phase velocities before and after a reflection are equal and have the opposite sign for the case of a stationary barrier. This motion is mathematically identical to an elastic collision of a point particle with a stationary wall of infinite mass in a non-relativistic approximation. However, when the wall is moving with a constant, non-zero velocity v_wall in the observer's reference frame, the velocities before, v_i, and after, v_f, according to the classical Galileo transformation are the following:

$$v_\mathrm{i} + v_\mathrm{f} = 2\, v_\mathrm{wall}\,. \tag{2.33}$$

These speeds do not depend on the details of the reflection, they only assume that the interaction happens and energy and momentum are conserved. This is also the assumption that is made for the phase velocity of a particle in phase space, where the wall becomes the moving barrier:

$$\dot{\phi}_\mathrm{i} + \dot{\phi}_\mathrm{f} = 2\, \dot{\phi}_\mathrm{b}\,. \tag{2.34}$$

This relationship holds for an arbitrary voltage shape, as long as its amplitude guarantees that the particle is reflected.

During the reflection, the drift space gets shorter in case of compression or gets longer in case of expansion. The time it takes for a particle to be reflected can be approximated by half of a synchrotron period $T_\mathrm{sl}/2 = \pi/\omega_\mathrm{s}$ of a conventional, stationary RF bucket corresponding to the reflection region of the barrier bucket. The phase of the barrier moves half of the synchrotron period by $\dot{\phi}_\mathrm{b} T_\mathrm{sl}/2 = \dot{\phi}_\mathrm{b}\pi/\omega_\mathrm{s}$.

To estimate the change of emittance in the reflection region, a linear voltage is assumed for a stationary bucket. This is justified, since the essential particle dynamics in a barrier bucket does not depend on the shape of the voltage used, but only on the integral of the voltage [36]. Therefore the Hamiltonian for the moving half bucket representing the reflection region becomes

$$H(\phi, \dot{\phi}) = \frac{1}{2}\dot{\phi}^2 + \frac{1}{2}\omega_\mathrm{s}^2\phi^2\,. \tag{2.35}$$

The following geometrical argument can be used to estimate the emittance growth during the time the particle reflects off the barrier while the barrier is moving at the same time. Let us assume an initial half drift space length, see also Fig. 2.4, of $\phi_\mathrm{d}/2$ compared to the edge of the reflection region. Then

using E.q. 2.34 and the notations of Fig. 2.7, the ratio of the two coloured areas

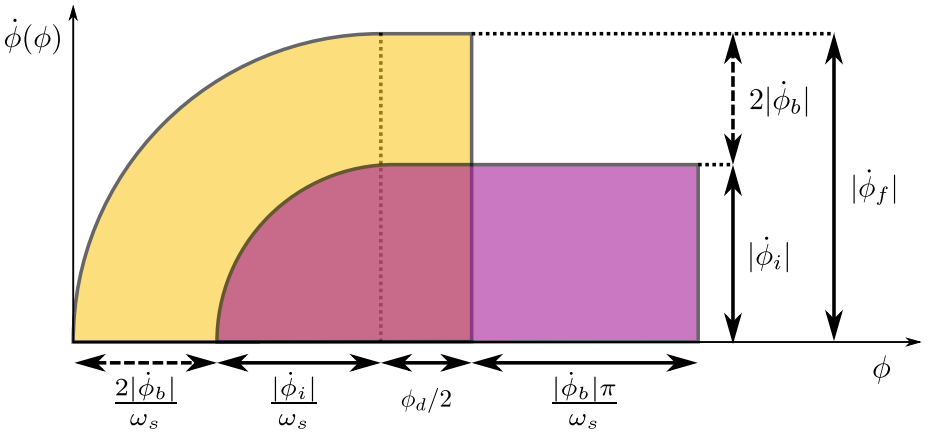

Figure 2.7: Diagram of the quarter areas of the phase space before and after a particle reflection off a moving barrier. The two phase spaces are shifted such that the main parameters used in the calculation are visible.

representing the change in emittance is evaluated:

$$\frac{A_\mathrm{f}}{A_\mathrm{i}} = \frac{|\dot{\phi}_\mathrm{f}|\left(|\dot{\phi}_\mathrm{f}|\pi + 2\phi_\mathrm{d}\omega_\mathrm{s}\right)}{|\dot{\phi}_\mathrm{i}|\left(|\dot{\phi}_\mathrm{i}|\pi + 4|\dot{\phi}_\mathrm{b}|\pi + 2\phi_\mathrm{d}\omega_\mathrm{s}\right)} \ . \tag{2.36}$$

It is worth noting that the phase change due to the change of a trajectory $2|\dot{\phi}_\mathrm{b}|/\omega_\mathrm{s}$ in the reflection region is not the same as the change of phase in the drift region due to the displacement of the barrier $|\dot{\phi}_\mathrm{b}|\pi/\omega_\mathrm{s}$. The singularity when $\dot{\phi}_f = 2\dot{\phi}_\mathrm{b}$ is the case when the beam in a very thin barrier bucket turns into a beam in a conventional RF bucket in $T_\mathrm{s}/2$ time or vice versa. This provides a hard limit on the barrier speed for an adiabatic manipulation, see Fig. 2.8 (right). If the area occupied by the particles in phase space changes too fast, the manipulation will become non-adiabatic, therefore the barrier speed should correspond to a very small area change during one reflection, see Fig. 2.8 (left). Using the notations of Fig. 2.4, $\phi_\mathrm{r} = \dot{\phi}_\mathrm{f}/\omega_\mathrm{s}$. The estimated emittance growth corresponding to different $\phi_\mathrm{d}/\phi_\mathrm{r}$ barrier bucket drift space ratios can also be seen on Fig. 2.8 (left).

The speed of the barrier should be much smaller than the drift speed of a particle with a maximum energy offset [36, 45], which means $\dot{\phi}_\mathrm{b}/\dot{\phi}_\mathrm{f} \ll 1$. This is the limiting case of a particle, which is not interacting with the potential barrier at all, as it never enters the reflection region. However, the speed of the barrier must be much less than even the half of this [37], which the present estimation also shows.

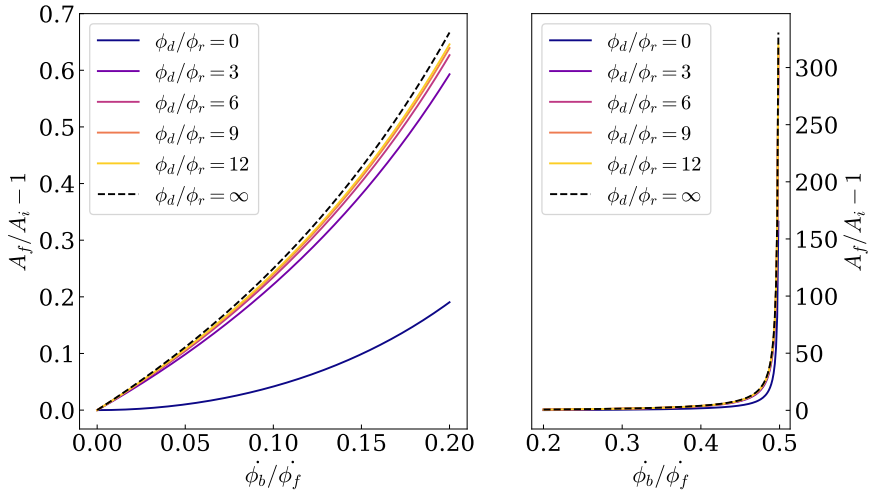

Figure 2.8: Left: Emittance growth estimate for low relative barrier speeds. Right: limiting case of the relative barrier speed at half of the phase velocity of an outer particle in the bunch.

2.4 Discrete time approach

The longitudinal dynamics of the particles in a synchrotron can be described on a turn by turn basis using a set of two non-linear difference equations, sometimes called mappings [124, p. 235]. Longitudinal particle tracking is a method of solving the difference equations of the synchrotron motion numerically. This method is different from the analytical calculations in phase space, since it does not involve an averaging step. Three sets of variables were used in thesis based on the same turn-by-turn tracking principle. Table 2.1 shows the variables used by the different methods. Certain choice of variables makes a problem easier

	Variables
Normalised tracking	ϕ, $\dot{\phi}$
Time- and energy offset based	$\Delta t, \Delta E$
Phase and relative momentum offset based	ϕ, $\delta = \Delta p/p$

Table 2.1: Types of tracking used in the thesis

to handle, the reason for choosing each method is highlighted in this section. A convention applied to all cases is that the indices n and $n+1$ are referring to the n and $n+1$ iteration of the difference equation performed from some set of initial conditions.

2.4.1 Normalised tracking

First, normalised longitudinal tracking is outlined. Using the same notations as in section 2.2.1, the mapping equations to calculate the ϕ and $\dot{\phi}$ coordinates of a particle are the following

$$\phi_{\mathrm{n+1}} = \phi_{\mathrm{n}} + \frac{2\pi}{\omega_0}\dot{\phi}_{\mathrm{n}} \ , \tag{2.37}$$

$$\dot{\phi}_{\mathrm{n+1}} = \dot{\phi}_{\mathrm{n}} - \frac{2\pi}{\omega_0}\omega_{\mathrm{s}} g(\phi_{\mathrm{n+1}}) \ . \tag{2.38}$$

Equation 2.38 assumes that the particle drifts with the phase velocity of the previous turn, $\dot{\phi}_n$, over a turn of the duration $2\pi/\omega_0$. Following from Eqs. 2.7, 2.9 and 2.12, the second term on the right-hand-side of Eq. 2.38 represents the phase velocity change integrated over one turn in the stationary bucket case. This formulation is useful, since the slowly-varying accelerator parameters are all lumped in one term, ω_{s}, therefore the comparison of the two phase space variables is transparent, which makes validating analytical considerations mentioned in section 2.3.2 easier.

2.4.2 Energy- and time-offset based tracking

The energy and time offset based tracking is an efficient way of tracking physical variables, which is implemented in the CERN Beam Longitudinal Dynamics code BLonD [129]. Since the change of the variables compared to their magnitude is small, it is more memory efficient and also more precise to track the differences only [130, p. 19]. The units and the derivations of these equations can be found at the following reference [129]. Since the energy unit is eV, the voltage V has the same unit as the energy. The tracking equations used in this thesis are the following:

$$\Delta E^{n+1} = \Delta E^{n} + \sum_{k=0}^{n_{\mathrm{rf}}-1} V_k^n \sin\varphi_{\mathrm{rf},k}(\Delta t^n) - (E_0^{n+1} - E_0^n) \ , \tag{2.39}$$

$$\Delta t^{n+1} = \Delta t^{n} + \frac{2\pi}{\omega^{n+1}} - \frac{2\pi}{\omega_0^{n+1}} \ . \tag{2.40}$$

The constant n_{rf} is the number of RF systems, V_k and $\phi_{\mathrm{rf},k}$ is the peak voltage and phase of these, respectively.

Note that the sum of the voltages in equation 2.40 resembles a classical Fourier sum of an odd waveform. This simple notion was utilised to model the wide-band waveform used in beam tests in BLonD as shown in the results in Chapter 4. This was accompanied with the appropriate amplitude modulation of the harmonics, as it will be seen in Chapter 3 to use identical methods of the

hardware implementation also developed during this study.

2.4.3 Phase and relative momentum offset based tracking

To cross-check the BLonD simulations for the re-phasing operation in conventional buckets for the proposed synchronisation in Chapter 5, a third set of equations [124, p. 235] were used in a custom made tracker.

$$\delta = \frac{\Delta p}{p} \tag{2.41}$$

$$\delta_{n+1} = \delta_n + \frac{qV}{\beta^2 E}(\sin\phi_n - \sin\phi_0) \ , \tag{2.42}$$

$$\phi_{n+1} = \phi_n + 2\pi h \eta(\delta_{n+1})\delta_{n+1} \ . \tag{2.43}$$

These equations are the direct consequence of Eqs. 2.7, 2.9 for the case of $g(\phi) = \sin\phi$.

2.5 Beam-accelerator interaction, impedance

The goal of this brief section is the introduce the beam and accelerator interaction restricted to longitudinal impedance.

The beam generates a potential by passing through a structure in the accelerator. This is called the wake function $W_{\mathrm{L}}(t)$ and it essentially acts as an extra wide-band RF system on the beam. In the frequency domain, this pulse corresponds to an impedance, called the longitudinal impedance. [124, p. 355]

$$Z(\omega) = \int_{-\infty}^{\infty} W_{\mathrm{L}}(t) e^{-j\omega t} dt \ , \ W_{\mathrm{L}} = \frac{1}{2\pi}\int_{-\infty}^{\infty} Z(\omega) e^{j\omega t} d\omega \ . \tag{2.44}$$

The complex valued and frequency dependent longitudinal impedance depends on many parameters. The following types are distinguished: the longitudinal space charge impedance, resistive wall impedance and narrow- and broad-band impedances [131].

The longitudinal space charge impedance depends on the vacuum impedance, Z_0 the geometrical factor of the beam pipe, g_0, and the speed of the particles, β, γ [124, pp. 365–6] and [132, 133]:

$$\frac{Z_{\mathrm{SC}}}{n} = -j\frac{g_0 Z_0}{2\beta\gamma^2} \ . \tag{2.45}$$

The resistive wall impedance follows from the fact that the beam pipe is not perfectly conducting [124, pp. 357–8]. Therefore predominantly the high frequency components of the wake can penetrate the beam pipe causing losses.

This depends on the skin depth $\delta_{\text{skin}} = \sqrt{2/\sigma_{\text{c}}\mu\omega}$, where σ_{c} and μ are the conductivity and the permeability of the beam pipe and ω is the frequency component in question. The impedance contribution can be approximated as:

$$Z(\omega) \approx \frac{R}{b\sigma_{\text{c}}\delta_{\text{skin}}(\omega)} \ . \tag{2.46}$$

Where b is the average radius of the beam pipe. Further geometries can be found at [134].

In general, the narrow-band impedances in an accelerator are present due to the resonant RF cavities. Broad-band impedances are due to broad-band cavities and in general discontinuities of the beam pipe.

2.6 Summary

This chapter describes the two main tools to investigate longitudinal beam dynamics in a synchrotron, the continuous time, analytical approach based on Hamiltonian mechanics and the discrete time approach as it is used in this thesis work. The continuous time approach was applied to describe the properties of barrier buckets and to calculate the phase space area change in barrier buckets in a simple way. Finally, concepts related to longitudinal impedance were introduced briefly.

Chapter 3

Requirements and implementation of the barrier bucket waveform generator

3.1 Introduction

To generate a barrier bucket waveform, a wide-band RF system is needed. This can be introduced with a short comparison with a single harmonic RF system in the context of synchrotrons. A single RF system, as its name suggests, can produce a sine wave of a given frequency [124, pp. 330–347] [135]. This single frequency can be changed to a smaller or larger degree by tuning the system accommodating the need of the acceleration of beams. A wide band or pulsed RF system [106, pp. 263–283], on the other hand, is capable of generating more harmonics across the spectrum at the same time. Hence a typical multi-harmonic RF system can interact with several parts of the beam spectrum at once making beam manipulations that require wide-band waveforms possible. However, a wide band system couples to more harmonic components of the spectrum, too, making the control of such systems more complex if their impedance or the beam intensities are higher.

In the case of the PS, as introduced in Chapter 1, the Finemet® system can not provide enough power to change the mean energy of the beam in a short time, therefore acceleration is not achievable in a realistic time frame with it. On the other hand, it is ideal for barrier bucket generation.

In order to interact with the beam, the barrier bucket waveform has to be synchronous with it as explained in the previous chapter. To achieve this, a beam synchronous, arbitrary waveform generator was devised and implemented in programmable logic. It uses the direct digital synthesis (DDS) principle [136, 137] extended to arbitrary waveforms as opposed to the conventional sine-based DDS. To implement the generation of the drive signal for the power RF system before the end of 2018, as many parts of the existing low power level RF infrastructure of the CERN PS was reused as possible. The details of this implementation are found in Section 3.3.

The electronic board with the new barrier bucket firmware on a field programmable gate array (FPGA) working in the lab was an important milestone for the PhD, but the integration into the accelerator high power level RF and control system was just as crucial. In particular, the distortion that the high power signal chain adds to the wide-band waveform had to be compensated for to achieve the desired waveform shape at the cavity gap. Section 3.4 describes the measurements and the model used to achieve this.

In order to investigate the behaviour of the beam in barrier buckets, longitudinal beam dynamics simulations are an indispensable tool as described in Chapter 2. The barrier bucket waveform generator system was added to the already existing simulator framework: BLonD to provide an accurate representation of the real RF system for numerical studies as described by Section 3.5.

3.2 Requirements

The pulse generating the gap must have two main properties. Firstly, the duration should be in the range of the rise time of the kickers, which is in the order of 300 ns [138]. Secondly, the amplitude should be high enough efficiently remove particles from the gap region during this time. In addition, the beam synchronous requirement mentioned in the introduction means that the frequency range of the system has to be compatible with the revolution frequency range of the PS. This, together with the wide band waveform defines the frequency range and the bandwidth of the installation. Furthermore, the system needs to be compatible with the CERN control system for remote control. These requirements are detailed below.

3.2.1 Amplitude requirement

Measurements with beam along the cycle detailed in Section 4.4 were used to establish total longitudinal emittance of the beam of 16 bunches. At least the total longitudinal emittance of 24 eVs of these bunches will have to be contained

by the barrier buckets, which provides a lower estimate for the amplitude. The maximum voltage available from the Finemet® cavity is about 5 kV [31]. The achievable bucket filling factors were compared to this value across a range of gap sizes using Eq. 2.32. The filling factor is the ratio of the longitudinal emittance of the beam divided by the bucket area.

Figure 3.1 shows the voltage requirement calculated for different filling fac-

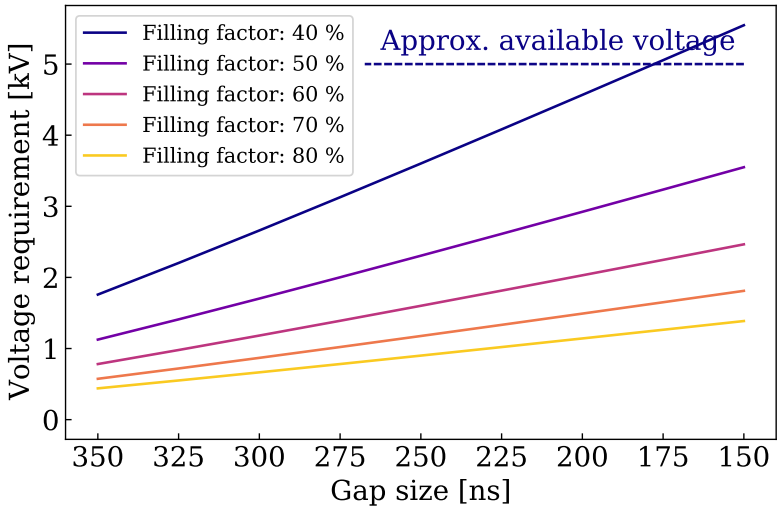

Figure 3.1: Peak voltage requirement for the ideal case of emittance preservation during re-bucketing.

tors based on Eq. 2.32 as a function of the gap size for the total emittance of the 16 bunches. The gap size is taken to be the length of the non-zero part of the waveform, which approximates the completely particle free region with low filling factors well in the first order. However, even if there are some particles in the gap region with higher filling factors, the line density can still be significantly reduced by the potential barriers as illustrated in Fig. 2.4 (bottom).

The re-bucketing without longitudinal blow up can not be expected in the present configuration, because of the limited time available. Longitudinal tracking simulations using BLonD were performed to estimate the longitudinal emittance of the coasting beam at extraction. This was found to be 30 eVs. Hence the voltage requirements are somewhat higher assuming a blow up during debunching. The study of the de-bunching process in detail is foreseen as future work detailed in Chapter 6.

Fig 3.2 shows that with the present RF system, a filling factor of approximately 80% can be achieved with the peak voltage of 5 kV for all gap sizes. It is clear that the voltage requirement increases with narrower gaps for the same

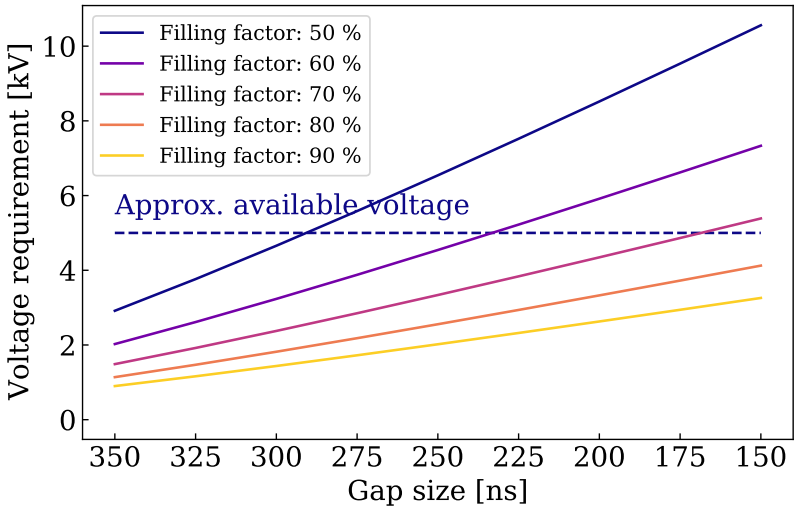

Figure 3.2: Peak voltage requirement taking the simulated longitudinal emittance blow-up during re-bucketing into account, too.

filling factor. Nevertheless, the amplitude of the Finemet® system based on these estimations is sufficient to make a particle free region in the beam, which can reduce the losses at extraction.

3.2.2 Frequency range and waveform control

This system should be able to validate the behaviour of the beam in an RF barrier bucket in the PS. This means that it should be able to operate in the revolution frequency range, 437 kHz – 476 kHz, synchronously with the beam. Furthermore, it should be compatible with the existing RF installations.

In order to generate azimuthally moving barriers, the phase of the barrier pulses have to be controlled remotely from the CERN Control System [139, 140]. To facilitate the re-bucketing process from the $h = 16$ bunches to the barrier bucket, the amplitude of the barrier bucket system is required to be controlled in real-time, too.

As it was explained in Section 2.3 if one inverts an RF waveform generating a barrier bucket, a conventional, isolated bucket is generated. Therefore a waveform inverter is useful to test the behaviour of the beam in a conventional bucket and a barrier bucket generated at the same azimuthal position. This function is useful to change between below and above transition operation, too. In addition, the ability to program a constant RF offset makes the system more

flexible in calibrating azimuthal reference points.

3.2.3 Bandwidth requirement

The barrier bucket waveform consists of a zero and non-zero part, which means that it is a wide-band waveform as described in 2.3. However, the shape of the waveform is a free parameter, provided it satisfies the general requirements. Hence the trade-offs involved in choosing a waveform shape are investigated in this section.

Firstly, the bandwidth requirement for two commonly used waveforms for barrier buckets, the sine and the square based barriers is evaluated analytically. Then a cosine section waveform is analysed that can be advantageous in certain respects compared to the other two. Finally, regardless of the waveform of choice, a windowing technique is presented that limits the bandwidth requirement for all pulses while keeping the correctness of their phase, which is important in synchrotron applications.

3.2.3.1 Waveform shape, bucket height and roll-off

Since the pulses have a fixed period determined by the revolution frequency of the synchrotron, it is sufficient to calculate components of the Fourier series:

$$g(\phi) = \sum_{n=0}^{\infty} a_n \cos n\phi + \sum_{n=1}^{\infty} b_n \sin n\phi \ , \tag{3.1}$$

where a_n and b_n are the Fourier coefficients. Waveforms that generate barrier buckets to be used in the present studies are odd as detailed in Section 2.3, hence $a_n = 0$. Eq. 3.1 simplifies to:

$$g(\phi) = \sum_{n=1}^{\infty} b_n \sin n\phi \ . \tag{3.2}$$

The bandwidth requirement depends on the shape of the waveform. Three example waveforms are analysed in this section based on their discontinuities. Square and sine barriers are introduced first, which have been widely used in generating barrier buckets [35, 45, 106, 110, 141]. An additional waveform based on cosine sections is introduced which combines desirable spectral properties of both, the square and sine waveforms.

The square wave is a discontinuous waveform, therefore its bandwidth requirements are the most demanding. This can be analytically seen from the diminishing of its Fourier coefficients. The normalised amplitude function, $g(\phi)$, as introduced in Section 2.2.1 is defined for the square wave barrier first:

$$g(\phi) = \begin{cases} -\mathrm{sgn}(\eta), & \text{if } -\pi/h_\mathrm{r} \leq \phi \leq 0 \\ \mathrm{sgn}(\eta), & \text{if } 0 < \phi \leq \pi/h_\mathrm{r} \\ 0, & \text{otherwise .} \end{cases} \tag{3.3}$$

The waveform changes sign at transition energy, this is incorporated in the $\mathrm{sgn}(\eta)$ term.

Its Fourier coefficients evaluate to:

$$b_n = \mathrm{sgn}(\eta)\frac{2}{n\pi}\left[1 - \cos\left(\frac{n}{h_\mathrm{r}}\pi\right)\right] , \tag{3.4}$$

decreasing proportional to $1/n$. Technically, this barrier is easier to realise when one uses, for instance, the switched signals of a power converter as demonstrated in [106]. However, due to its discontinuity, it is not the best candidate to be implemented using a wide-band RF system. On the other hand, the advantage of using a square barrier is that it achieves the largest bucket area for a given reflection region width as shown by Table 3.1.

As a generalisation of the square wave, an arbitrary pulse train synthesis method is presented in Appendix A. That approach uses two phase shifted harmonics of an equal frequency at half of the harmonic frequencies of the classical Fourier sum to generate a pulse train. This could potentially be beneficial in implementations with wide band feedback as it is referred to in Section 3.4.

The normalised amplitude of the single sine barrier waveform is defined as follows.

$$g(\phi) = \begin{cases} \mathrm{sgn}(\eta)\sin\left(h_\mathrm{r}\phi\right), & \text{if } -\pi/h_\mathrm{r} \leq \phi \leq \pi/h_\mathrm{r} \\ 0, & \text{otherwise .} \end{cases} \tag{3.5}$$

The first derivative of this waveform is discontinuous. Its Fourier coefficients were published in [35]. The calculation leads to two different formulas, since there is a discontinuity depending on the value of n and h_r. When $n \neq h_\mathrm{r}$:

$$b_n = \mathrm{sgn}(\eta)\frac{2h_\mathrm{r}}{\pi\left(h_\mathrm{r}^2 - n^2\right)}\sin\left(\frac{n}{h_\mathrm{r}}\pi\right) . \tag{3.6}$$

When $n = h_\mathrm{r}$,

$$b_n = \frac{\mathrm{sgn}(\eta)}{h_\mathrm{r}} . \tag{3.7}$$

The coefficients decrease with $1/n^2$, meaning that the isolated sine wave is less demanding in terms of the required bandwidth compared to the square wave, since its Fourier coefficients diminish faster with the number of terms required to synthesise the waveform as depicted in Fig. 3.4. However, the bucket height shrinks for the same h_r compared to the square wave representing the maximum

Waveform	Relative bucket height	Relative bucket area
Square	1	1
Sine	$\sqrt{2/\pi} \approx 80\%$	$\frac{3\sqrt{2}(\pi(h_\mathrm{r}-1)+2)}{\pi^{\frac{3}{2}}(3h_\mathrm{r}-1)}$
Cosine sections	$\sqrt{2}/2 \approx 71\%$	$\approx 2.1213\frac{2\sqrt{2}\sqrt{h_\mathrm{r}}+\pi^{\frac{3}{2}}(h_\mathrm{r}-1)}{\pi^{\frac{3}{2}}(3h_\mathrm{r}-1)}$

Table 3.1: The comparison of the bucket heights and bucket areas for different barrier bucket generating waveform shapes for the same h_r. Calculating the cosine sections bucket area involves a numerical integration.

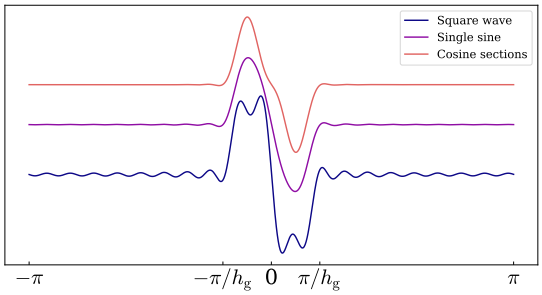

Figure 3.3: Comparison of different waveforms generated for the same gap width using 20 Fourier harmonics.

for a given h_r as seen in Table 3.1.

The following example is made out of cosine sections. The waveform has a discontinuity in its second derivative but not in the zeroth or in the first:

$$g(\phi) = \begin{cases} \mathrm{sgn}(\eta)\left[\frac{1}{2}\cos\left(2h_\mathrm{r}\phi\right) - \frac{1}{2}\right], & \text{if } -\frac{\pi}{h_\mathrm{r}} \leq \phi \leq 0 \\ -\mathrm{sgn}(\eta)\left[\frac{1}{2}\cos\left(2h_\mathrm{r}\phi\right) - \frac{1}{2}\right], & \text{if } 0 < \phi \leq \frac{\pi}{h_\mathrm{r}} \\ 0, & \text{otherwise .} \end{cases} \tag{3.8}$$

The waveform is illustrated in Fig. 3.3. Its Fourier coefficients when $2h_\mathrm{r} \neq n$ are

$$b_n = \mathrm{sgn}(\eta)\frac{4h_\mathrm{r}^2}{\pi n\left(4h_\mathrm{r}^2 - n^2\right)}\left[1 - \cos\left(\frac{n}{h_\mathrm{r}}\pi\right)\right] \ , \tag{3.9}$$

which decrease as $1/n^3$. When $n = 2h_\mathrm{r}$, $b_\mathrm{n} = 0$.

It can be observed from Eq. 3.9, that the $\sim 1/n^3$ roll-off begins at $n = 2h_\mathrm{r}$ contrary to the previous cases, whose coefficients start to diminish from $n = h_\mathrm{r}$. An example is shown for $h = 5$, in Fig. 3.4. Suppose that the available bandwidth for this example is set at $4h_\mathrm{r} = 20$, only to illustrate the significance of the limit being at twice of h_r. The cosine sections waveform has higher amplitudes compared with the sine in the second lobe, for the same h_r. These are harmonics 10-20 in the example of Fig. 3.4. This results in an improved waveform fidelity compared to the sine, because the higher harmonics fill the pass-band better. However, unlike the square waveform, the cosine sections pulse has a sine like

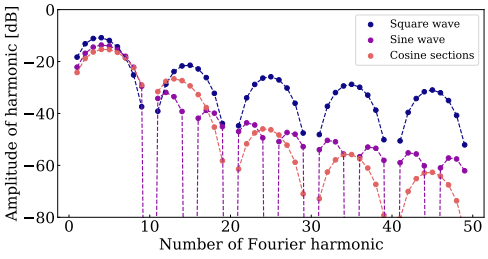

Figure 3.4: Comparison of the Fourier harmonics of different waveforms. In this example $h_r = 5$.

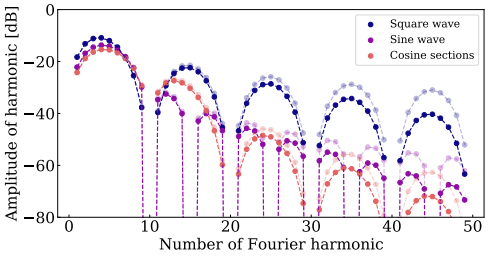

Figure 3.5: σ_3 modulated spectra. In this example $h_r = 5$. The transparent dots and lines are the Fourier coefficients without windowing ($m = 0$) corresponding to Fig. 3.4.

or even better better roll-off outside the pass-band. This behaviour is evidently not dependent on the particular parameters of the example as per Eq. 3.9 and is valid for any $h_r \geq 1$ real number. The trade-off is a lower achievable bucket height, see Table 3.1, for the exact analytical case of the cosine sections. In reality, because of the smoothing effect of the limited number of terms available, the achievable bucket heights can be higher for this waveform.

However, the sine wave still achieves more bucket height, while its wide-band characteristics are similar to the cosine one. All in all, the isolated sine wave is a good compromise between bucket height and bandwidth to be used as a shape prototype in these studies. The ringing can be lowered by using a frequency domain windowing technique to increase the convergence of the Fourier series as explained in the subsection below.

3.2.3.2 Sigma modulation or windowing

The benefit of using a smooth waveform from the beam dynamics point of view is that it reduces the formation of micro bunches in particular in the drift region as well as eases bandwidth requirement given a waveform shape. Windowing the Fourier sum at synthesis can achieve this. The trade-off is the longer tails of the waveform around the pulse. For the purposes of this exercise the shape of the actual window is not critical as long as it preserves the basic properties of the barrier bucket waveforms. The σ factors [142, p.225-229] are suited to this task, since they preserve the symmetry of the waveform. They were chosen in addition, because they are flexibly tunable via their power parameter.

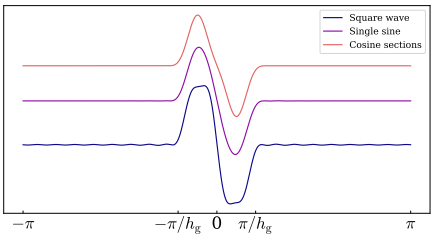

Figure 3.6: Comparison of different waveforms generated for the same gap width using 20 Fourier harmonics using σ_3 modulation.

The definition of the factors to multiply the Fourier coefficients with are

$$\sigma_m(n) = \mathrm{sinc}^m \frac{n\pi}{2(N+1)} \ , \tag{3.10}$$

where N is the total number of Fourier coefficients in the finite sum. The general shape is half of the main lobe of the sinc function. The larger m, the faster the roll-off and the narrower the main lobe. This results in larger the tail of the waveform in the time domain, but less ripple. $m = 0$ corresponds to the rectangular window.

The waveform synthesis with the sigma factors included is the following:

$$g(\phi) = \sum_{n=1}^{N} \sigma_{\mathrm{m}}(n) b_n(h) \sin n\phi \ . \tag{3.11}$$

It is clear from Eq. 3.11 that the phase of the components is not changed. The consequence in practice is that the smoothing does not affect the azimuthal position of the generated barrier bucket, which is convenient in the present implementation.

3.3 Low-level RF system

As explained in Section 3.2.3, the barrier bucket waveform has to be generated synchronously with the circulating beam. A conventional LLRF system [143] generates sinusoidal voltages, but for a barrier bucket, a special wide-band waveform is needed. In addition, the waveform has to be pre-distorted at the input of the high power amplifier chain, such that the voltage seen at the cavity gap is close to the expected, isolated, approximately sinusoidal pulses as described in earlier sections of this chapter.

3.3.1 Beam synchronous, arbitrary waveform generation

Waveform generation for a conventional digital RF system [135] in the frequency range up a few 100 MHz is typically achieved by using a direct digital synthesizer (DDS) [136, 137]. The basic structure of a DDS consists of a phase accumulator, a waveform look-up table and a digital to analogue converter (DAC). Most implementations have a sine look-up table (e.g. [144–150]) in different configurations or, alternatively use a CORDIC algorithm [151], such as [152]. Generating a barrier bucket requires a wide band waveform with many harmonics, in which case the previous solutions do not scale well. However, changing the sine only look-up table of a conventional DDS to a programmable look-up table achieves a compact arbitrary waveform generator based on the DDS principle.

Fig. 3.7 shows the block diagram of the beam synchronous, arbitrary wave-

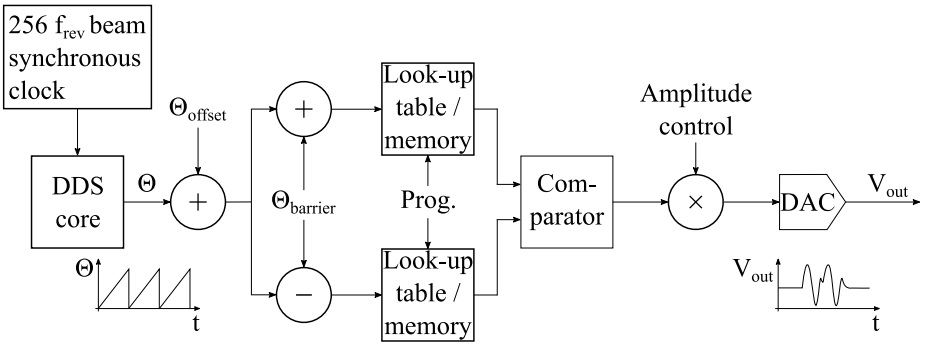

Figure 3.7: The diagram shows the functional elements of the beam synchronous RF source firmware generating barrier buckets.

form generator. The DDS core, or a special numerically controlled oscillator (NCO), provides the beam synchronous azimuth information, Θ, based on the reference clock at 256 times the revolution frequency, f_{rev} [152]. A programmable offset, Θ_{offset}, to change the centre of the generated barrier bucket was added. Two look-up tables were used to generate two symmetrically moving

barriers with respect to the fixed azimuth position, the phase shifts, Θ_{barrier}, were implemented. The waveform in the look-up tables is calculated outside the hardware allowing flexibility of choosing pre-distortion methods.

In addition, an alternate waveform generator concept was also conceived and is outlined in Appendix A. This combined with a complex multiplication based harmonic synthesis can potentially be more frugal on the same hardware platform with the added benefit of perhaps easier feedback option. However, the latter possibility was not realised, because that would have required considerably more time investment with some existing functionality re-implemented in a different form and, more importantly, the original plan with a shorter time span allowing for a longer experimental program with beam succeeded.

3.3.2 Implementation

The concept of the beam synchronous arbitrary waveform generator using programmable memory was implemented on existing electronics, the PS one turn delay feedback board [153], hosting an Altera Stratix II FPGA. This board was chosen, since its analogue and digital specifications met the requirements of barrier bucket waveform generation as outlined in Section 3.2. The advantage an FPGA is that it can be reprogrammed for a different purpose. In the present implementation, the rewiring of the device was described in virtual hardware definition language (VHDL) partially using Visual Elite and text based VHDL with the test benches simulated with Modelsim. The Altera toolchain was used for constraints definition, routing, bitstream generation and flashing.

3.3.2.1 FPGA utilisation

The challenge of the implementation was that the utilisation of the FPGA was quite high, around 70% without the barrier functionality, with the potentially re-usable firmware blocks: the NCO and the blocks necessary to connect the board to the RF signal chain and the accelerator control system including a CORDIC for validation purposes. Therefore the barrier bucket implementation had to be economical if it was to benefit from earlier development. This meant that several optimisations were performed to fit the barrier bucket firmware on the FPGA while trying not to re-develop existing functionality as detailed below.

3.3.2.2 Beam synchronous NCO

Thus, an existing numerically controlled oscillator (NCO) capable of providing beam synchronous phase information serving as a phase accumulator was the

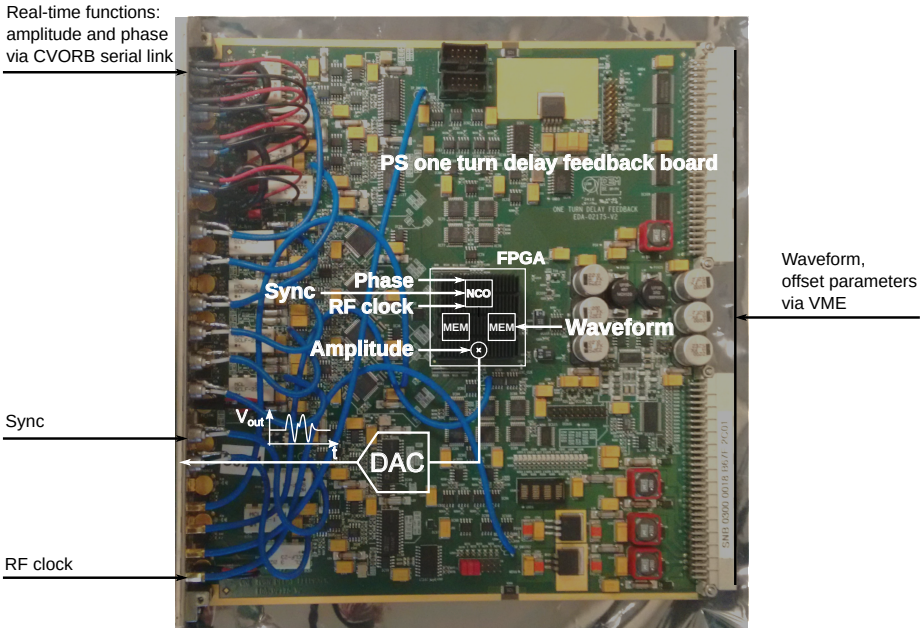

Figure 3.8: The PS one turn delay feedback board with the illustration of the barrier bucket firmware. The board inputs and outputs are also marked in our implementation. The coaxial leads are to route the test points to the front panel.

starting point of the implementation. This firmware block was analysed to see where the wide-band waveform generator could be added.

The NCO's multiplied phase output represents a fixed azimuthal or phase position, Θ_{m}. This position is a reference for the imaginary centre of the two barrier waveforms:

$$\Theta_{\mathrm{m}}(n) = \Theta + n \cdot 2^N \mod 2^M \ . \tag{3.12}$$

Here, n is the output of the phase accumulator, an N bit overflow counter driven by the RF clock outputting 2^N samples per turn. 2^M represents the available phase resolution with $M > N$ in a typical implementation. The conventional harmonic number is $h = 1$ for barrier buckets as detailed in Chapter 2, therefore not shown in the equations, and Θ is a fixed azimuthal angle. The ramp of the phase accumulator is implemented as a counter. This, together with the output of the RAM is illustrated by Fig 3.9.

In order to dynamically align the centre position of the barriers along the azimuth of the accelerator, a programmable offset, Θ_{offset}, was added to the marker, Θ_{m}:

$$\Theta_{\mathrm{out}}(n) = \Theta_m(n) + \Theta_{\mathrm{offset}} \mod 2^M \ . \tag{3.13}$$

If only one waveform is used, Θ_{offset} sets the azimuthal position of the waveform used to generate the longitudinal gap in the beam distribution.

3.3.2.3 Waveform merging and splitting

The task of this part is to generate two distinct sinusoidal waveforms and move them without overlap. This corresponds to capturing a bunch in a conventional bucket when the two waveforms are next to each other. To generate two, movable barriers to confirm the adiabaticity limits of the barrier manipulation, two RAMs with identical content were used as illustrated by Fig. 3.9.

The azimuthal angle between the two barriers was set by adding or subtracting an angle value to or from Θ_{out}, which sets the correct look-up addresses of the RAMs to offset the waveforms by the correct number of samples. Then the samples are merged and sent to the output as illustrated by by Fig. 3.12.

At the end of the waveform lookup stage of the DDS, a final amplitude scaling was added by using one multiplier only to facilitate the handover from a conventional RF system to the barrier bucket RF.

3.3.2.4 Mitigation of the latency of the address look-up

SRAM blocks were still available on the FPGA. However, the look-up during one clock cycle of the RF clock was not fast enough for a stable output using only one block of the SRAM at the highest clock speeds of 128 MHz RF clock corresponding to a speed 5% higher than the speed of light in vacuum in the ring to provide a margin for the implementation. Two of the RAM blocks were used with a clock at half speed each. Then the stable output was connected to the DAC at the original RF clock rate providing a stable output at the desired clock rate.

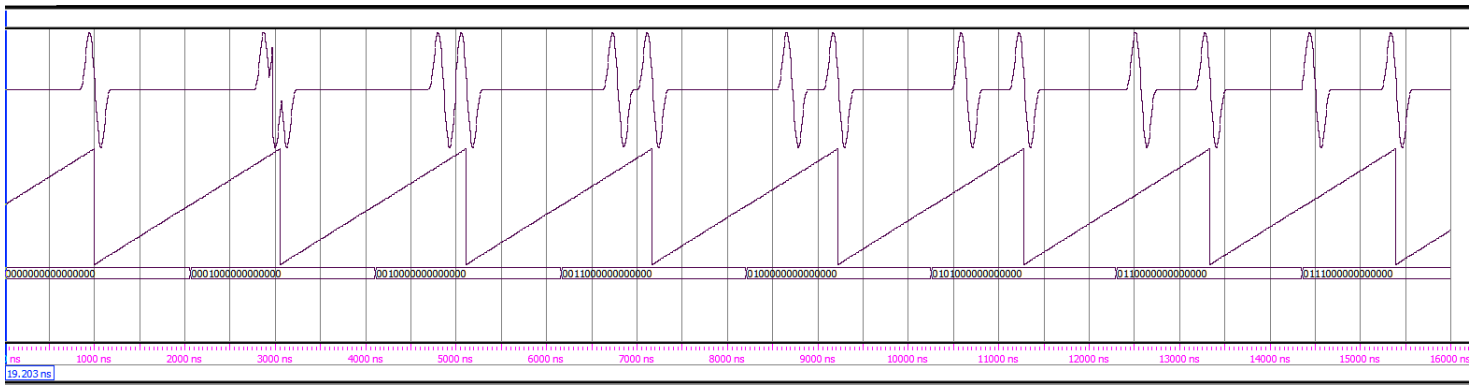

Figure 3.9: The result of a Modelsim simulation of the MHS phase ramp output (bottom) and two barriers generated per turn (top), where the distance between them can be set. Note that a distance closer than the width of the pulse can produce higher potential as the second pulse from the left shows. Such operation is not foreseen for this drive. Either one barrier is to be made per turn at extraction or multiple barriers at low energy commissioning, but not the two at the same time, hence this is not a true limitation.

3.3.2.5 Optional linear interpolator

If only a smaller amount of RAM is available with a higher resolution of phase information, interpolating the output of the RAM makes the output smoother. To do so, the lower phase bits not utilised for address look-up can be used to calculate intermediate values between two RAM output values, bb_1 and bb_2.

The linear interpolation formula is the following between two points of the waveform: bb_1 and bb_2 with l interval length at a point $bb_1 \leq \phi \leq bb_2$.

$$y(\phi) = \frac{(l-\phi)bb_1 + \phi\ bb_2}{l} \tag{3.14}$$

The calculation is done every RF clock cycle. I is the intermediate value for the interpolation and I_{out} is the digital to analogue converter (DAC) output. The interval used for the interpolation is $[0, 2^N - 1]$. The equation for a generic implementation is the following, where w is the output bitwidth, n is the number of bits used for the RAM address.

$$I[w+n-1:0] = bb_1[w-1:0]\cdot(2^n-1-\phi_{LSB}[n-1:0])+bb_2[w-1:0]\cdot\phi_{LSB}[n-1:0] \tag{3.15}$$

It can be see that $2^n - 1 - \phi_{LSB}[n-1:0]$ is the one's complement of ϕ_{LSB}, therefore it can be substituted in the equation with just a bitwise inversion and the pseudo code simplifies to the following.

$$I[w+n-1:0] = bb_1[w-1:0]\cdot(\sim \phi_{LSB}[n-1:0])+bb_2[w-1:0]\cdot\phi_{LSB}[n-1:0] \tag{3.16}$$

Then the division becomes the following:

$$I_{out} = I[w+n-1:n] \tag{3.17}$$

3.3.2.6 System integration

With a significant firmware version ready, the frequency and stability of the output was tested in the lab from 100 MHz to 128 MHz, which is beyond the required swept clock range. To integrate the drive with the cavity high power level amplifier chain, the board was installed by the accelerator ring.

For the LLRF drive to be usable with the beam, connections to the control system were established, which were at the present level of implementation so called low-level, expert settings. As illustrated by Fig. 3.8, the memory containing the waveform was exposed via a communication bus to a Python script that could write to it, running on a virtual machine on CERN's technical network. This has the advantage of changing the waveform properties, including

the pre-distortion model without changing the firmware implementation. The real-time, remote amplitude control was necessary to implement a smooth hand-over from the main RF system to the barrier RF system.

3.4 High-level RF system

A beam synchronous direct digital synthesizer drives the six pairs of solid state amplifiers. The outputs of these are directly connected to the cavity gap as illustrated by Fig. 3.10. The broad-band cavity is loaded with the magnetic alloy called Finemet® [33, 154, 155] which couples to the beam similarly to a 1:1 autotransformer [106, pp. 28–32]. The high power level signal chain alters the phase and the magnitude of the harmonic components of the input waveform, therefore a pre-distortion scheme was devised and applied to the input to counter this effect.

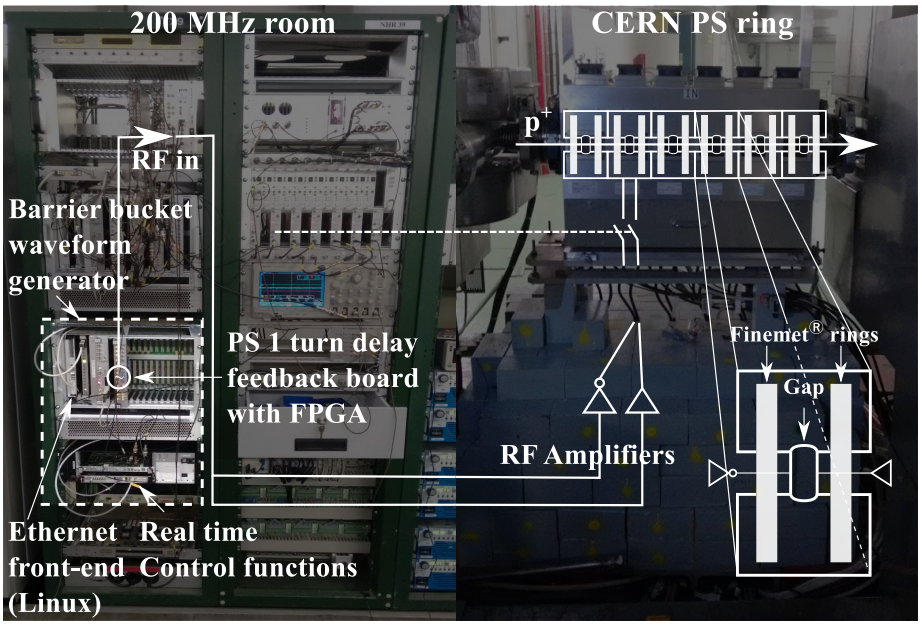

Figure 3.10: The prototype barrier bucket system as it is installed in the PS.

3.4.1 Transfer function - linear pre-distortion

In the first order of approximation, the high power level system is considered as a combination of linear elements. Therefore in order to establish the magnitude and phase adjustments this makes to the components of the input waveform, an S_{21} parameter measurement was performed from the input of the pre amplifier of the high power signal chain to the cavity return sum, which represents the

sum of the voltage of the six gaps of the cavity, see Fig. 3.10. The corresponding transfer function in the $0 - 20$ MHz range is shown on Fig. 3.11.

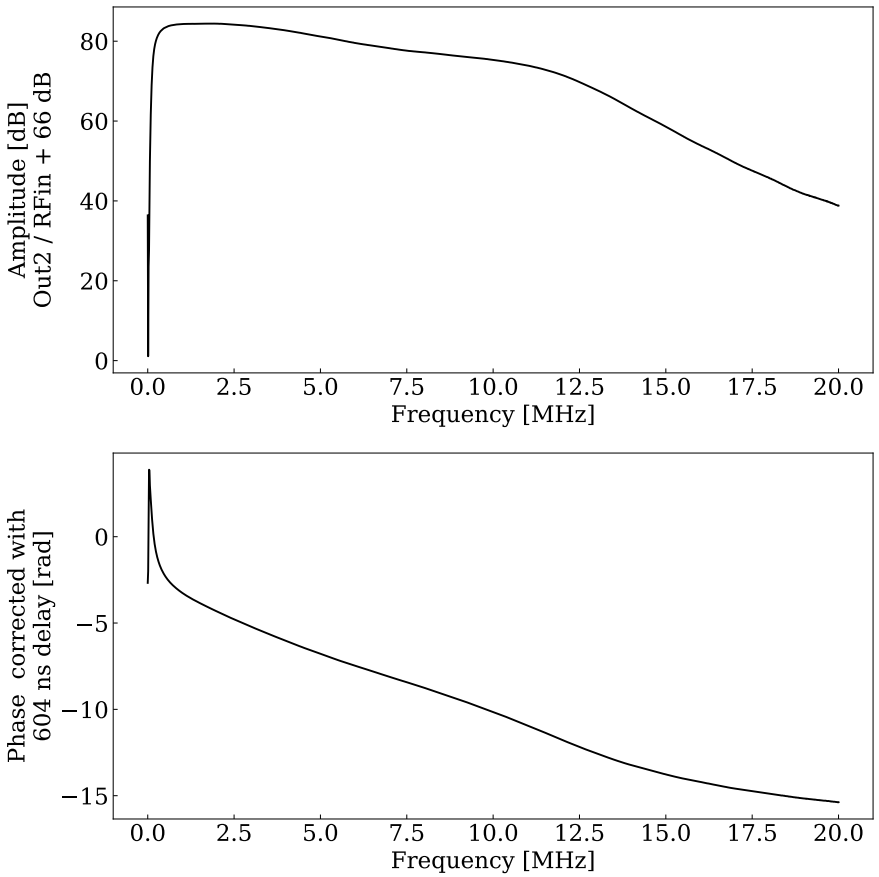

Figure 3.11: Measured S21 parameters from the RF input to the summed output of all the cavity cells corrected for the attenuation in the path to the VNA and the electrical delay from the input to the cavity installed in the ring.

Knowing the magnitude and phase shifts the system adds from the drive input to the cavity gap, the inverse of these are calculated. Then the harmonic components of the input waveform are modified accordingly: the magnitudes are pre-scaled and the phases are shifted. Examples of linearly pre-distorted waveforms can be seen in Fig. 3.12.

3.4.2 Limitations

At highest power outputs harmonic distortion is detectable. The third harmonic of the component having the highest amplitude in the wide band waveform was the most pronounced. The deviation compared to the expected linear behaviour

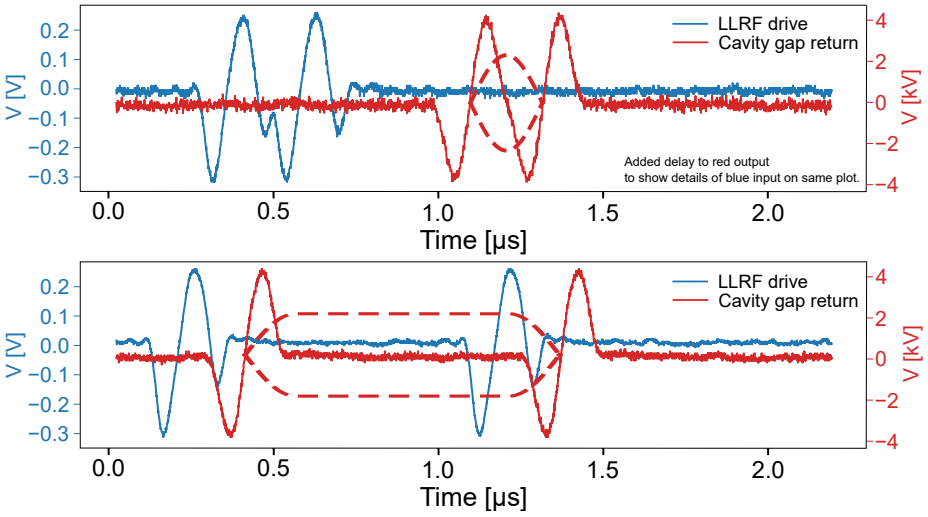

Figure 3.12: Pre-distorted input waveforms (blue) and cavity gap return waveforms (red) for the bucket stretching exercise with low intensity beam in barrier buckets. Note, the delay was added to the red waveforms to display it on the same plot.

was the highest, where these harmonics have a relatively higher amplitude, as illustrated by the yellow-orange curves of Fig. 3.13. The figure shows the ampli-

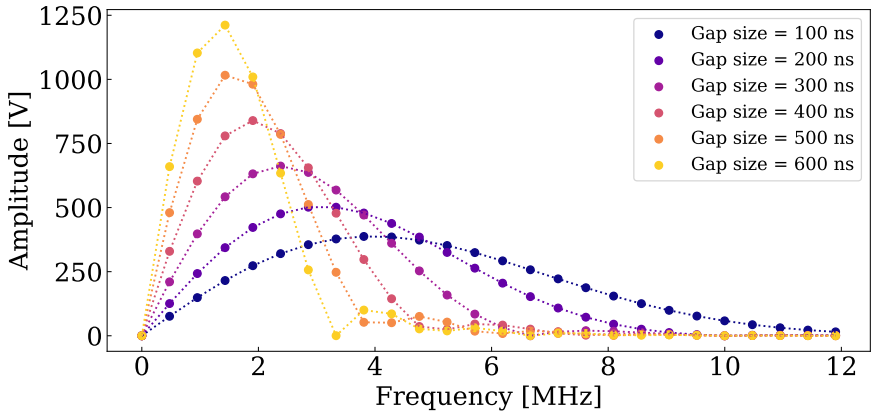

Figure 3.13: The first 25 sigma modulated harmonics used in the simulations for different gap sizes at the peak voltage of 4 kV.

tudes required for a 4 kV peak RF voltage. This means in practice that longer gaps than $300 - 400$ ns will have a ripple higher or equal than the few percent of the peak amplitude, since the present scheme does not have a compensation mechanism for this. This would make a significant distortion in the drift space.

However, gaps of this width are too long for the presently foreseen operational conditions, therefore this does not limit the effectiveness of the gap generation and were not investigated further.

The technical limitation of generating very narrow barriers is the available cavity bandwidth, as illustrated by the blue curves of Fig. 3.13 when compared with Fig. 3.11. However, the amplification in this domain is lower resulting in a lower waveform amplitude. Furthermore, to generate a shorter waveform combined with a low amplitude means a significantly lower integrated pulse strength as explained in Section 3.2.1, therefore the achievable bucket height is significantly less, too. This means in practice that much lower than 150 ns wide gaps are not feasible to achieve if a full depletion of the line density in the gap region is required.

Problems with the accuracy of the simple transfer function model were not observed during the approximately 6 months of tests with beam and measurements after the proton run stopped at the end of 2018. Nevertheless, it is important to point out that the accuracy of this pre-distortion depends on the accuracy of the transfer function measurements, since there is no feedback or correction mechanism applied. Note that Fig. 3.11 represents the latest state after the LS2 updates, measured in October 2020.

3.4.2.1 Potential improvements

Appendix A outlines a different way of synthesising the barrier bucket waveform utilising its basic symmetries in the complex plane, that could potentially be paired with a feedback system better than the current DDS-based version. This was not implemented for the beam tests, since the open loop configuration with a remote waveform update and linear pre-distortion was sufficient.

3.5 The barrier bucket RF system in BLonD

In order to simulate the longitudinal dynamics of the beam in barrier buckets, the barrier bucket system had to be modelled in BLonD. The pulsed RF voltage generating the barrier bucket has been modelled by the Fourier sum of 25 RF harmonics with sinusoidal amplitudes.

The simulation uses the same Python code base as the remote waveform generation, therefore there is no difference in the generation method between the simulated and physical waveforms. Naturally, in a floating point arithmetic, the fixed point limitations are not present, but the effects of these on the physical system are not pronounced given the sufficient resolution of the digital to analogue converters [153].

The starting point of the implementation is a so-called a single BLonD RF system with the output:

$$V_n(t) = M_n \sin\left(n\omega t + \phi\right) \ . \tag{3.18}$$

The magnitude M_n of one barrier harmonic for a given gap harmonic h is:

$$M_n = \sigma(n) b(n, h) \ . \tag{3.19}$$

The energy kick is calculated in electron volts in BLonD, therefore the voltages can simply be added to the energy term. Therefore the waveform synthesis happens at the energy kick calculation. This means that the waveform synthesis itself does not take added computational effort other than adding extra RF systems to the simulation.

$$\Delta E_i' = \Delta E_i + \sum_{j=0}^{n_{\mathrm{rf}}-1} V_j \sin(\omega_j \Delta t_i + \phi_j) \tag{3.20}$$

The harmonics of the RF voltage program are illustrated in Fig. 3.13 adding up to a peak voltage of 4 kV. The results of the simulations are presented in Chapter 4.

3.6 Summary

The voltage and the bandwidth requirements for a barrier bucket RF system for beam loss reduction were analysed and were found to be compatible with the capabilities of the Finemet® cavity and amplifier system already installed in the PS.

Different waveform shapes were investigated comparing their bandwidth and the barrier bucket parameters they provide. The bandwidth requirement and consequently the ringing of the waveforms can be limited by increasing the convergence of the Fourier series by the application of sigma factors resulting in smoother time domain waveforms. A sigma modulated, isolated sine pulse was selected for the beam tests conducted in this study as a compromise between bandwidth usage and achievable bucket area.

In order to realise the barrier bucket manipulation with beam, a beam synchronous, arbitrary waveform generator concept was developed based on swapping the sine look-up table of a conventional DDS with a remotely programmable waveform memory. The concept was implemented on a field programmable gate array and the drive successfully tested in the laboratory.

The LLRF drive was installed by the PS ring and integrated into the control system to perform beam tests. Since the signal chain from the waveform generator to the cavity gap alters the magnitudes and phases of the harmonic components of the input waveform, a linear pre-distortion scheme was devised and implemented. The linear model performs adequately within the foreseen operational parameters, but the limits of the scheme were also explored.

Finally, the barrier bucket system was implemented in a similar way to the actual drive in the longitudinal beam dynamics simulator, BLonD for numerical simulations.

Chapter 4

Beam tests and comparison with simulations

4.1 Introduction

The full validation of the low-level RF and power hardware completed, the strategy was to confirm the beam synchronous operation first at PS injection energy. The demonstration of this synchronisation was the objective of the initial tests. As shown in Sec. 4.3, more evolved manipulation schemes, like changing the azimuth of the barrier to shorten and stretch the bunch in the barrier bucket have been exercised at low energy to illustrate the behaviour of the beam in barrier buckets. Following the success at low energy, high energy beam tests were prepared by modifying the cycle for fixed target beams to include the barrier bucket operation alone, and later, the combination of the MTE with barrier buckets. Section 4.4 presents an analysis on the details of the longitudinal profile evolution at extraction and reports on the substantial beam loss reduction achieved in the PS.

In order to test the barrier bucket scheme with beam at the foreseen operational conditions to reduce losses, the acceleration cycle for the fixed target beams with MTE had to be modified as described in Section 4.4.1. The barrier bucket manipulation was added to the cycle after the acceleration in $h = 16$ buckets took place. This re-bucketing from the $h = 16$ buckets to the barrier bucket and the debunching are detailed in Section 4.4.2 which reports on a series of measurements with and without MTE. Simulations confirmed the observed behaviour of the beam before extraction.

Extraction of the beam from the PS to the TT2 transfer line with MTE was carried out. The results of the comparison of the longitudinal beam profiles

before and after extraction to highlight the contribution of the extraction kickers is summarised in Section 4.4.3. To check the effects of beam intensity on the quality of the longitudinal profiles at extraction an intensity scan is described in Section 4.4.4. The results were analysed and the effects of the impedance of the cavities on the shape of the longitudinal profiles at extraction was evaluated.

Following the analysis of the beam loss at extraction, it is concluded that the barrier bucket scheme reduces the losses at extraction significantly across the probed intensity range. As expected, the magnitude of the loss reduction depends on the size of the gap made by the barrier bucket system: a shorter gap results in a smaller loss reduction. As the length of the gap in time approaches the duration corresponding to the rise time of the extraction kickers, more than an order of magnitude loss reduction is achieved in the extraction region at high beam intensity as described in Section 4.4.5.

The results presented in this chapter are based on signals from beam observation equipment, namely a wall current monitor (WCM) installed in the PS ring, a wide-band electrostatic pick-up (WBP) in the TT2 transfer line and two PS beam loss monitor (BLM) systems. The working principles of these devices are introduced int the following Sections.

4.2 Measurement signals

The devices measuring the longitudinal line density in the PS ring and in the TT2 transfer line are introduced in Sections 4.2.1 and 4.2.2. The integrated beam loss was measured by two beam loss monitor systems in the PS briefly presented in Section 4.2.3.

4.2.1 Wall current monitor

Most of the measurement data reported in this chapter was acquired by a device called Wall Current Monitor (WCM). Such a device installed in straight section 03 of the PS ring [156].

The device acts as a current to voltage transformer similar to a simple resistor [157–159]. The passing beam induces an equal and opposite local image current indicated in Figure 4.1. This image current generates a voltage when it reaches a gap in the beam pipe. More precisely, the voltage is an electromagnetic pulse and is confined in a cylindrical geometry surrounded by a conductor labelled detector cavity in Fig. 4.1. To increase the inductance and thereby decrease the lower cut-off frequency of the device, the cavity is loaded with Ferrite toroids. Absorbers damp the detector cavity resonances to improve the quality of the signal towards the upper end of the device's bandwidth.

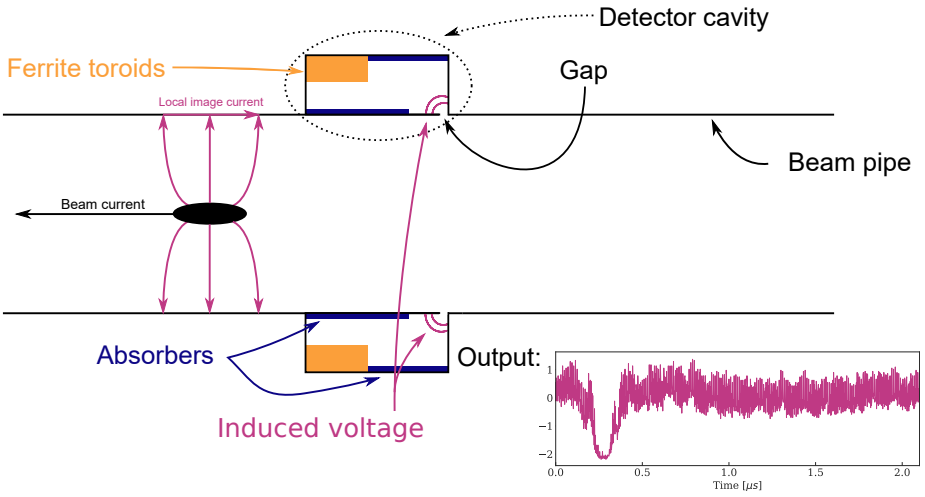

Figure 4.1: Sketch of the longitudinal cut of the Wall Current Monitor installed in the PS illustrating its principle of operation.

The lower cut-off frequency is about 100 kHz, which is less than the quarter of the PS revolution frequency, therefore it contains the relevant parts of the spectrum of the longitudinal profiles. This device can not measure DC currents since the cavity material is conducting providing a shunt. The upper frequency cut-off is limited by the gap capacitance and it is about 4 GHz [160, 161]. However, despite the presence of the absorbers, the higher end of the spectrum is dominated by cavity resonances [161]. The bandwidth used in these studies was from 100 kHz to 500 MHz. The upper end was limited by the 1 ns sampling rate of the acquisition system.

To observe the profile evolution, which happens on a longer scale than one turn, the WCM acquisition is typically repeated with a given interval along one part of the cycle, as illustrated in Figure 4.2. Assuming adiabatic manipulations, the profiles of consecutive turns in a synchrotron are very similar. Therefore for economical data logging, depending on the beam manipulation, several turns of logging can be skipped without the loss of information on the profile evolution.

4.2.2 Wide-band, electrostatic pick-up

In order to compare the longitudinal beam profile before and after extraction from the PS, it was measured before extraction in the PS and after in the TT2 transfer line. The device providing the transfer line profiles is introduced in this section.

The wide-band pick-up (WBP) currently named BPMW208 [162], previously UES208, with 4 tetrahedron-shaped electrodes forming a cube [163] is installed

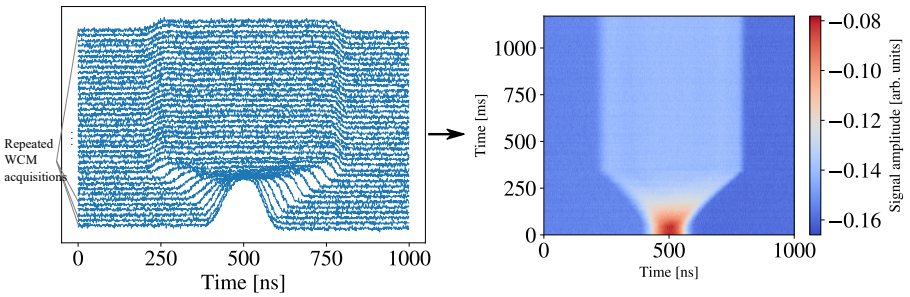

Figure 4.2: Illustration of the plots from a WCM. Two time axis are used, the x time axis is during a fraction of the turn and the y time axis is showing repeated acquisitions along a cycle on a longer time scale. Left: acquisitions as a mountain range plot. Right: the same acquisitions as on the right displayed as an image with the signal amplitude colour-coded.

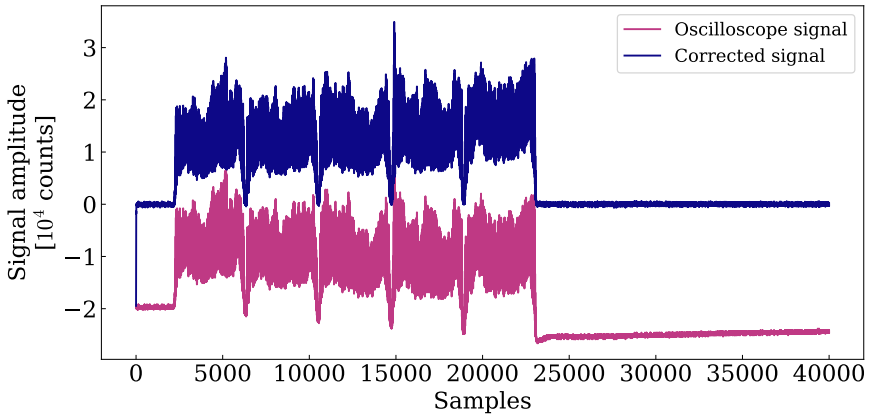

Figure 4.3: An example of the raw acquisition from the oscilloscope and the corrected beam profile.

in the TT2 transfer line in the beam pipe. The signal from the capacitive pick-up is impedance transformed using high input impedance and low output impedance buffer amplifiers [164] to also preserve the low frequency part of the beam signal. The acquisitions are five times longer in time, therefore their lower frequency components are more relevant than in the case of the WCM. The electrode signals are summed via an RF hybrid [165] and then connected to an oscilloscope. The −3 dB bandwidth of the device installed in the transfer line is about 5 kHz−400 MHz.

A slight correction in post processing was needed to compensate for the baseline and still, the low-frequency cut-off of the system. Figure 4.3 shows an example of the acquisition from the oscilloscope and the filtered waveform. To compensate for the baseline of the acquired signal, a custom discrete-time

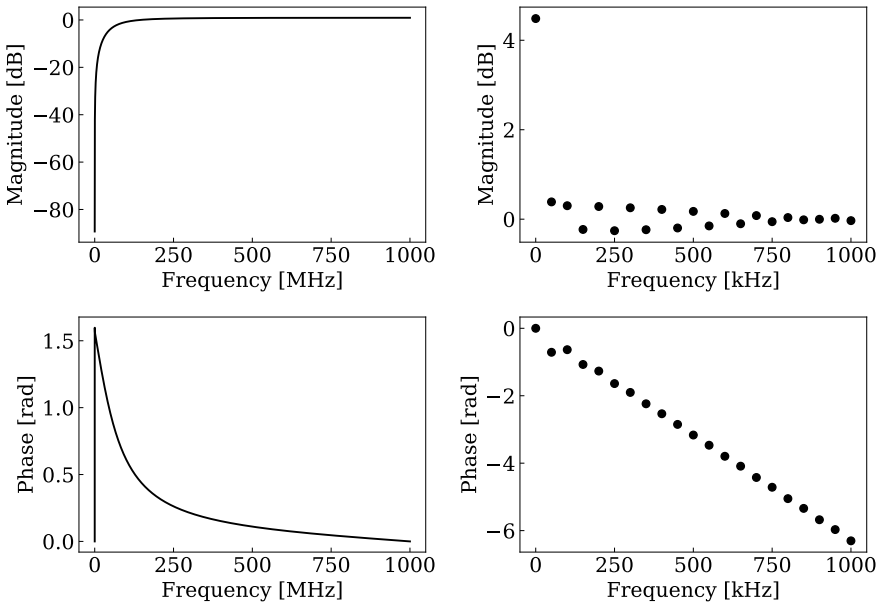

Figure 4.4: Frequency responses of the compensation used for the pick-up signal. The droop was compensated for by a high pass filter (left). Then it was replaced by an integrator (right) for compensating for the losses on the low end of the spectrum due to the low frequency cut-off of the acquisition. The sample spacing is 0.5 ns, which explains the 1 GHz length of the full Nyquist range.

infinite impulse response filter was applied in post processing, as a part of a standard collection of routines [166] developed for data analysis. The filter has two operational modes. It is a high-pass filter when the beam is absent, acting as a baseline corrector as shown in Fig. 4.4 at the beginning and the end of the blue trace. In the second mode, it is operated as a compensator for the

low frequency cut-off of the acquisition system when the beam is present. The frequency response of the two modes is shown in Fig. 4.4, the baseline corrector on the left-hand-side and the low frequency cut-off compensator on the right-hand-side. See Figure 4.3 for an example input and output. The analysis of the discrete time filter was performed as part of these studies.

4.2.3 Beam Loss Monitors

When the particles of a beam hit parts of the accelerator, usually the beam pipe, they generate a shower of secondary particles that can be detected using a range of methods [167, 168]. A state-of-the-art beam loss monitor (BLM) is capable of measuring the energy deposited by these particles over time, which is dependent on the type of the radiation at a given site in the accelerator. The relationship is usually established using Monte Carlo simulations [169–173].

The BLMs in the PS are ionisation chambers attached [174] to all 100 main magnets [175, pp. 71–158], signalling the location of the integrated beam loss along the ring. The current measured from the BLM [176, pp. 593–5] is integrated over a cycle, representing the deposited charge relating to the beam loss. The signal from both, the old measurement system in the PS [177, 178], which is only capable of a relative measurement, and the new, high dynamic range and calibrated BLM system [179–181] was used in the analysis in Section 4.4.5. The particularly interesting region for our studies over straight sections 14-17, which contain the dummy and extraction septa. This is where the beam is expected to hit the accelerator first as explained in Section 1. The barrier bucket scheme is expected to reduce the integrated beam loss, as mentioned in Section 1.

4.3 Low energy and low intensity studies

When the barrier bucket RF system was used with beam for the first time, simple tests were performed to see the interaction of the beam with a single potential barrier produced per turn at injection, this is detailed in Section 4.3.1. Producing two barriers per turn allows to check the adiabaticity of the manipulations with moving barriers. Section 4.3.2 presents the results of simulations and beam tests performed with azimuthally moving barriers. The barrier speed limits predicted by Section 2.3.2 confirmed by both simulations and measurements. The key beam parameters used in the low energy and low intensity studies are in Table 4.1.

Parameter name	Symbol	Value
Kinetic energy of the beam	E	1.4 GeV
Maximum energy offset	ΔE	2.1 MeV
Intensity	N	10^{11} ppp
Average beam current	I_{b}	6.4 mA
Peak RF voltage	V	$3-4$ kV
Revolution period	T	2.29 μs
One-sided barrier excursion in time	$t_{\mathrm{d}}/2$	300 ns
One-sided barrier excursion in azimuth	$\phi_{\mathrm{d}}/2$	7.5°
Time range of the manipulation	t_{m}	20 ms – 1 s
The range of the relative phase velocity	$\lvert\dot{\phi}_b/\dot{\phi}_f\rvert$	0.01 – 0.25

Table 4.1: Parameters used for the low energy simulations and beam tests.

4.3.1 Reflection at barrier during debunching

One bunch from the PSB was injected in the PS and solely the barrier RF system was turned on. The first goal was to find the azimuthal position of the barrier created each turn. By scanning the azimuthal position of the injected bunch, the newly created barrier was found. Figure 4.5 (top) shows the RF voltage and the potential barrier made during half of a PS turn. Fig. 4.5 (bottom) shows the profile evolution of two separate acquisitions with the same azimuthal barrier position, but different bunch injection positions on two sides of the barrier. The phase of the barrier was found by the protons reflecting off both sides of the barrier. The barrier waveform was also inverted to check that the expected bunching is observed instead of reflection. Although not shown here with low energy beam, the bunching with high energy beam can be seen in Fig. 4.16 (left).

4.3.2 Bunch length manipulation using moving barriers

While the strategy to inject the beam directly into a barrier bucket was sufficient for the phase calibration of the system, it is not sufficient for more elaborate beam tests. This is because the barrier bucket system can not provide sufficient voltage for a matched capture of the beam at injection from the PSB. Nonetheless, it is possible to create a matched initial condition for beam manipulations with the barrier bucket system alone. To begin with, one needs an isolated bucket, which can be made by placing two isolated sinusoidal pulses next to each other as shown in the bottom of Fig. 4.6. To match the beam distribution to the isolated bucket created by these two isolated pulses, a blow-up with the 200 MHz system was performed. As a result, some particles were not captured in the bucket between the two barriers, which need removal not to interfere with the subsequent moving barrier tests. In order to achieve this, a transverse kicker sufficiently fast to remove the uncaptured beam in one turn was chosen, because

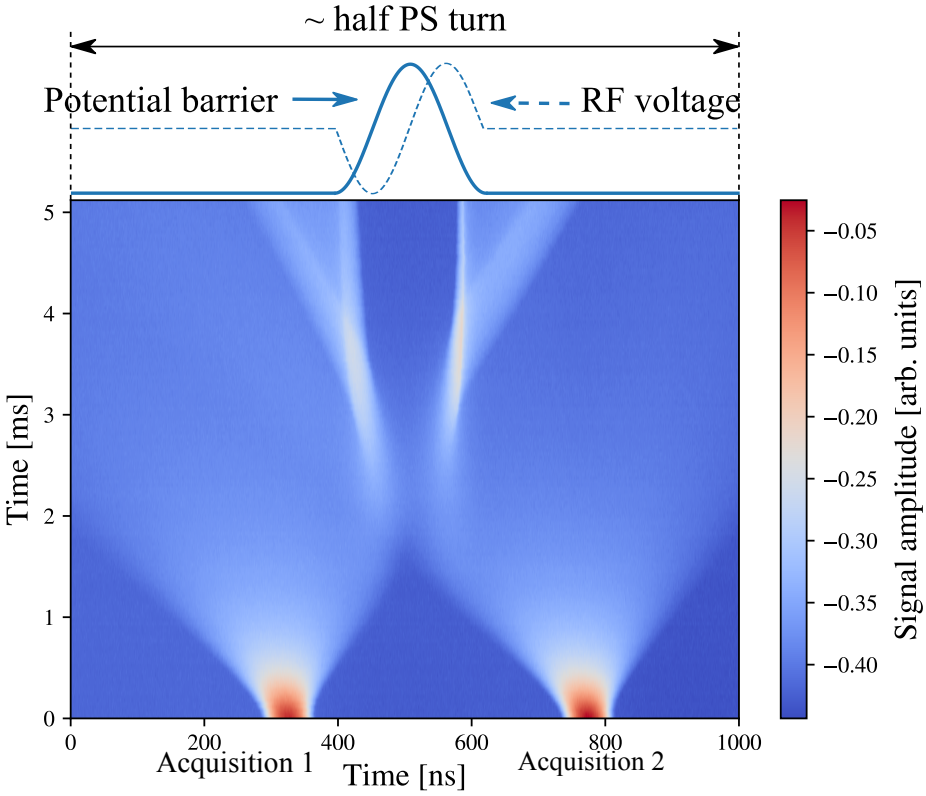

Figure 4.5: Protons reflecting off the right hand side and left hand side of the potential barrier in a barrier bucket. Two longitudinal profile evolutions were combined in this plot. Injecting the beam on the left hand side of the barrier at about 320 ns and injecting on the right hand side of the barrier at about 700 ns. The top of the image shows the RF voltage and the corresponding potential.

this allows to keep the beam in the conventional bucket between the barriers, while removing the rest of the particles still circulating outside the isolated, conventional bucket. A matched initial condition to start the manipulation is thus achieved. Then the two barriers moved in azimuth to stretch the beam in the bucket as shown in Fig 4.6.

The key parameters of the manipulation are summarised in Table 4.1.

4.3.2.1 Flatness of the line density

The beam was decompressed to barrier buckets of different drift space lengths to observe the flatness of the line density. Optimisation of the input waveform was performed to achieve a nearly perfectly flat line density during such an operation as it can be seen in Fig. 4.7.

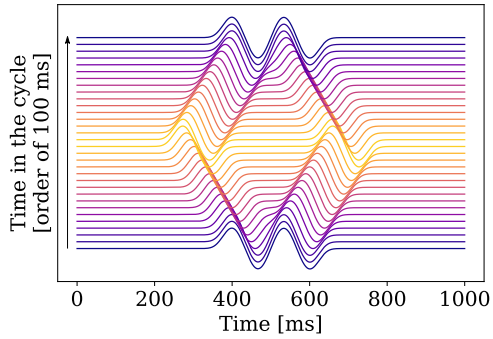

Figure 4.6: Illustration of the RF program during a decompression and compression operation. The blue traces generate a conventional, isolated bucket. The other traces generate barrier buckets with increasing drift space from purple to yellow.

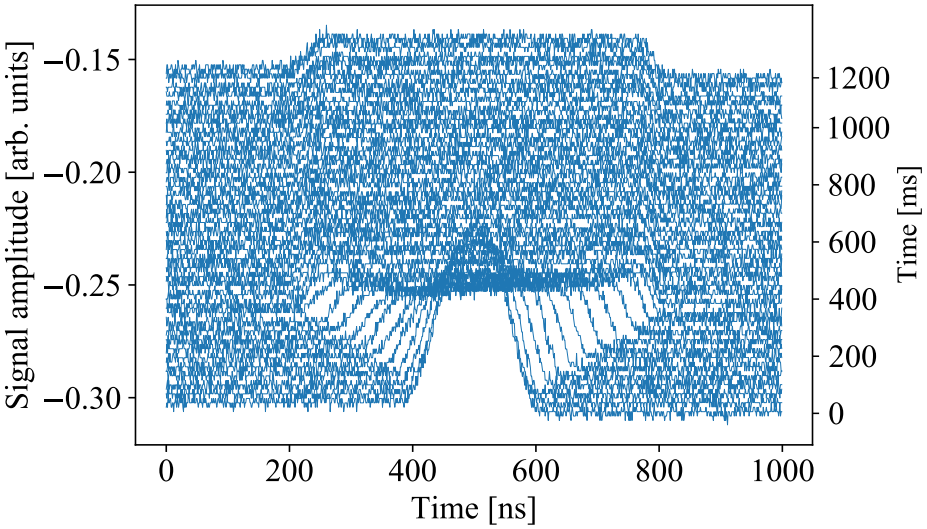

Figure 4.7: Measured longitudinal line density profile evolution of a decompression operation with moving barriers.

4.3.2.2 Simulations

Before moving onto tests to check the effect of different barrier speeds on the profile evolution, simulations with moving barriers are discussed in order to compare the results of the measurements with the results of these. Figure 4.6 illustrates a voltage program of the simulations.

As in the real tests, the beam was matched to a conventional RF bucket created by two barrier RF pulses right next to each other at the beginning of the simulations. The initial conditions of this bunch in the isolated bucket were matched using tomography [182] based on measured reference profiles similarly to the method used in the high energy case, see Fig. 4.17. Then the two, isolated pulses were moved apart to expand the isolated bunch into a bunch in a barrier bucket and compress to a bunch in a conventional bucket again as

shown in Fig. 4.6.

The main challenge of the simulations using BLonD [129] was to model the wide-band RF system, as it is outlined in Section 3.5. To compress and expand the beam, only the phase of the individual harmonic components was linearly increased and decreased again. The main accelerator and beam parameters used in these simulations are summarised in Table 4.1.

Since the intensity of the beam is very low, the beam induced voltage was neglected in these simulations. The results of these simulations are directly compared with measurements in the next section.

4.3.2.3 Comparison of measurements with simulations

The result of the estimation performed based on Section 2.3.2 is that the barrier pulse speed should be such that the ratio of the barrier phase velocity to the maximum phase velocity is $|\dot{\phi}_b/\dot{\phi}_f| \ll 0.5$. The duration of compression and expansion, t_c, was varied in a range of 10 ms to 300 ms. In all cases the bucket was stretched to a maximum drift space of 600 ns and compressed back again. Although the upper speed is still well below the optimistically defined limit, it became clear during the tests that approaching even a fifth of this value results in a significant perturbation of the bunch profile. Similar observations have been reported in [45].

In the first tests, the barriers were receding and approaching only, therefore the total time of the manipulation was $2t_c$. When $t_c = 10$ ms, corresponding to $\dot{\phi}_b/\dot{\phi}_f \approx 0.25$, the decompression and compression results in a highly perturbed profile after the manipulation as it is shown in Fig. 4.8, which shows the bunch length measured as a Gaussian fit. The barrier bucket part can not be approximated this way, thus it was removed from the middle plot. Therefore these tests are suitable to calculate the perturbation or oscillation of the resulting longitudinal line density profiles. However, when the speed of the barriers were much slower corresponding to about $\dot{\phi}_b/\dot{\phi}_f \approx 0.01$, the original bunch profile was restored after the manipulation as it can be seen in Fig. 4.9.

In the subsequent tests a different timing was used aiming to measure the filamented bunch length at the end of the manipulation rather than the oscillations as in the previously mentioned tests. This means that the total time was kept as long as it was possible in the cycle, and an intermediate filamentation phase in the created barrier bucket was added. The probed barrier speed range was kept the same. Figure 4.10 shows the results of a fast, non-adiabatic manipulation, whereas Fig. 4.11 presents an adiabatic manipulation with a slow barrier movement. It is clear from the simulated and measured profile evolution, that the measurements agree with the simulations to a high degree in all

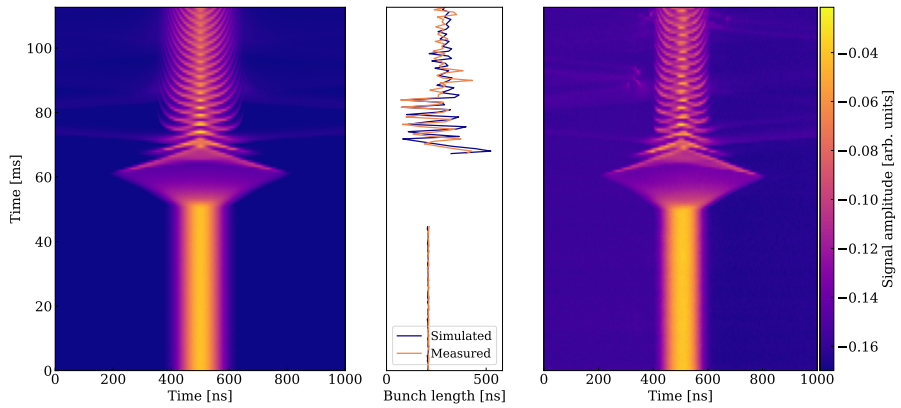

Figure 4.8: Evolution of the bunch profile during fast compression and expansion at $\dot{\phi}_\mathrm{b}/\dot{\phi}_\mathrm{f} \approx 0.25$. The oscillations after 60 ms are a clear indication of a non-adiabatic manipulation. Simulated (left) and measured (right) profiles are shown. The plot in the middle show the bunch lengths, highlighting the oscillations at the end.

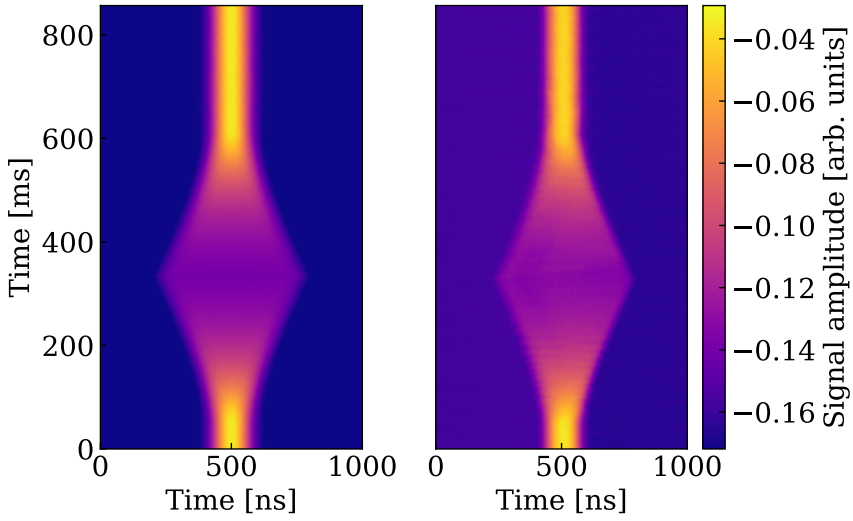

Figure 4.9: Evolution of the bunch profile during slow compression and expansion at a normalised speed of $\dot{\phi}_\mathrm{b}/\dot{\phi}_\mathrm{f} \approx 0.01$. The smooth transitions indicate an adiabatic manipulation. Simulated (left) and measured (right) profiles are shown.

cases.

Performing Gaussian fits to the beam distribution before and after the compression, the bunch lengths before the expansion operation and after the compression are compared for two schemes of barrier motion, and the results are

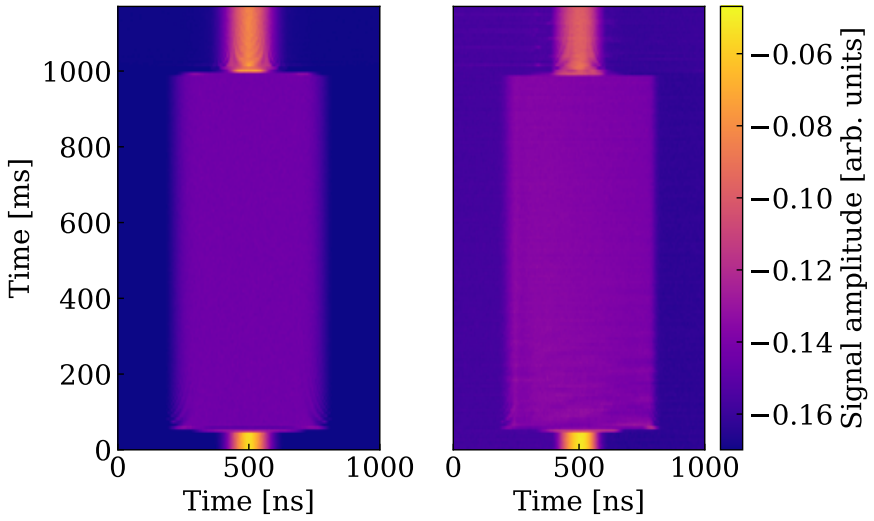

Figure 4.10: Evolution of the bunch profile during fast compression and expansion at $\dot{\phi}_\mathrm{b}/\dot{\phi}_\mathrm{f} \approx 0.25$. The increased bunch length at the end of the manipulation shows a non-adiabatic manipulation. Simulated (left) and measured (right) profiles are shown.

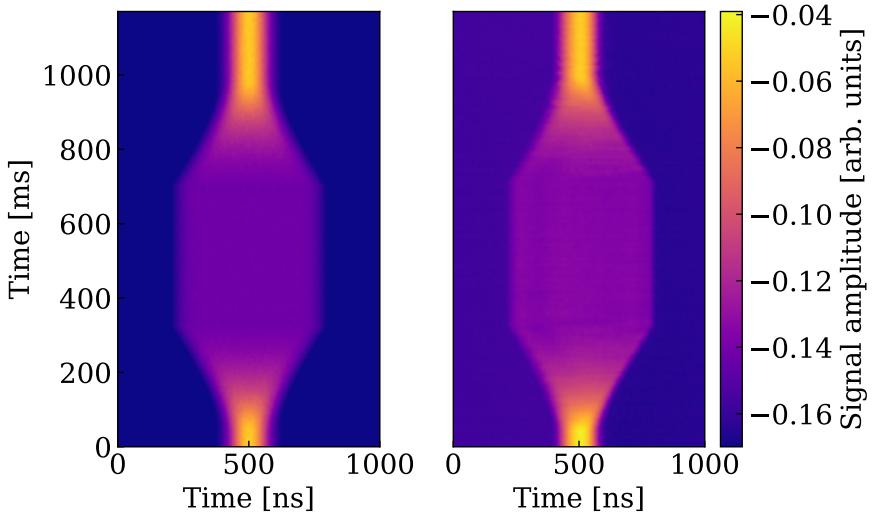

Figure 4.11: Evolution of the profile during slow compression and expansion at $\dot{\phi}_\mathrm{b}/\dot{\phi}_\mathrm{f} \approx 0.01$. Bunch profiles at the end are restored indicating an adiabatic manipulation. Simulated (left) and measured (right) profiles are shown.

shown in Fig. 4.12. It is clear that once even the fifth of $|\dot{\phi}_\mathrm{b}/\dot{\phi}_\mathrm{f}| = 0.5$ is approached, the difference in the bunch length increases significantly. In addition,

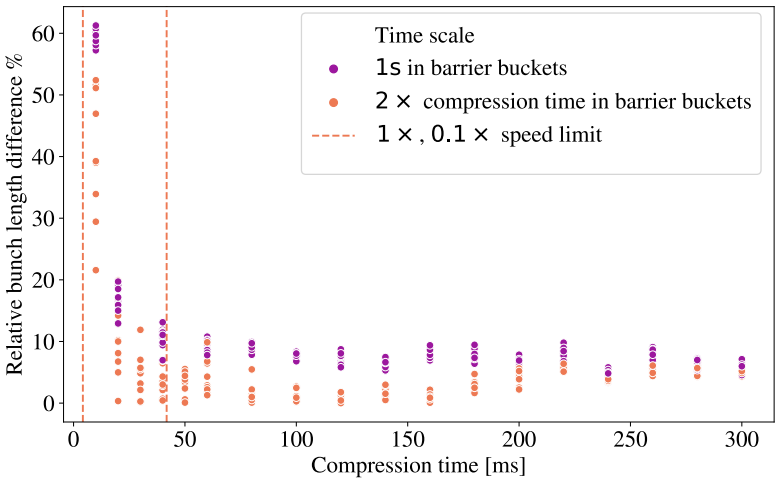

Figure 4.12: Difference of initial (200 ns) and final bunch length versus compression and expansion. Each marker on the time axis having categorical labels has two associated boxes for the two schemes with the marker in the middle, except for 30 ms and 50 ms. Once the compression speed is near the theoretical limit, the bunches are perturbed after compression resulting in a not well defined or large bunch length due to the fast manipulations. Plot uses the same data as Figure 4. in [2] (CC-BY), but the improved speed limit from Chapter 2 is also shown.

the data taken for the shorter beam manipulations show that the bunch length spread increases for larger barrier speeds as a result of quadrupolar oscillations of the final bunch. This view of the experimental data in Fig. 4.12 supports the expected conclusion that approaching the optimistically-defined barrier speed limit results in a non-adiabatic compression.

4.4 Studies at high energy

As outlined in Chapter 1, the aim of the studies is to reduce beam losses for fixed target beams at the transfer from the PS to the SPS. The PS injection during these studies was at 1.4 GeV kinetic energy and extraction happens at 14 GeV/c momentum. The barrier bucket RF system can not accelerate the beam with the required ramp rate, since the maximum voltage it achieves is not sufficient [31]. Therefore the main RF system [183, 184] operated at $h = 16$ is used to reach the beam momentum of 14 GeV/c. Then, at flat-top, the beam is re-bucketed in a barrier bucket.

Although sufficient for the acceleration of the beam, a single harmonic RF system is unsuited to create a barrier bucket required for the beam loss reduction, because it can not generate a wide-band waveform. Hence re-bucketing from the main RF system to the barrier bucket system is needed before extraction.

Given these requirements, beam tests at extraction energy were performed [1, 2]. A convenient choice to start was to modify the operational acceleration cycle for the beam for fixed target experiments [185] as summarised in Section 4.4.1. The challenge was to find a way to accommodate the barrier bucket manipulation in a highly optimised cycle [16, 21, 22], while keeping the benefits of MTE. Adding a re-bucketing operation from the $h = 16$ buckets to a barrier bucket at 14 GeV/c momentum near extraction is compatible with the requirements of the RF acceleration and handover and the limitations imposed by the maximum duration of the existing cycle.

The description of the re-bucketing from the $h = 16$ buckets to a barrier bucket is presented in Section 4.4.2 accompanied by simulations and measurements with beam. To understand the longitudinal profile modulation due to the drift of the particles around the barrier, a beam test and simulations with a longer debunching time were also performed in addition to the operational, shorter debunching duration. During this longer operation, the transverse splitting was disabled.

To observe the efficiency of the barrier bucket operation with the transverse splitting, the latter was activated. The beam was extracted during five turns. Section 4.4.3 compares the longitudinal profiles in the accelerator and the unfolded longitudinal structure in the TT2 transfer line spanning five turns in time. Variation of the longitudinal profiles depending on the intensity of the beam is analysed in Section 4.4.4. Finally, Section 4.4.5 presents the main achievement of the study, the significant beam loss reduction at extraction.

4.4.1 The acceleration cycle for the fixed-target beam in the PS

As illustrated in Chapter 1, the beam is injected into the PS from rings 3, 4, 2 and 1 of the PS Booster (PSB), in this order, with the principal harmonic number being $h = 2$. The injection takes place at 1.4 GeV kinetic energy, upgraded [176, pp. 285–90] to 2 GeV [186, 187] of the accelerators. Since the circumference of the PS is four times longer than the one of the PSB, the bunch-to-bucket transfer requires an RF capture at $h = 8$ in the PS. The RF voltage programs for $h = 8$ and $h = 16$, as well as the current programs for the magnetic elements involved in the transverse splitting are shown in Figure 4.13 for the whole acceleration cycle.

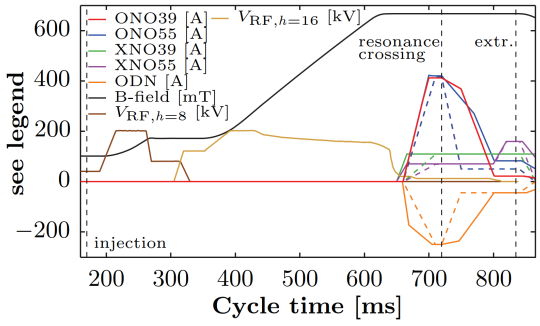

Figure 4.13: The current of the different magnetic elements taking part in the transverse splitting, the magnetic flux density along the cycle and the RF voltages peaking at 200 kV are shown. Figure taken from [16], Figure 3 (top). Copyright CERN, 2016 CC-BY licence.

To suppress longitudinal instabilities during the PS cycle, a controlled longitudinal emittance blow-up with a phase-modulated 200 MHz system is performed. After accelerating to an intermediate magnetic plateau at 3.5 GeV/c, an additional longitudinal emittance blow-up is applied, to mitigate instabilities when crossing transition.

At the same time a splitting from 8 to 16 bunches is accomplished by changing the main harmonic to $h = 16$. The beam is then accelerated through transition energy to the magnetic flat top at 14 GeV/c momentum. At this point the beam is transversely split into four islands and a core. Then a debunching process is realised by decreasing the amplitude of the main RF system at 7.6 MHz ($h = 16$) down to zero. At the very end of the cycle, just before extraction, the 200 MHz system is pulsed for 1 ms to modulate the longitudinal beam structure and ease the injection capture in the SPS with its main RF system at 200 MHz.

The operational cycle was modified for beam the tests to include the handover to the barrier bucket RF system [1, 2]. One barrier per waveform was generated to cover the rise time of the extraction kicker. These modifications take place a the end of the cycle, after the main RF amplitude is dropped

from 200 kV to about 12 kV and the transverse splitting to took place. An exception to this was the tests without the transverse splitting. In this case about 50 ms time was gained in some of the tests to study the re-bucketing process longer.

The key beam parameters used in the high energy studies are summarised in Table 4.2.

Parameter name	Symbol	Value
Revolution period of the PS	T	2.1 μs
Momentum	p	14 GeV/c
Intensity	N	4×10^{12} ppp – 2.2×10^{13} ppp
Average beam current	I_{b}	0.3 A – 1.7 A
Total initial longitudinal emittance	ϵ	25 eVs
Peak RF voltage	V	$3 - 4$ kV
Length of the gap in time	t_{gap}	150 ns – 300 ns
Duration of the manipulation	t_{m}	≈ 20 ms

Table 4.2: Parameters used for the high energy simulations and beam tests with one barrier pulse per turn.

4.4.2 Re-bucketing and debunching into a barrier bucket

As described in the previous section, the beam is accelerated to 14 GeV/c using $h = 16$ buckets, since the main RF system has sufficient peak amplitude to achieve this opposed to the barrier RF system. Therefore to achieve a gap in the debunched beam at extraction a re-bucketing from the $h = 16$ buckets to the barrier buckets must take place driven by an RF handover from the main, single harmonic RF system to the barrier bucket wide-band system. The details on how to perform this handover were first tried experimentally at the end of run 2 of the LHC operation.

4.4.2.1 RF handover and observations with beam

One barrier waveform generating a gap was programmed per turn by lowering the amplitude of the main RF system at $h = 16$ and, at the same time, increasing the amplitude of the wide-band system. The voltage program and the corresponding RF waveform evolution is shown in Figure 4.14 top. During the tests, the azimuthal position of the barrier was varied and the longitudinal profile evolution was observed. The symmetry of the profiles at extraction around the gap depend on the azimuthal position of the barrier bucket with respect to the position of the conventional buckets. If the RF phase corresponding to the unstable fixed point of both buckets is not aligned, the resulting longitudinal

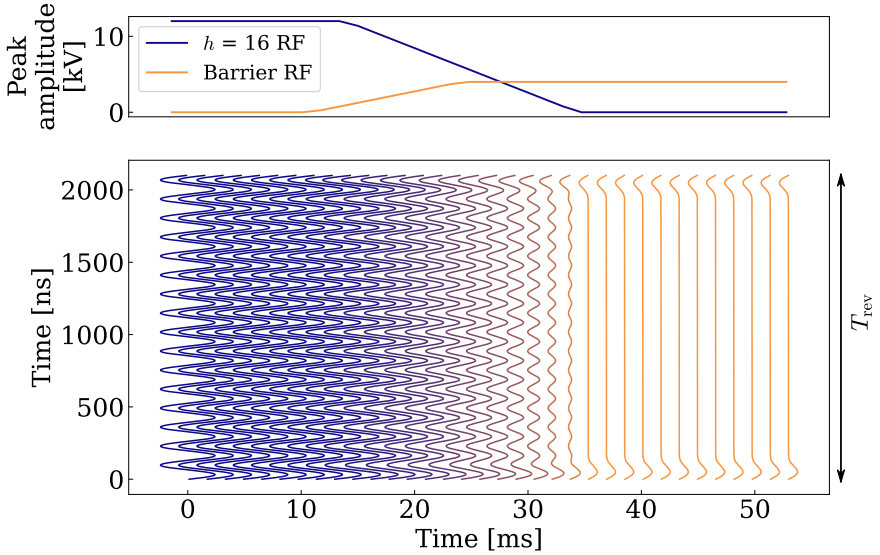

Figure 4.14: Total RF voltage evolution during re-bucketing with peak amplitudes (top) and waveform (bottom).

profiles become asymmetric around the gap region. Simulations presented later in this section provide an explanation for this observation.

This observation then defined the relative phase of the barrier RF system and that of the conventional RF system during the re-bucketing. It can be observed in Fig. 4.14 that the zero crossing and the sign of the slope of the half pulses generating a conventional and a barrier bucket are the same resulting in the alignment of the unstable fixed points of the buckets.

Using an aligned RF program, profile evolution that is symmetrical around the gap was observed see Fig. 4.15.

Apart from the positioning of the gap with respect to the bunches, RF waveform imperfections can cause uneven profiles at extraction, too. A few number of tests were performed to investigate the effects of RF waveform distortions.

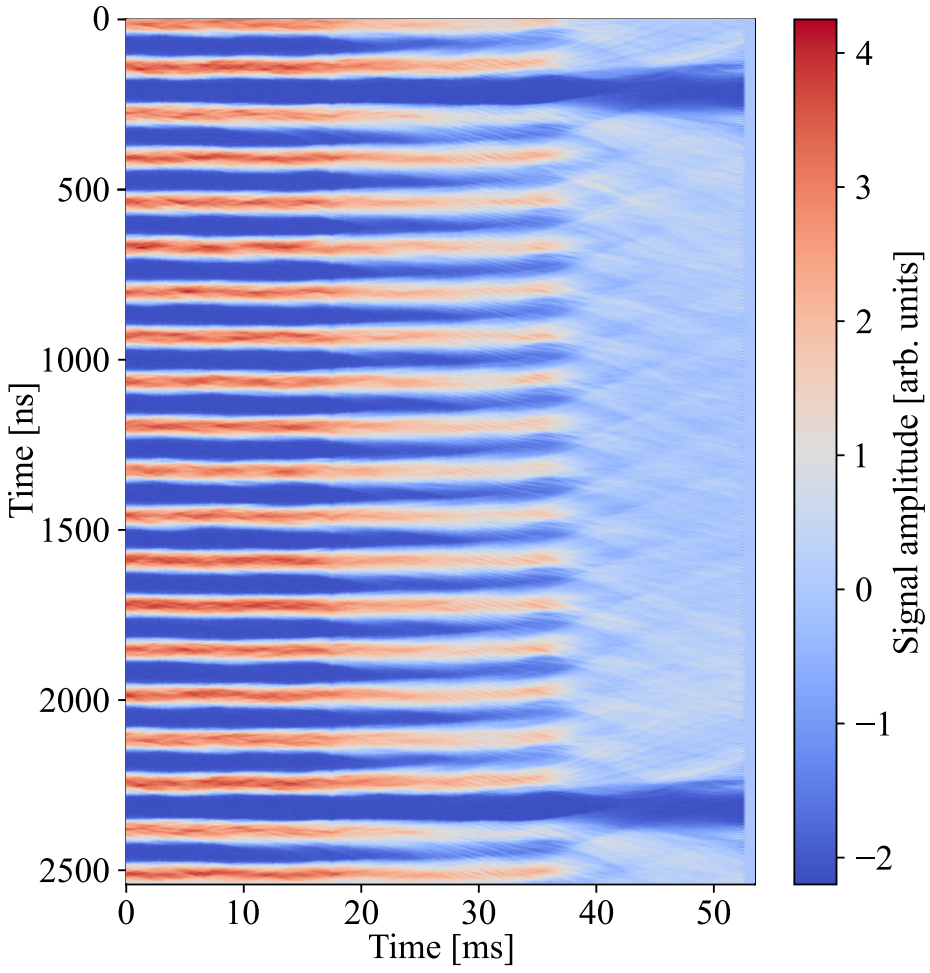

Figure 4.15: Re-bucketing into a barrier bucket at total beam intensity of 1.87×10^{13} ppp.

4.4.2.2 RF waveform imperfections and drift

Inverted and distorted barrier waveforms were generated to trap the beam in sub-buckets near the gap region. Figure 4.16 shows three measurements with different RF waveforms. Fig. 4.16 (left) illustrates the measured longitudinal

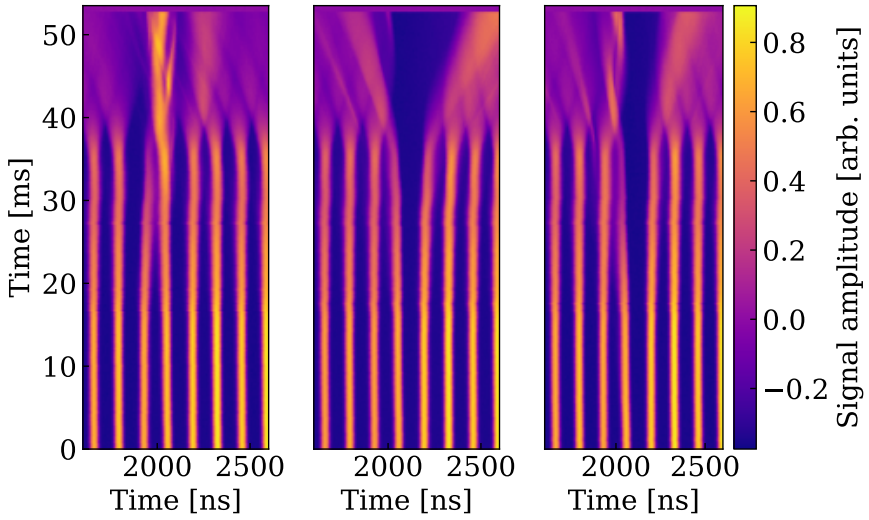

Figure 4.16: Comparison of line-density modulations during the handover from the conventional to the barrier bucket RF system. Left: re-bucketing to an isolated bucket. Centre: modulation due to drift of particles. Right: modulation due to both potential-well distortion and particle drift.

profile evolution corresponding to an isolated bucket made by an inverted barrier bucket waveform. The merging of two bunches can be observed from 20 ms. The measurement in the centre plot highlights the reflection around the gap region with a conventional barrier RF waveform as reported earlier in this section. During the measurement shown in the right figure, an inverted RF pulse right next to the barrier generating the pulse was made. This plot shows both phenomenon on two sides of the gap. The bunching can be observed on the left-hand-side of the gap, where the sub-bucket was made by generating an RF ripple. On the right-hand-side of the gap, the longitudinal profile evolution consistent with particles reflecting off the potential barrier can be seen.

4.4.2.3 Simulations

To analyse the bunch distribution at extraction, numerical simulations with the longitudinal tracking code BLonD [129] have been performed. Appendix B contains further details on the simulation framework and the code developed for the barrier bucket simulations.

4.4.2.4 Matching of the initial conditions

Most tests were performed with the time frame corresponding to the voltage evolution shown in Fig. 4.14. Hence the same RF program was used in the initial simulations.

Apart from the RF voltage, the distributions were also matched. The particle distribution in the longitudinal phase space and its corresponding emittance during acceleration can be reconstructed based on a set of bunch profiles using tomography [182]. To observe the fundamental beam dynamics during re-bucketing, a matching of the measured distribution based on a parabolic beam distribution was performed. Although a more sophisticated method exists [188], this simple approximation was sufficient to simulate the fundamental behaviour of the beam without intensity effects.

A set of longitudinal profile evolutions having different emittances were generated using BLonD. The reference profiles were available at the end of the intermediate flat top, hence the RF parameters were matched to those earlier in the cycle. These profiles were exported from the simulation and the same tomography algorithm was run on them as on the measured profiles. Figure 4.18 illustrates the reconstructed profiles from simulations and the reconstruction from the measurements see Fig. 4.17. The emittance corresponding to the lowest error in the RMS emittance, the 90% emittance, the matched area and dp/p was chosen. Approximately 1% agreement was achieved for all four parameters.

A minor longitudinal blow-up, 10% was added, since levels below this can be expected from the moment of the emittance measurement, around C350 in the cycle, and the start of the re-bucketing process to the barrier bucket around C800. This is because the reference profiles were only available after transition crossing at the end of the intermediate flat top, but before the acceleration in the $h = 16$ buckets.

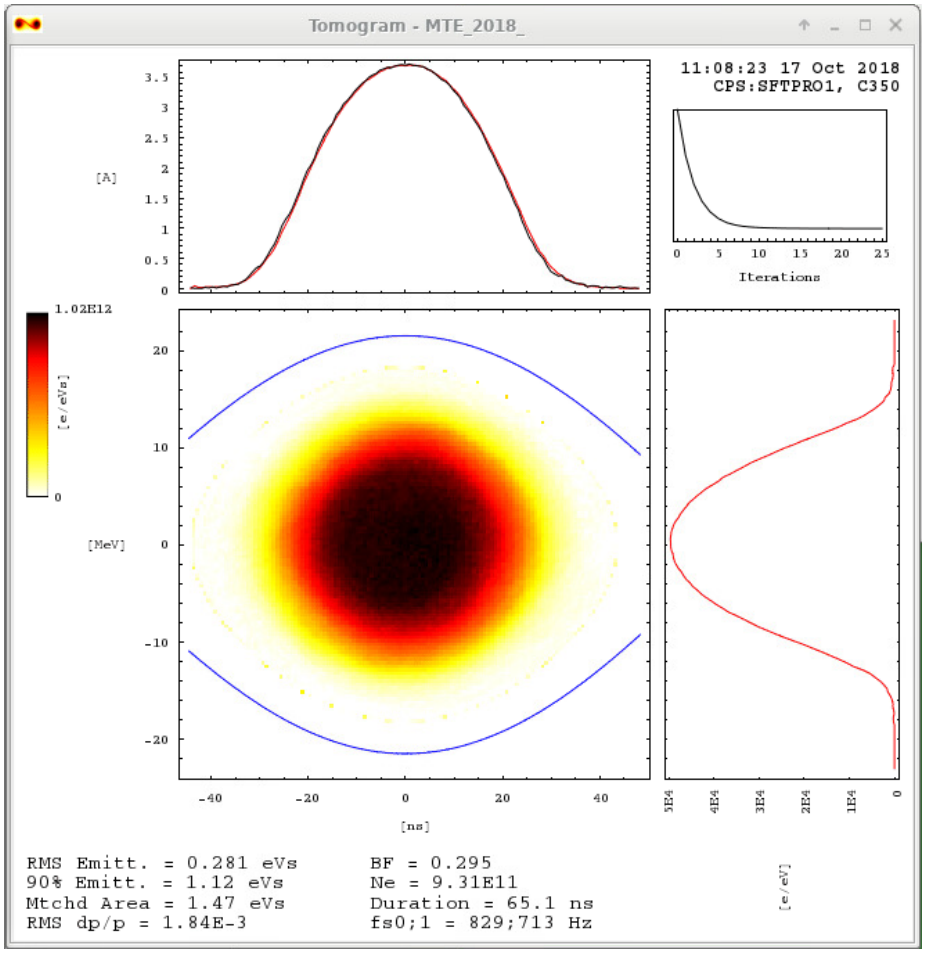

Figure 4.17: Tomographic reconstruction of the longitudinal phase space based on measured data. The reference profiles were available at the end of the intermediate flat top.

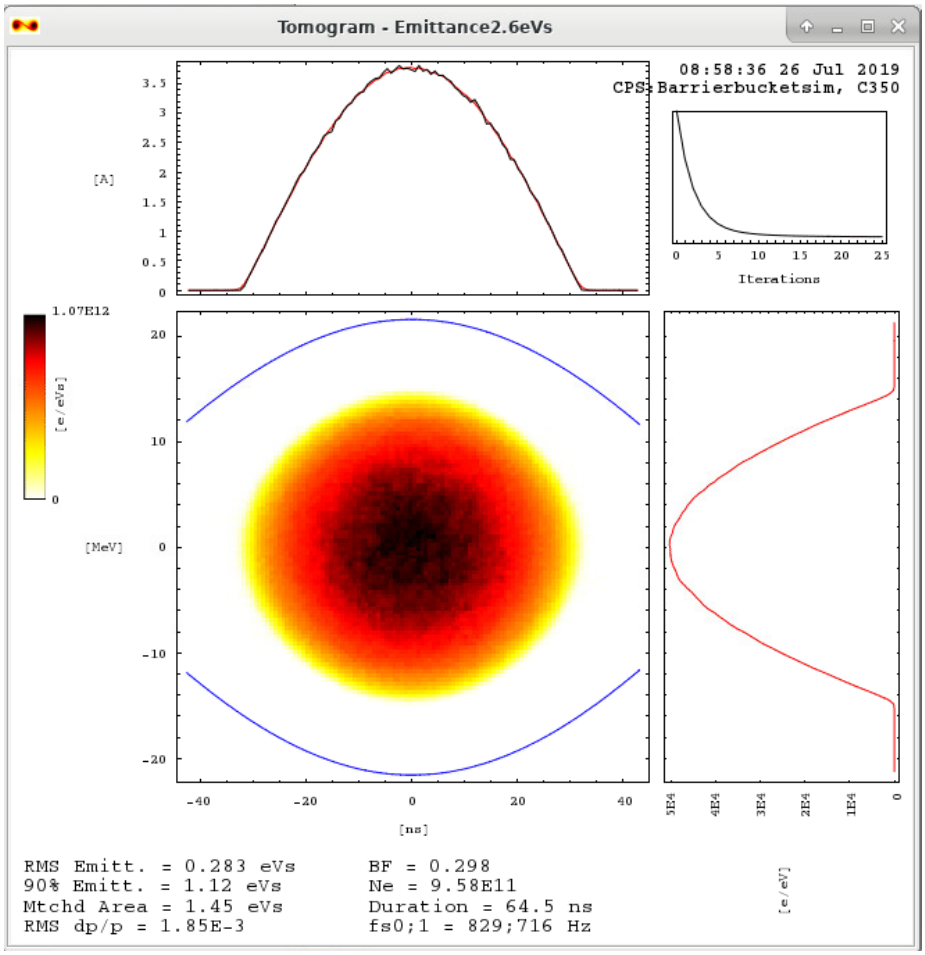

Figure 4.18: Tomographic reconstruction of the simulated longitudinal phase space matching the parameters of Fig. 4.17.

4.4.2.5 Results

Figure 4.19 shows the simulated evolution of the bunch profiles under conditions comparable to those of the measured evolution presented in Fig. 4.15. It is clear that the simulated and measured longitudinal line densities agree to a great degree. The simulations reveal the longitudinal phase space at extraction, see Fig. 4.20, which highlights the slow synchrotron motion in the barrier buckets at extraction. Only a fraction of the particles is reflected at the barriers.

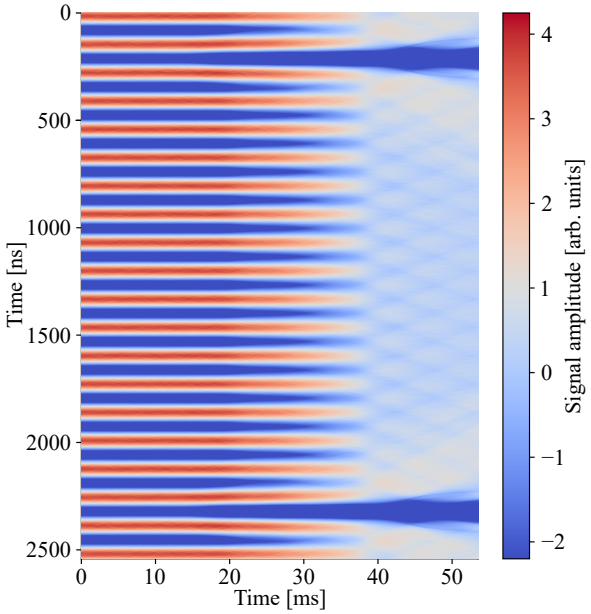

Figure 4.19: Simulated profile evolution for the same principal RF voltage evolution as for the measurements shown in Fig.4.15. The initial longitudinal emittance corresponds to the one measured during acceleration.

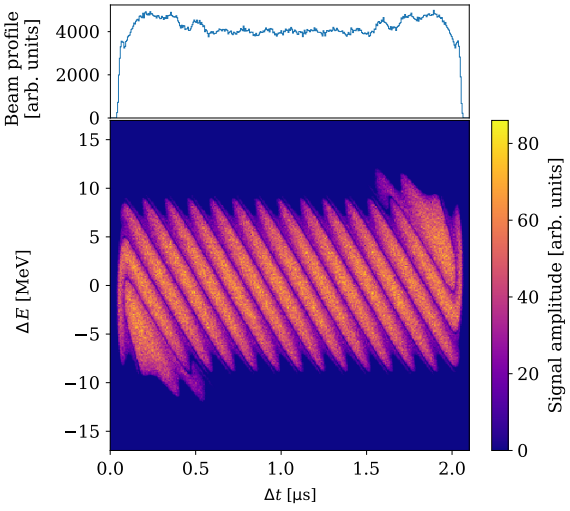

Figure 4.20: Simulated longitudinal phase space at extraction with the matched emittance corresponding to Fig. 4.15, 4.19 and without the 200 MHz modulation. The partial filamentation mechanism in the barrier bucket is illustrated. The projection of the beam distribution is also shown.

The limited time available for re-bucketing from the $h = 16$ buckets to the

barrier bucket, combined with the low synchrotron frequency, means that there is no time for the beam to filament into the barrier bucket. Since the duration of a reflection at the barrier is significantly shorter than the drift time in between the barriers, more particles are accumulated at the barriers near the reflection region. This results in the formation of shoulders on the bunch profile, i.e. regions with larger line density close to the barriers. This was also confirmed by simulations, which are in good agreement with the measured data [1].

4.4.2.6 Debunching on a longer time scale

The slow drift of particles between the barriers being the reason for the formation of shoulders near the gaps on a shorter time scale is also supported by measurements taken on a longer time scale. Here the longitudinal profile evolution corresponding to the drift of the particles can be observed. In order to gain time for these measurements, the nominal MTE cycle was modified not to include the transverse splitting. This made advancing the re-bucketing possible, see Fig. 4.21 (right). Simulations on a longer time scale were performed

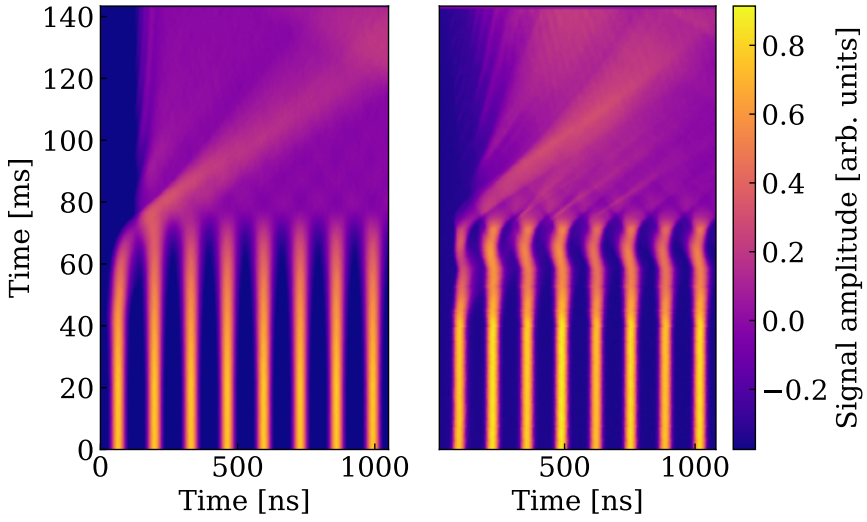

Figure 4.21: Beam reflecting off a potential barrier, shown over half a PS turn. The amplitude of the $h = 16$ system was lowered and then subsequently turned off at 70 ms and the amplitude of the barrier bucket RF system was increased to reach the maximum at the same time. The transverse beam splitting was disabled during these measurements. Simulated (left) and measured (right) profiles are shown.

to confirm the slow filamentation process compared to the time of the beam manipulation in barrier buckets at extraction. Figure 4.21 (left) shows the sim-

ulated longitudinal profile evolution on the same time scale as the measured data.

No more than 80 ms in total were available in the experimental cycle to observe a full filamentation in the barrier bucket. However, simulations on an even longer time scale were performed to confirm the slow speed of the filamentation in the barrier buckets made at extraction. Figure 4.22 (right) shows

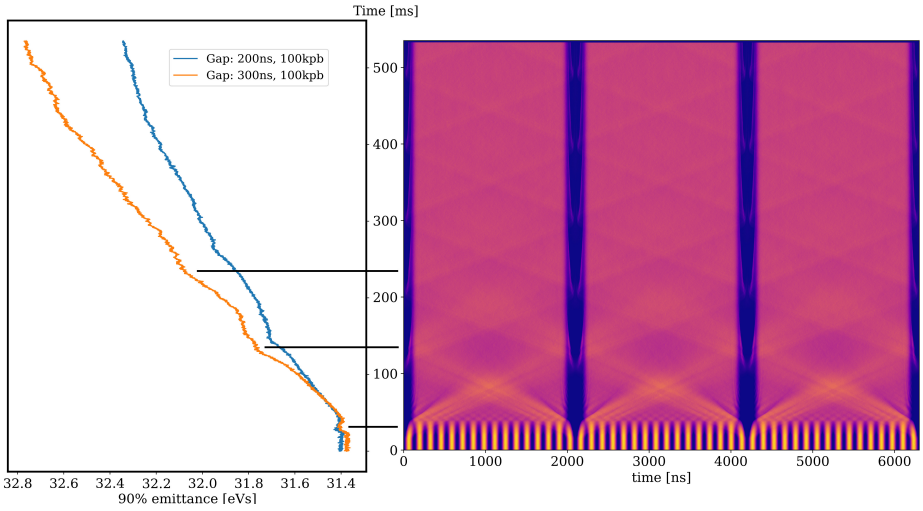

Figure 4.22: Oscillations in barrier buckets with a pulse duration of 300 ns. Beam profile evolution (right) and corresponding 90% area emittance (left). Peaks in 90% emittance correspond to shoulder forming in the barrier bucket.

three consecutive turns logged in one acquisition. This acquisition was repeated during the simulation and at the same time the corresponding 90% most dense area occupied by the particles (left figure) was calculated as a measure of the longitudinal emittance. The corresponding area in phase space occupied by the beam increases only slowly. This provides further evidence that during the time of the manipulation there is no significant macroscopic emittance growth, this only happens on a longer time scale. However, tests with beam are still required to confirm this result of the simulation at extraction energy given the unusual initial conditions of the re-bucketing process. The emittance in this case is measured with a numerical area calculation routine.

4.4.3 Beam in the PS and in the transfer line

As explained in Chapter 1, the extraction of the beam from the PS happens during five turns, each turn extracting a beamlet of the length of the accelerator circumference. The first four turns are extracting the islands of the distribution using kickers KFA31 and KFA21 with a correction from KFA9. The rise time of these kickers is 350 ns and their pulse is 10.5 μs long. The core is extracted with KFA4, KFA71 and KFA79, which have a much faster rise time of 56 ns, but can not sustain the pulse longer than one PS turn [138].

4.4.3.1 Longitudinal profiles in the transfer line

In order to investigate the beam removed by the kickers in the longitudinal structure and compare it with the gap made by the barrier, the longitudinal profiles recorded with the WCM, e.g. Fig. 4.15, and the WBP, e.g. Fig. 4.23, were compared.

During the joint beam tests in PS and SPS, the synchronisation of the position of the gap made by the barrier with the rise of the PS extraction and SPS injection kickers was not yet possible for technical reasons. A scheme for synchronising the phase of the barriers with the kicker rise times is proposed in Chapter 5. This means that the trigger of the PS extraction and SPS injection kickers, which are fixed with respect to each other in time, and the gap made by the barrier was fluctuating randomly from cycle to cycle. Examples of the measured longitudinal beam profiles in the transfer line for three different scenarios are shown in Fig. 4.23.

A typical longitudinal beam profile without barrier bucket is shown in the top plot. Two features are worth mentioning. Firstly, the increased line density fluctuations during the first four extracted turns and, secondly, a short longitudinal gap corresponding to the rise time of the kickers used to extract the first island and at the end of the profile, the central beamlet during the fifth turn. A profile corresponding to the barrier bucket position being asynchronous with the rise of the extraction kickers is visible in the middle plot. The gap region of the barrier bucket can be seen in the unfolded beam structure. In this case, five additional gaps are added for the longitudinal beam profile. Their position varies within the time corresponding to a single PS turn at the momentum of 14 GeV/c, i.e. 2.1 μs, as the transfer trigger jitters with respect to the gap position due to the lack of synchronisation. The bottom plot shows a case when the barrier bucket is approximately synchronous with the kicker rise times, which occurred only accidentally during these measurements.

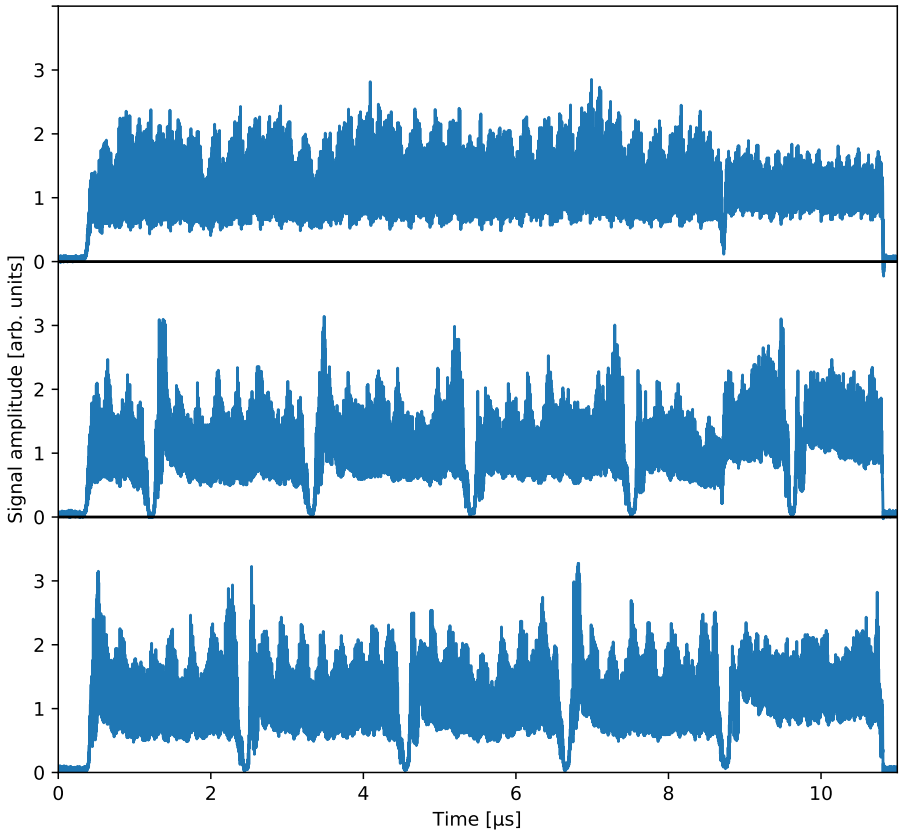

Figure 4.23: Examples of the longitudinal beam structure measured in the transfer line without barrier bucket (top), with barrier bucket asynchronous with the rise of the PS extraction kicker (middle) and with barrier bucket synchronous with the rise of the PS extraction kickers (bottom). The 200 MHz modulation is clearly visible in all cases.

4.4.3.2 Longitudinal profiles in the PS and in the transfer line

Comparing the line density measured in the TT2 transfer line and in the PS ring indicates parts of the beam lost due to kicker rise times. In the case of an ideal, loss-less extraction, it is expected that the longitudinal line density signal measured in the transfer line, during the five turns of extraction, is identical to the longitudinal line density profile before extraction. Clearly, the total longitudinal beam distribution is ideally the same before and after extraction. To demonstrate this, the following analysis using [189–194] and code developed for this study was performed.

As both instruments, the WBP and the WCM are operated at different sampling rates, have different bandwidths and their triggers were also different, the acquired profiles from the two instruments were pre-processed. The WCM

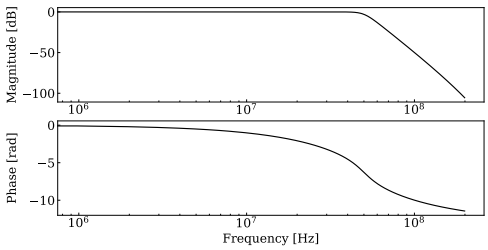

Figure 4.24: Single pass response of the low-pass filter. The forward-backward filtering technique squares the frequency response and cancels the phase response.

signal has high lower cut-off frequency, meaning that the comparison with the WBP is usable only when the barrier bucket is present. Furthermore, the WCM and the WBP have different amplitude scaling and DC offsets. Therefore, normalisation of the longitudinal line density and the current were also performed. Simply scaling by the minimums and maximums is more sensitive to outliers than the proposed method. A different normalisation was chosen based on the basic statistical properties of the signals. The steps of the analysis are detailed below.

The measured voltage from the WBP was downsampled using polyphase decomposition [195, pp. 179–184], [196] in combination with an anti-aliasing filter to match the sampling rate of the WCM without noticeable artefacts. Since the high frequency components of the signal are not responsible for the fluctuations in the longitudinal line density of the beam removed by the kickers, an additional low-pass filter was applied to remove, in particular, the 200 MHz component. The response of a single pass of the filter is shown in Fig. 4.24. The filter was applied forward-backward, which squares frequency response and cancels the phase response [197]. Since the signal to be filtered has potentially large swings at the beginning and at the ends of the intervals, the initial conditions for the filter were chosen using Gustaffson's method [198, 199]. As a result, filter artefacts related to the transient response of the filter around these regions are minimised.

The resampled WBP signal was then sliced up into five segments of equal lengths in time, corresponding to one PS turn each. The falling edge of the instantaneous beam current at the tail of the batch was chosen as a reference position for the slicing. The slices were then summed giving a sequence of samples corresponding to one PS turn.

It is assumed that the WCM, $\mathbf{x}$, and WBP, $\mathbf{y}$, signals are generated by largely the same beam, but measured by the two different devices. Hence the variance, the estimate of the normalised power of the signal [195, p. 816] in the overlapping bandwidth, is the same apart from a constant scaling factor. The

mean value, $\langle \mathbf{x} \rangle$ differs only by a constant offset. The following normalisation

$$\hat{\mathbf{x}}[n] = \frac{\mathbf{x}[n] - \langle \mathbf{x} \rangle}{\sqrt{\frac{1}{N}\sum_{i=1}^{N}(\mathbf{x}[i] - \langle \mathbf{x} \rangle)^2}} \tag{4.1}$$

cancels the DC offsets and the differences of the amplitude scaling at the same time for the signal of length N. To align $\hat{\mathbf{x}}$ and $\hat{\mathbf{y}}$ in time, the sample offset of the maximum of their cross-correlation sequence [200], [195, p. 815] was used. The non-overlapping parts were padded with zeros. The m-th term of the sequence is:

$$\hat{R}_{\mathbf{xy}}[m] = \frac{1}{N}\sum_{n=1}^{N} \hat{\mathbf{x}}[n+m]\hat{\mathbf{y}}[n] \ . \tag{4.2}$$

It follows from the property of the cross-correlation sequence [195, p. 818], that

$$|\hat{R}_{\mathbf{xy}}| \leq \hat{R}_{\mathbf{xx}}[0] = \hat{R}_{\mathbf{yy}}[0] = 1 \ , \tag{4.3}$$

where the normalisation was performed according to Eq. 4.1. Figure 4.25 illustrates the normalised cross correlation sequence for a pair of acquisitions.

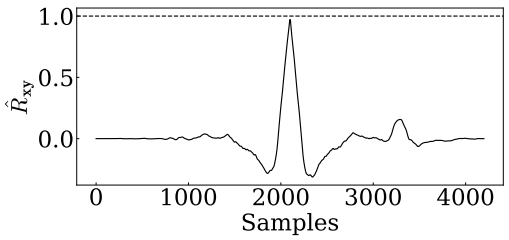

Figure 4.25: The cross-correlation sequence of the signals compared in Fig. 4.26, with the maximum at 0.97 for this example.

In the ideal case when the signals are identical, the maximum of their normalised cross-correlation sequence is equal to 1, which is the starting value of their normalised autocorrelation sequence. Otherwise, $\max\left\{\hat{R}_{\mathbf{xy}}\right\}$ falls in the $[-1, 1)$ interval, with a positive value signalling some degree of similarity.

Figure 4.26 shows an example comparison between $\hat{\mathbf{x}}$ and $\hat{\mathbf{y}}$. As expected, the match between the normalised WCM and the normalised and summed 5-turn signal of the WBP is nearly perfect.

There is a small, but relevant difference between these profiles during the first few tens of nanoseconds. This short longitudinal gap can be attributed to the rise time of the kickers required to extract the beam from the PS. The difference is systematically present in all the summed profiles when compared to the WCM acquisition before extraction. It only disappears when the barrier bucket position is synchronised with the kicker rise time as it coincides with the

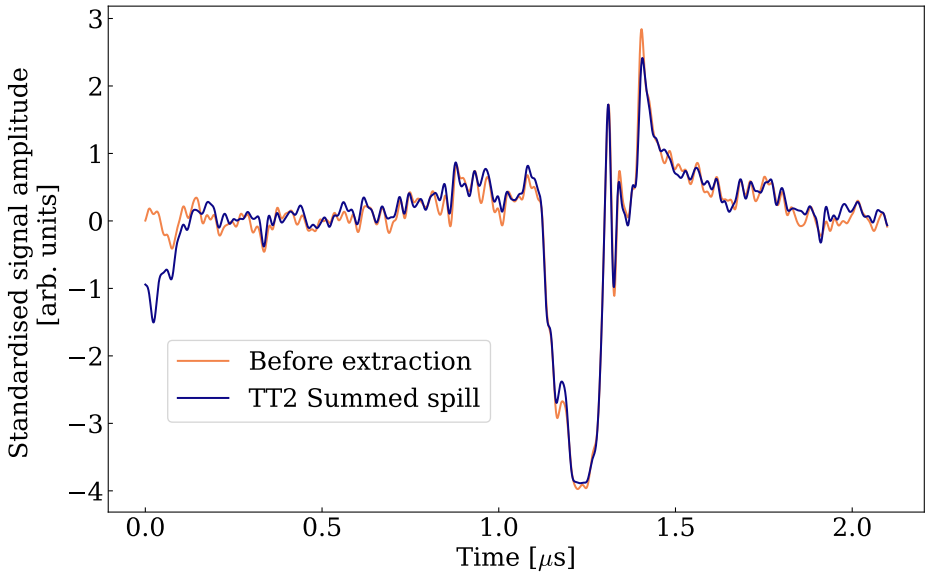

Figure 4.26: The summed profiles from the WBP in the TT2 transfer line compared with the WCM trace before extraction aligned according to the maximum of $R_{\mathbf{xy}}$.

gap position (Fig. 4.23, bottom). Hence, the deviation between the traces of Fig. 4.26 during the first few hundred nanoseconds demonstrates a difference in the line density attributed to the kickers.

Figure 4.27 summarises how well the sums of five-turn acquisitions correlate with the last-turn PS profile, taking into account in total 234 measurements from the PS with different gap size settings. The higher correlation scores for larger barrier bucket gap are due to the better signal-to-noise ratio. The lower, but still positive, correlations with small gap sizes are due to the higher relative noise in the profiles when the gaps made by the barrier bucket system are narrow. Although the high lower cut-off frequency of the WCM means that it can not measure DC levels of a coasting beam line density, an attempt of comparing the WCM and WBP signals without barriers was made. This is possible by detecting similarities outside the kicker gap regions in the longitudinal profiles, for example based on the residual $h = 16$ structure that both signals still contain. The downside is that the noise is higher once the profile comparison is restricted to these regions. Therefore, the result is a wide variation from a low, but still positive correlation to a relatively high correlation as illustrated by Fig. 4.27 with a zero gap setting.

It is clear from the systematic analysis that the beam structure before and after extraction when the barrier is present essentially only differs in a relatively small detail. This underlines that the beam loss mitigation can be adequately

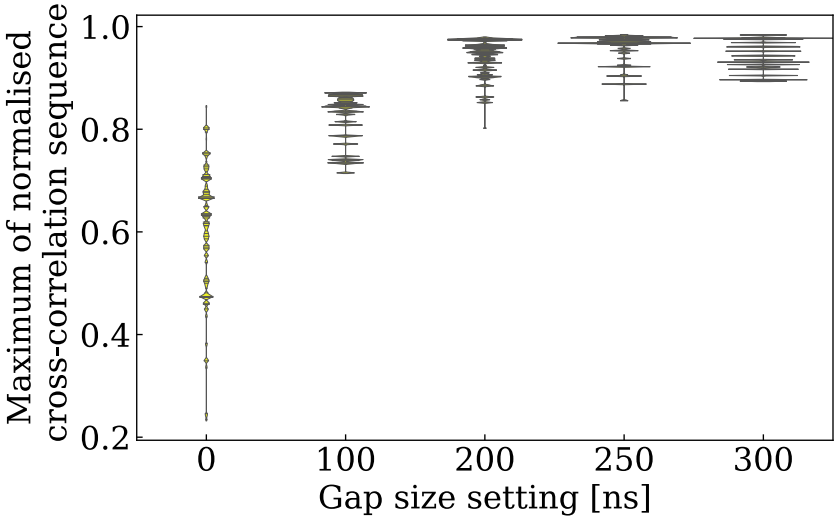

Figure 4.27: The maximums of the cross-correlation sequences of the last acquisitions before extraction from the PS and the summed five-turn profiles normalised to the same power. Each thin, horizontal line represents a pair of acquisitions. The length of the horizontal line shows the relative frequency of the values falling in the corresponding bin [194].

addressed by the barrier bucket system once it is synchronised with the extraction kickers. A sufficiently large gap can be made to leave time for the field of the kickers to rise.

4.4.4 Intensity dependent effects

The measured variation of the line density at the edge of the drift space decreases with increasing intensity. The difference of a profile calculated using local elliptic [201] beam distribution and a measured profile can be seen in Fig. 4.28. As

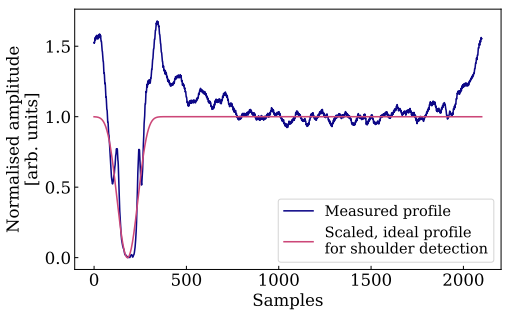

Figure 4.28: The measured and profiles calculated from local elliptical beam distribution scaled for shoulder height detection.

the intensity increases, the measured line density gets closer to the calculated.

In order to confirm this observation systematically, the acquisitions during the intensity scan were analysed.

The measured profiles were low-pass filtered to remove the 200 MHz component as described in Section 4.4.3 using the same filter, see Fig. 4.24. In order to establish the position of the gaps, calculated profiles were cross-correlated with the measured profiles.

A correction for the DC level based on the mean of the signal as in Section 4.4.3. It was not necessary to normalise for the power of the rest of the spectral components in this case, because the signal amplitude of the calculated and measured profiles were in the same range, hence the correlation produces accurate results. Figure 4.29 shows an example of the result.

Since one gap per PS turn was made, the criterion for successful gap detection was that the single, isolated maximums, see Fig. 4.29, of the cross-

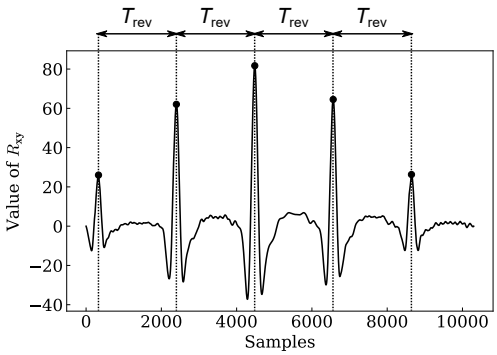

Figure 4.29: The cross-correlation sequence of the measured and calculated profiles with the detected peaks.

correlation sequence corresponding to the gaps are one revolution period apart with a ± 1% error corresponding to the uncertainty of the peak detection. The minimums of Fig. 4.29 represent the shoulders that are in anti-phase with the gaps. The reliability of the detection was improved by using a series of ideal profiles spanning three turns not just a single one. This value was established based on practical considerations of the calculation, representing a trade-off between accuracy and running time. The full cross correlation series spans almost 5 PS turns in time, because the original data was spanning almost two PS turns, containing two gaps, plus the calculated profiles were three turns long. Establishing the position of the gaps made it possible to align the profiles automatically.

Once the azimuthal position of the gaps were known, the height of the peaks of the longitudinal profiles near the gap region could be established by comparing the flat region of the profiles with the peaks around the gaps as illustrated by Fig. 4.28. Technically, the profiles were normalised such that the height of the line density between the gaps in the middle and the minimum of the line density is equal to one, see Fig. 4.28 for an example. This way, the middle point between the gaps, the mean of the centre of the profiles calculated for 200 ns, becomes

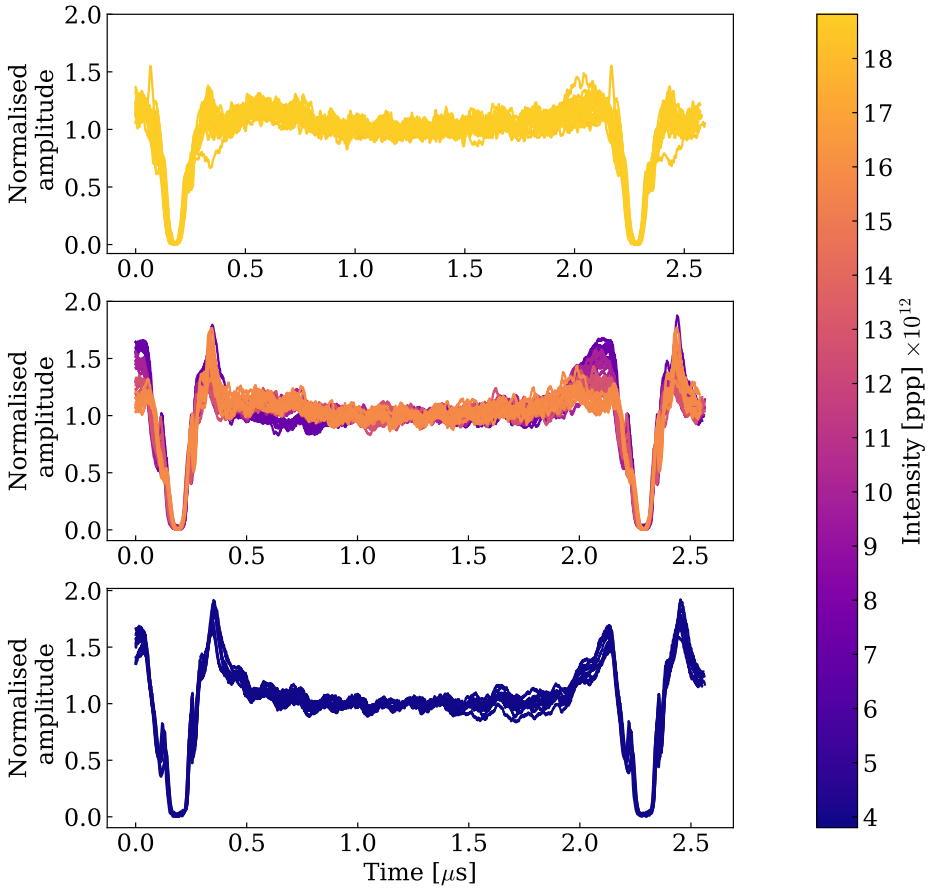

Figure 4.30: Comparison of the low-pass filtered, normalised longitudinal line density profiles at extraction at the same time in the re-bucketing process for acquisitions with 180 ns gap size setting. The effect of the beam intensity can be seen.

the reference for the height of the shoulders. This is a reasonable reference since, as already said in Section 4.4.2, the particles that reflect off the barriers, can not reach the middle of the barrier during the manipulation. Therefore by measuring the height of the excess peak, the deviation of the low-pass-filtered profiles from the calculated can be compared.

Figure 4.30 shows all the traces acquired by the WCM at extraction during different cycles for the case of 180 ns gap setting, ordered by beam intensity. The traces were sorted into three intensity categories based on the number of available measurements: the beam intensity is less than 6×10^{12} ppp in the bottom plot, greater or equal than 6×10^{12} ppp and less than 1.6×10^{13} ppp in the middle plot and greater or equal than 1.6×10^{13} ppp in the top plot. The colour of the traces is mapped to the intensity scale on the right of the figure.

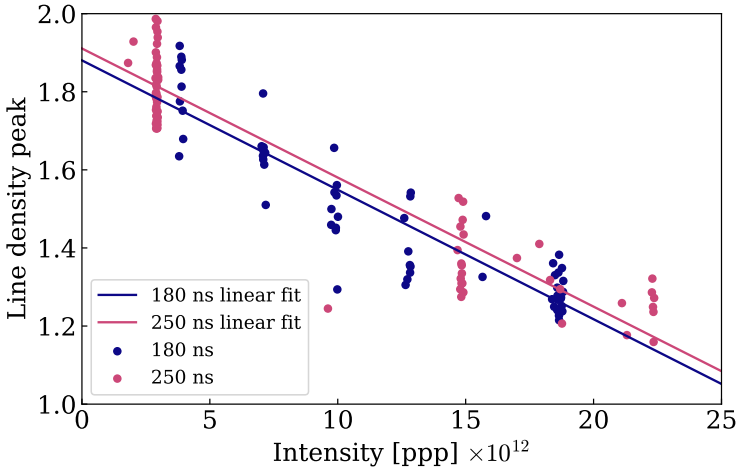

Figure 4.31: Normalised line density change along the bunch, showing a decreasing trend towards improved flatness of the bunch with increasing intensity. The colours refer to the different gap duration settings as indicated in the legend. Independent of the gap duration, the line density change improves with increasing intensity. 63 and 76 acquisitions for 180 ns and 250 ns are shown. The least-squares linear fits are displayed to highlight the downward trend.

Firstly, the observation is clear that longitudinal line density gets flatter as the intensity increases.

Secondly, the asymmetry around the generated gap increases as the intensity increases. Comparing the left-hand-side and right-hand-side of the gap regions of the middle and top plots shows greater asymmetry than the same features in the bottom plot. The observations seem to indicate that the asymmetry around the gap: a sharper peak on the right-hand-side of the gap compared to the left-hand-side is preserved as the intensity increases.

When extending the analysis to the longitudinal profiles corresponding to a 250 ns gap setting, too, the observations indicate that as the intensity increases the profiles become flatter irrespective of the size of the gap. Figure 4.31 shows the peak value of the line density profiles around the gap with respect to the reference in the middle of the profiles. The normalisation described earlier in this section means that the middle of the profiles correspond to the value 1, meaning that an ideal profile without an increase in the line density around the gap would have a line density peak of 1. Larger than 1 values indicate that the line density around the gap is higher than the ideal, filamented profile's line density. The clear downward trend shows that the line density profiles near extraction get flatter as the intensity increases.

4.4.4.1 200 MHz modulation and flatness

The analysis was performed with several low pass filter settings with a cut-off set at 20 MHz–500 MHz to establish the robustness of the cross-correlation technique. When a low pass filter is used, the results are very similar to the one reported in the previous section largely independent of the cut-off frequency of the low pass filter.

Although the results without filter also support the same trend as the filtered profiles, an additional effect of the short, 200 MHz modulation can be seen in this case. Figure 4.32 shows that the trend is still visible with the high frequency

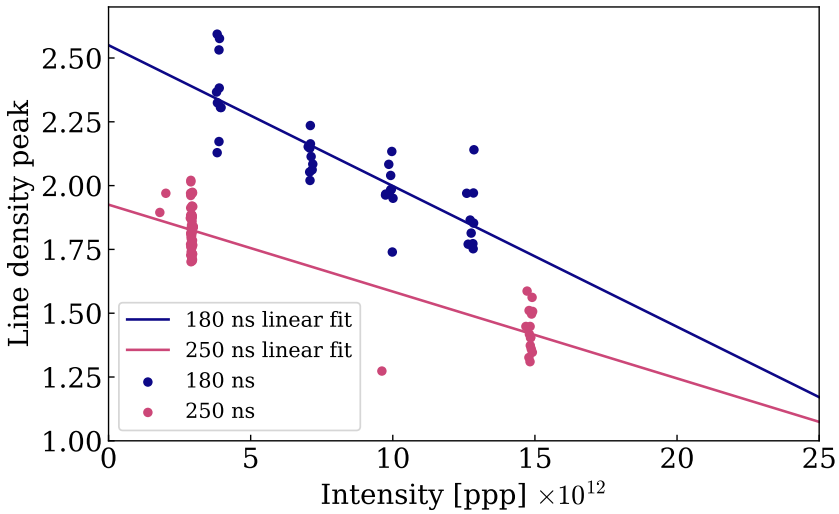

Figure 4.32: The results of the analysis without low-pass filtering. The detection routine is less efficient at the highest intensities in this case and there is an overall increase in the line density peak when the 200 MHz system is active with the 180 ns gap setting.

noise not filtered. However, a difference in the overall offset is clearly visible. This is because almost all of the 180 ns profiles were acquired with the 200 MHz system activated. Unfortunately, the detection was not successful for more of the high intensity profiles with 180 ns due to high noise content without the application of a low-pass filter.

As mentioned before, the reference level, corresponding to the line density peak value 1 in Fig. 4.32, is taken in the opposite azimuthal position compared to the position of the gap as an average calculated for 200 ns of the longitudinal profile. Therefore the reason for the offset in the trend of the 180 ns, 200 MHz modulated profiles is that the averaging provides the same reference value as in

the previous analysis, but the line density peak is calculated as the maximum of the line density in the detected gap region without smoothing.

Therefore, as it is clear from Fig. 4.32, the 200 MHz modulation adds an overall offset and changes slope of the trendline with the 180 ns setting compared to its low-pass filtered counterpart in Fig. 4.31. However, the limited amount of data available seems to indicate that the 200 MHz modulation does not change the overall trend of improving flatness with increasing intensity, which is expected because of the short duration of the manipulation.

4.4.4.2 Effects of cavity impedances

In order to investigate intensity effects, particle tracking simulations including cavity longitudinal impedance models [202] were performed. Table 4.3 lists of all the RF cavities and their gap status after the re-bucketing has taken place.

Cavity	Number installed	Gap status after re-bucketing
Finemet®	1	Open
10 MHz	11	Closed
20 MHz	2	Closed
40 MHz	2	Open
80 MHz	4	Open
200 MHz	6	Open during last 1 ms, only.

Table 4.3: RF cavities installed in the PS ring and the status of their gaps after the re-bucketing into the barrier bucket took place.

The beam spectrum overlaps with the Finemet® cavity band, therefore the most beam loading is expected in the frequency range of this cavity. This expectation is confirmed with simulations. The parameters used were the same as detailed at the beginning of Section 4.4. The longitudinal impedance of the cavities with their gaps open were included in the simulations. Figure 4.4.4.2 shows the simulated effective RF waveforms changing with beam intensity. The distortion of the profiles near the peak of the pulses is visible as the intensity increases.

In order to evaluate the relative contributions of the different cavities, the total voltage for different configurations of cavities was calculated: V_{ALL} represents all open gap cavities; V_{FC} denotes the total voltage with only the Finemet® cavity included; V_{PROG} is the ideal, programmed voltage without any intensity effects. Then simulations with these configurations were performed using BLonD. The difference $V_{\mathrm{ALL}} - V_{\mathrm{FC}}$ represents the additional voltage contribution originating in the 40 MHz and 80 MHz cavities. The difference $V_{\mathrm{ALL}} - V_{\mathrm{PROG}}$ is the induced voltage contribution of all the cavities, including the Finemet® cavity. Figure 4.4.4.2 compares these voltage differences. As expected, there is

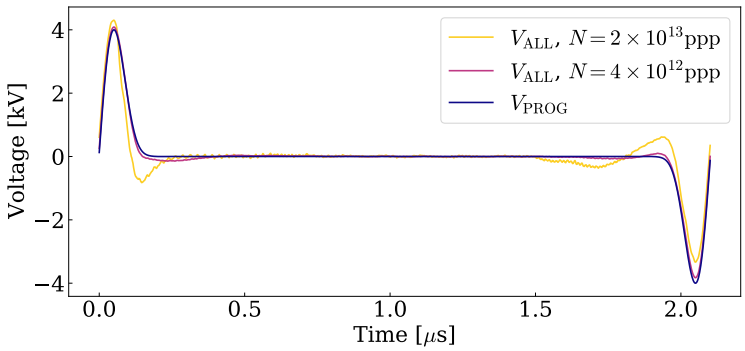

Figure 4.33: Simulated voltage seen by the beam at extraction at different beam intensities with reference. The impedance of the Finemet®, 40 MHz and 80 MHz cavities with higher order modes was taken into account.

an order of magnitude difference between the induced voltage contribution of the high frequency cavities and the Finemet® cavity to the favour of the latter.

The simulated longitudinal line density was also compared at different beam intensities in order to provide an explanation to the observations with beam. The change of the line density profiles can be seen in Fig. 4.35 as intensity of the beam increases. The middle of the profiles corresponding to the drift space in the barrier bucket are largely unaffected by the intensity. However, the line density peaks in the gap region become uneven as the beam intensity increases. There are larger and narrower peaks on one side and wider shoulders on the other side of the gap. This phenomenon was only observed in simulations when the Finemet® cavity was included, therefore it is attributed to the beam loading in this cavity. A similar behaviour near the gap can be seen in Fig 4.30 in the measured profiles. The increase of the line density corresponding to a longitudinal blow-up in the drift space, based on these simulations, is not caused by the beam coupling to the cavities that have open gaps during the manipulation. Identifying the source of the increase of the line density, in particular in the drift region requires further investigations.

4.4.5 Beam loss reduction

This section evaluates the success of the main practical aim of this study, the beam loss reduction at the PS-SPS transfer by barrier buckets. As described in Section 4.2.3, the PS is equipped with two BLM systems, both of which were collecting data during these studies. Careful alignment of the data acquired

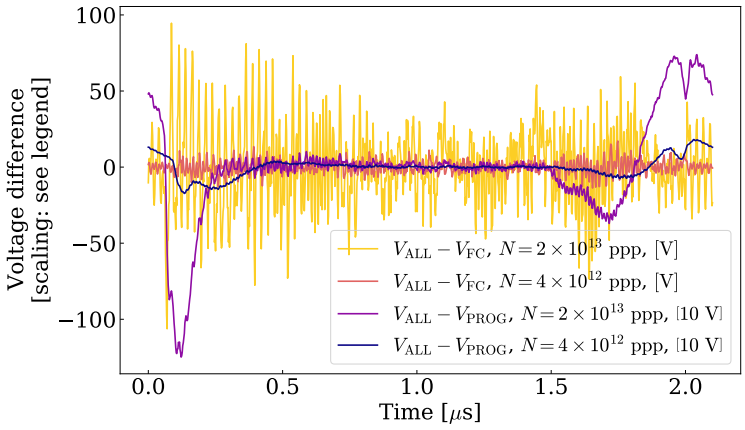

Figure 4.34: The relative contributions to beam loading at the lowest and highest beam intensities of the different cavities. The voltage induced in the Finemet® cavity is an order of magnitude more than voltage induced in the 40 MHz and 80 MHz cavities.

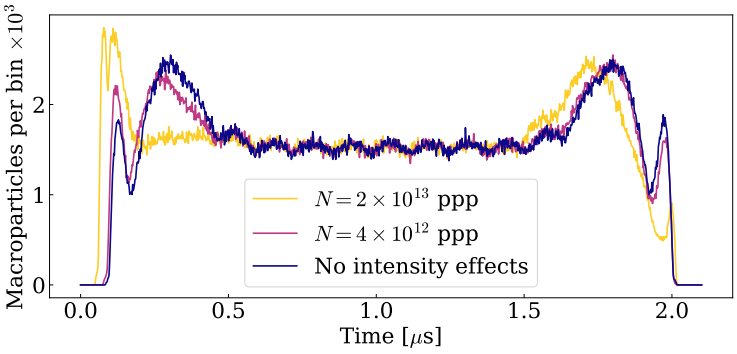

Figure 4.35: Simulated effect of beam loading in the Finemet® cavity on the profiles at extraction with different beam intensities and without intensity effects at a 180 ns gap setting.

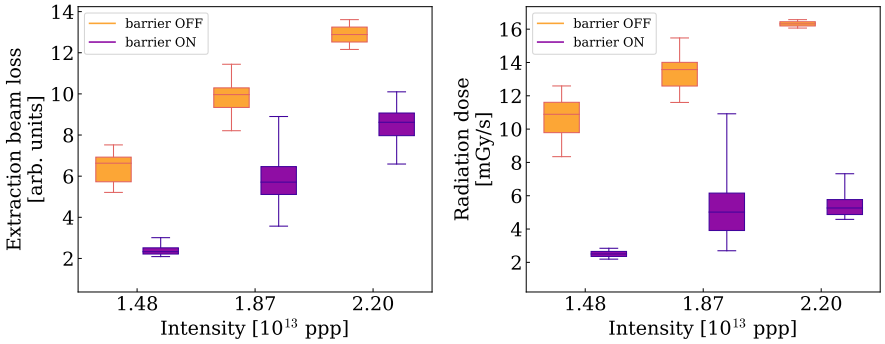

Figure 4.36: The measurements with the old (left) and new (right) BLM systems show the effectiveness of the barrier bucket system in reducing the losses across all intensities, which is obvious by comparing the orange box and whiskers indicating much higher losses with the barrier off to the purple ones indicating much lower losses when the barrier bucket system was operational.

by the BLM and WCM systems made the comparison of beam losses with and without the barrier buckets possible. The results of the subsequent analysis are presented below.

4.4.5.1 Reduction of losses

The following section assesses the magnitude of the beam loss reduction provided by the new scheme. The integrated radiation dose along the cycle reported by all the new BLMs were summed and compared when the barrier bucket system was operational and when switched off. The losses at the moment of extraction as provided by the old BLM system were also summed for all detectors and compared with respect to the new RF system being active or not. The two different BLM systems provide conclusive evidence on the effectiveness of the beam loss reduction provided by the new barrier bucket RF. All cases with the barrier on, irrespective of the size of the gap, were lumped together in Fig. 4.36. Both the left and right plots in Fig. 4.36 indicate a beam loss reduction across all gap sizes and intensities when the barrier bucket system is operational. The barrier bucket scheme effectively reduces losses at extraction.

The difference in the spread of the measurements across the two plots of Fig. 4.36 with the barrier bucket system operational is the result of varying beam loss reduction with different sized gaps. Shorter gaps were also tried with 1.87×10^{13} ppp beam intensity, but not with other intensities, hence the whiskers are consistently longer in these cases representing a larger spread of beam loss corresponding to a larger range of gap settings. This is presented in detail in the next subsection. The small spread with the highest, 2.20×10^{13} ppp

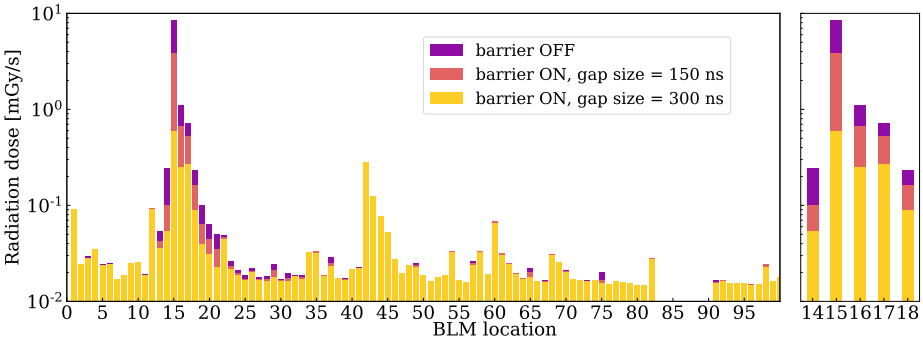

Figure 4.37: An example logarithmic plot of the losses as the function of the location in the PS ring with different gap sizes. Left: the total beam loss as a function of location along the PS ring. Right: zoom of the BLM readings in the extraction region. Plot shows the same data as [1] Fig. 9 using different colours and aspect ratios. The intensity corresponding to these measurements is 1870×10^{10} ppp.

intensity of the control measurement, when the barrier is off, is because of the low number of data points available. Furthermore, measurement data was not available for the new system from straight sections 83-90 for technical reasons. This is also seen in Fig. 4.37. The losses in this section add to the extraction loss shown in the left figure, but are missing from the radiation dose reported by the right figure. Nevertheless, these details do not alter the overall conclusion, that the new barrier bucket system is highly effective in reducing the losses in the fixed target cycle.

4.4.5.2 Dependence of the losses on the gap size

The distribution of the integrated radiation dose during the cycle along the whole PS circumference is illustrated with three examples in Fig. 4.37 (left) together with a zoom (right) of the extraction region. The measurement data shown as a logarithmic plot by Fig. 4.37 was acquired by the new BLM system. The more than an order of magnitude loss reduction is visible in straight section 15 with a 300 ns long gap. Even a shorter gap reduces the losses significantly throughout the extraction region. The more particles are displaced by the wider barrier in the septum region, the lower the losses, as expected. In practice, wider than 300 ns gaps are becoming difficult to reach with the required quality with the hardware as mentioned in Chapter 3 due to bandwidth limitations. Making a much wider gap would not serve a practical purpose, either, since even the slowest kickers involved in MTE have a 360 ns rise time as explained in Section 4.4.3.

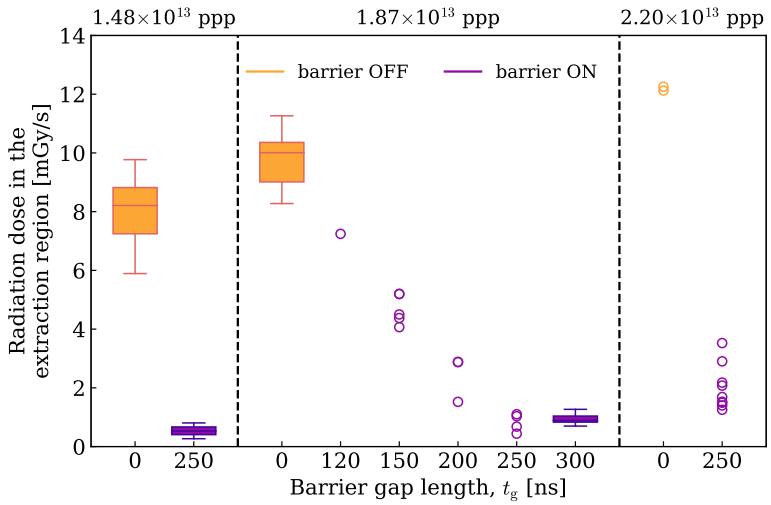

Figure 4.38: Integrated beam loss in the extraction region with three intensities, indicated on the top of the plot. The losses decrease as the gap size increases. Figure re-plotted from [1] Fig. 10 using different colours.

Barriers with various gap sizes were generated at different beam intensities as part of the studies. Figure 4.38 summarises the low, medium and high intensity measurements with varying gap sizes in the left, middle and right plots, respectively. In all three cases the losses in the extraction region decrease with increasing gap size as the barrier bucket covers a bigger fraction of the kicker rise times. This demonstrates that the barrier bucket system is capable of significant beam loss reduction when extracting fixed target beams from the PS using MTE.

4.5 Summary

Following the essential commissioning of the basic features of the new firmware developed to generate barrier buckets with beam, barrier buckets with flat line densities were produced from matched initial conditions. Progressing with more complex tests, barriers moving in azimuth confirmed the theoretically predicted behaviour of the beam in decompressed and compressed buckets.

The conditions for the re-bucketing at flat top from $h = 16$ conventional buckets to a barrier bucket were studied with beam and analysed using particle tracking simulations. These studies highlight that during the time available in the cycle only partial filamentation in the barrier bucket can take place. For this reason, to achieve a quasi-symmetrical longitudinal distribution at extraction from the PS, the gaps generated by the barriers have to be aligned with the gaps already existing before debunching between the conventional $h = 16$ RF buckets.

Application of the cross-correlation sequence of the longitudinal profiles acquired in the transfer line and the ones acquired in the PS also confirms that the 5-turn-length profiles, when added together, after the multi-turn extraction and the one-turn-length profiles before extraction are very similar. This was expected, but never explicitly shown before. However, a relevant and systematic difference in the line density of these profiles also confirm that the losses occurring at extraction are consistent with the extraction kicker rise times.

Using an adaptive barrier detection algorithm based on the cross-correlation of calculated and measured profiles show that as the intensity increases the flatness of the profiles also increases. A measure of the flatness was also developed. Comparing the profiles with varying intensity lead to the conclusion that the improvement of the longitudinal line density at larger beam intensities is likely to be independent of the size of the gap. The measured longitudinal line density profiles show an asymmetry around the gap region with increasing intensity. BLonD particle tracking simulations performed with the longitudinal impedance models of the Finemet®, 40 MHz and 80 MHz cavities identify beam loading from the Finemet® cavity as a likely source for the asymmetry of the profiles. The reason behind the flatness of the profiles at high intensity is subject of further studies.

Analysis of the carefully merged datasets acquired by the BLM and WCM systems allowed to assess the beam loss reduction attributed to the new barrier bucket system. Data from the old and new BLM systems was analysed focusing on the total integrated loss along the whole ring and in the extraction region. The clear conclusion can be drawn that the barrier bucket system reduces the beam loss up to an order of magnitude in the extraction region. Scans with

different sized gaps demonstrate that the longer the gap, the lower the losses. When the system was operated with a gap setting of 300 ns, a practically loss-free extraction from the PS was achieved.

In order to benefit from this scheme, a synchronisation between the SPS injection and the PS extraction processes has to be taken place. The next Chapter presents a proposal for this.

Chapter 5

A concept of synchronisation for barrier buckets

As explained in detail in the previous chapter, in order to benefit from the beam loss reduction in both the PS and SPS, the gaps in the beam covering the rise times of the PS extraction and SPS injection kickers have to be synchronised. This chapter outlines a conceptual synchronisation scenario and presents a proposed sequence.

The manipulation requires to move the bunches in azimuth in the PS with respect to the beam already circulating in the SPS, which is investigated using analytical calculations and particle tracking simulations.

5.1 Introduction

The SPS is presently able to receive the fixed target beam without barrier buckets from the PS, therefore the fundamental criteria for synchronisation [143, 203], such as the energy matching of the beam at transfer and the aperture requirements are met. However, since essentially a coasting beam is transferred with a modest 200 MHz modulation, the means of a conventional RF synchronisation are not necessary and therefore not available for this cycle. This presents a challenge for beam in barrier buckets as opposed to a coasting beam, because the gap needs to be generated synchronously with respect to the SPS reference position as detailed below.

As introduced in Chapter 1, the fixed target beam in the PS is extracted in 5 turns, hence one extraction fills 5/11 of the circumference of the SPS. There-

fore two PS cycles are needed in order to fill 10/11 of the SPS circumference. The remaining 1/11 of the SPS circumference remains empty in order to avoid losses at extraction due to the rise time of the kickers of the SPS.

The two transfers from the PS to the SPS, including the trigger for the extraction and SPS injection systems are presently controlled entirely from the SPS. This is possible since the coasting beam structure allows to extract at any azimuthal position. However, the presence of the gap means that this can not be the case. The synchronisation process must be able to trigger the generation of the barrier bucket in the PS such, that once the beam arrives in the SPS, the gap initiated in the PS overlaps with the gap needed by the SPS. Figure 5.1 presents a diagram of the chain of the fixed phase relationships between the systems involved in the synchronisation process to ultimately align the beams in both accelerators.

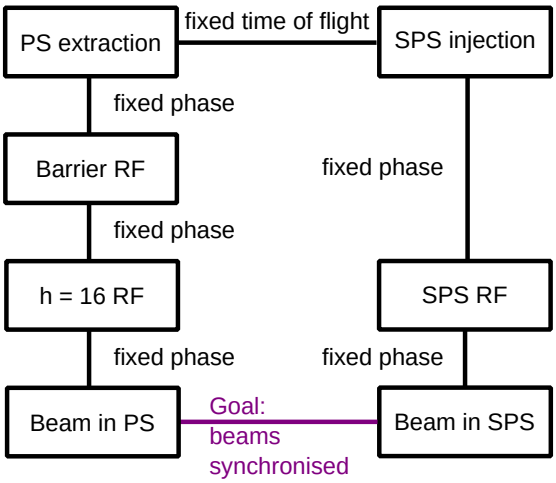

Figure 5.1: Chain of phase relationships between the systems of the PS and SPS involved in the extraction and injection. The fixed phase relationships mean that the position of the beam has to be aligned in the PS.

Moving the azimuth to achieve the fixed phase relationship means that the synchronisation requires to slightly accelerate and decelerate the beam in the PS. Such an azimuthal beam alignment is also referred to as cogging [204–212] or re-phasing [213]. This operation can be used for example as injection phase synchronisation, see for instance [214] and references therein, or for a collision point alignment [215–220]. In all cases the success of the synchronisation depends on whether the beam can follow the desired energy change associated with the cogging.

There are four main constraints in the PS to change the mean energy of the particles of the beam. All of these stem from the fact that only a few tens of milliseconds are available for the synchronisation.

Firstly, the main 10 MHz RF system can not be set to a sufficiently high voltage at flat-top once the transverse splitting is initiated, because the MTE requires a low momentum spread, which can only be provided by a low RF

voltage. Therefore to accelerate or decelerate the beam within the short time frame is not possible with this system. Hence a strategy such as the one applied for a conventional bunch to bucket transfer [214], is not directly applicable, only as a part of the synchronisation.

Secondly, the synchrotron frequency is too low in barrier buckets to move the beam azimuthally without significant perturbation of the longitudinal line density as shown in Section 4.4. In addition, the barrier bucket RF system does not have sufficient voltage to change the mean energy of the beam sufficiently fast for the synchronisation.

Thirdly, the experimental studies and simulations of the re-bucketing in the previous chapter have shown that the barrier bucket, and consequently the gap in the longitudinal line density, can not be made at an arbitrary azimuthal position as discussed in detail in Section 4.4.2. In fact, the gap has to be located between two conventional $h = 16$ buckets.

Fourthly, the radial displacement has to be kept small during the manipulation, because of the aperture limitation of the PS.

Introducing a short, few tens of milliseconds long flat-top, just before the $h = 16$ RF voltage is decreased for the transverse splitting, could in principle meet these requirements.

The initial idea is to profit from the already existing $h = 16$ structure of the beam to accommodate the gap to be made by the barrier bucket, as there are gaps between the bunches already. Then the barrier bucket azimuth is locked to one of these gaps, closest to the known extraction position. Moving the bunches and the gaps between the $h = 16$ bunches using the main RF system can be a viable strategy, when its voltage is sufficient before the transverse splitting is initiated. The position, where the gap should be is determined by the time of the extraction, which is known well before the operation takes place from the SPS. The advantage of such a manipulation is that it would only require a 1/16 azimuthal movement at maximum, conservatively assuming a one directional azimuthal motion.

5.2 Requirements and constraints

As explained in the introduction, it is sufficient to move the beam by only one $h = 16$ bucket and generate the barrier with respect to the nearest possible gap position, assuming one directional movement only. Such an operation could be achieved by using the main RF system before its voltage is lowered for transverse splitting.

The radial displacement should additionally be small to respect the aperture

limitation. On the other hand, the precision of the synchronisation can be relaxed to the few ns compared to a conventional case, when this alignment must be even an order of magnitude better to transfer a bunch into a very short 200 MHz bucket in the SPS. The gap needs to only occur during the kicker rise time, which is a few hundred ns long, therefore the centre position of the gap can vary a few nanoseconds without the loss of the effectiveness of the beam loss reduction scheme. The requirements are summarised in Table 5.1.

Beam momentum	14 GeV/c
Precision	< 5 ns
Manipulation time	tens of milliseconds
Max. phase change	$2\pi/16$ corresponding to 1 bucket at $h = 16$
Max. radial excursion	$<$ few mm

Table 5.1: Requirements for the synchronisation.

The main steps of a synchronisation sequence requiring only a 1/16 azimuthal displacement are shown in Table 5.2.

No.	Manipulation
1	Set PS revolution frequency is synchronous with the on of the SPS at an exact ratio of 1/11.
2	Move the beam to the nearest h=16 gap synchronous with the extraction azimuth.
3	Create barrier at the right position for re-bucketing and extraction.
4	Trigger ejection system based on SPS signals.

Table 5.2: Overview of the proposed synchronisation steps when including a short flat-top in the cycle after acceleration and before the transverse splitting.

After aligning the frequency reference of the PS to the SPS, the beam needs to be accelerated and decelerated to move its azimuth. This is achieved by changing the RF frequency at a constant magnetic field. The required duration for such a manipulation is calculated in the following.

5.2.1 Minimum duration of the phase slip

Since one of the limitations is the radial displacement, the frequency requirement is calculated from this, despite the fact that the radial position in practice defined by the frequency. If the beam is displaced by ΔR at a constant magnetic field [213], the required frequency change can be calculated according to [221, p. 9] as:

$$\frac{df}{f} = \frac{\gamma^2}{\gamma_{\mathrm{tr}}^2 - \gamma^2} \frac{dR}{R} \ . \tag{5.1}$$

The minimum time required for the beam to be on the modified orbit can be calculated from the frequency offset. Fig. 5.2 compares the time needed for a half azimuthal change corresponding to a $h = 1$ phase slip in the optimistic two directional case, with the time needed for the $h = 16$ and $h = 32$ movements, the order of magnitude time difference is evident. Accepting a radial displacement of maximum a few millimetres, the minimum time for the frequency bump is in the order of tens of milliseconds.

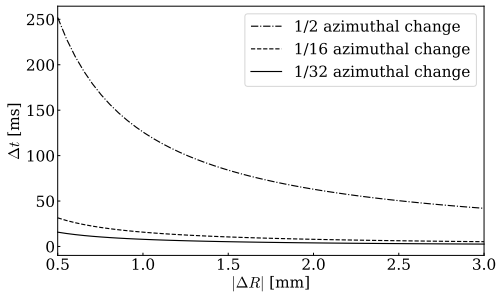

Figure 5.2: The minimum time needed for the beam to spend on off-orbit versus the radial displacement.

5.2.2 Smooth phase bump

In order to avoid discontinuities in the phase or frequency program leading to an unnecessary oscillation of the $h = 16$ bunch, a smooth, analytical pulse based on a sine curve was introduced as the following:

$$\phi(\phi_{\text{set}}, T, t) = \frac{\phi_{\text{set}}}{T}\left[t - \frac{T}{2\pi}\sin\left(\frac{2\pi}{T}t\right)\right] \tag{5.2}$$

$$t \in [0, T] \quad ; \quad \phi_{\text{set}} \in [-2\pi, 2\pi] \ . \tag{5.3}$$

The required phase slip of the gap between the bunches is ϕ_{set}, measured in RF phase of the $h = 16$ buckets. The duration of the phase bump is set by T and t is the running variable for time. Fig. 5.3 illustrates the phase excursion in the worst case, the corresponding relative RF frequency change and the radial position change.

The advantage is that the phase has zero slopes at the beginning and at the end of the curves. Because of the sinusoidal shape, all its derivatives will be cosine and sine. Therefore the stable phase will also change as a sinusoid. This curve may be optimised in the future, but as a feasibility test it is sufficiently smooth as the following calculations demonstrate.

In order to calculate the synchronous phase change during the manipulation,

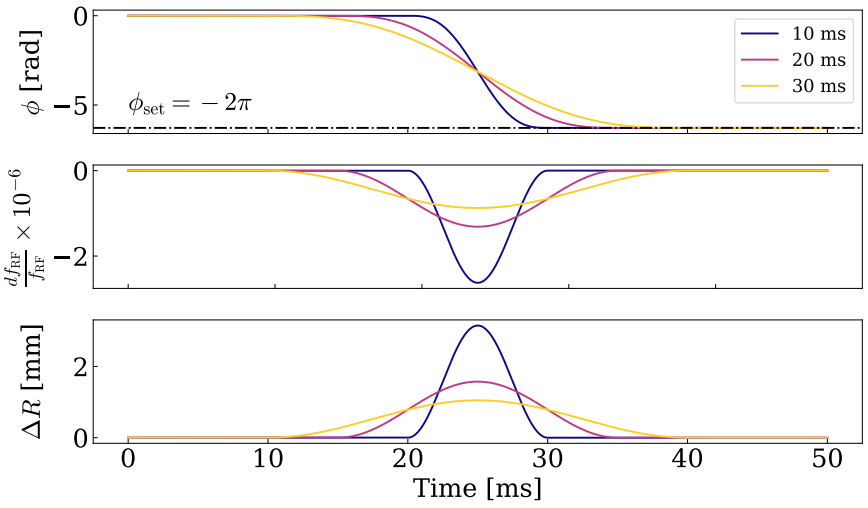

Figure 5.3: The following parameters are shown during a 10, 20 and 30 ms long manipulation: the pre-defined phase program (top), the relative change of the RF frequency (middle) and the change of the radial position (bottom).

the frequency and momentum differential relation is used [221, p. 9]:

$$\frac{dp}{p} = \frac{\gamma_{\mathrm{tr}}^2 \gamma^2}{\gamma_{\mathrm{tr}}^2 - \gamma^2} \frac{df}{f} \ . \tag{5.4}$$

The relation above is combined with Eqs. 2.5 and 5.1 to obtain:

$$\sin \phi_{\mathrm{s}} \ = \ \frac{df}{dt} \frac{p}{f} \frac{\gamma_{\mathrm{tr}}^2 \gamma^2}{\gamma_{\mathrm{tr}}^2 - \gamma^2} \frac{2\pi R}{qV} \ = \ \frac{dR}{dt} p \frac{2\pi \gamma_{\mathrm{tr}}^2}{qV} \ . \tag{5.5}$$

The estimates of the most relevant parameters during the manipulation, the synchronous phase, the momentum change and the synchrotron frequency according to Eq. 2.12 are shown in Fig. 5.4.

The bucket filling factor is in the order of 20%. The bucket area shrinks in the case of the shortest, 10 ms manipulation by approximately 20% as illustrated by Fig. 5.4 bottom. Therefore the beam will still only occupy approximately a quarter of the accelerating and decelerating buckets meeting this requirement. However, a 10 ms short duration causes oscillations of the bunch as shown by simulations, therefore this is already a limiting case of the operation. The actual change of the bucket area is expected to be well below one fifth. The small stable phase change with a small radial change compared to the aperture are promising parameters showing that the beam could possibly follow a change in the order of 30 ms during a short flat top.

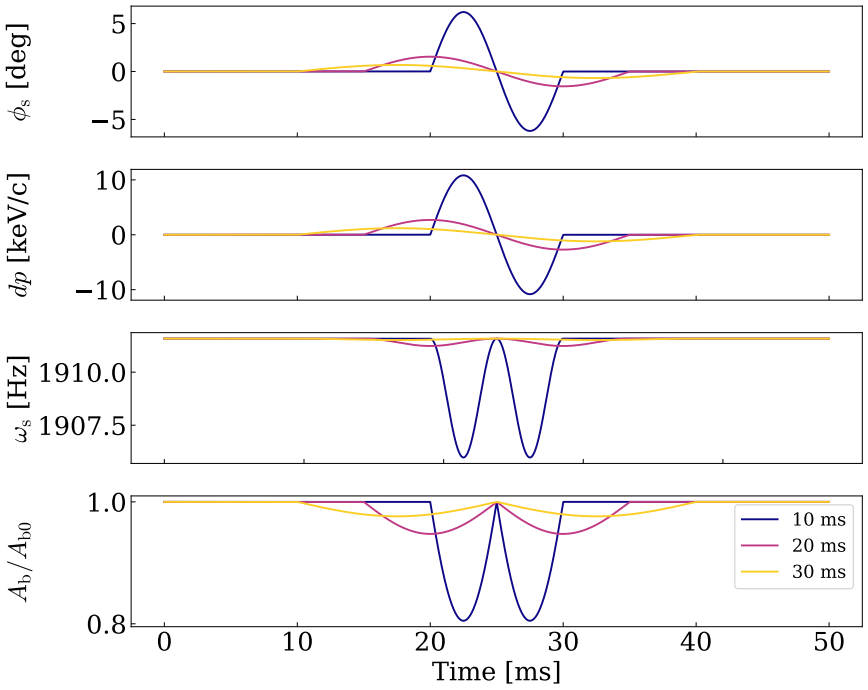

Figure 5.4: The following parameters are shown during a 10, 20 and 30 ms long manipulation with the same parameters as Fig. 5.3 from top to bottom: synchronous phase, momentum change, synchrotron frequency in the middle of the bucket and relative bucket area.

5.2.3 Adiabaticity of re-phasing

To evaluate the adiabaticity of the RF manipulation, a general adiabaticity criterion based on the bucket area change was applied, see [37] and [124, p. 303]. The conventional one based on the synchrotron frequency change [124, p. 241] does not take into account the consequences of the change of the shape of the bucket as shown below.

The relative bucket area change can be written as

$$\frac{dA}{A} = \alpha_{A_B} \omega_s dt \ . \tag{5.6}$$

For the manipulation to be adiabatic the change of the area has to be small compared to the synchrotron period as also explained for barrier buckets earlier in Chapter 2, which means:

$$\alpha_{A_B} = \left| \frac{1}{\omega_s A_B} \frac{dA_B}{dt} \right| \ll 1 \ . \tag{5.7}$$

The following calculation was performed with the conventions of [124, pp. 241–4] and separately using the variables of Eq. 2.19 leading to the same result as expected. The calculation using the former convention is presented.

Using the conventional $\alpha_\mathrm{b}(\phi_\mathrm{s})$, the bucket area factor [124, p. 243] for accelerated sinusoidal buckets and Eq. 5.7 the following is true of the change of the bucket area:

$$\frac{dA_\mathrm{B}}{dt} \sim \frac{d}{dt}\left(\frac{\omega_\mathrm{s}\alpha_\mathrm{b}(\phi_\mathrm{s})}{\sqrt{|\cos\phi_\mathrm{s}|}}\right) = \frac{\alpha_\mathrm{b}(\phi_\mathrm{s})}{\sqrt{|\cos\phi_\mathrm{s}|}}\frac{d\omega_\mathrm{s}}{dt} + \omega_\mathrm{s}\frac{d}{dt}\left(\frac{\alpha_\mathrm{b}(\phi_\mathrm{s})}{\sqrt{|\cos\phi_\mathrm{s}|}}\right) . \tag{5.8}$$

The change in α_b is much larger than the contribution of $\sqrt{|\cos\phi_\mathrm{s}|}$, around the zero stable phase where we operate, therefore:

$$\frac{dA_\mathrm{B}}{dt} \sim \alpha_\mathrm{b}\frac{d\omega_\mathrm{s}}{dt} + \omega_\mathrm{s}\frac{d\alpha_\mathrm{b}}{dt} . \tag{5.9}$$

According to Eqs. 5.7 and 5.9:

$$\alpha_{A_\mathrm{B}} = \left|\frac{1}{\omega_\mathrm{s}^2\alpha_\mathrm{b}}\left(\omega_\mathrm{s}\frac{d\alpha_\mathrm{b}}{dt} + \alpha_\mathrm{b}\frac{d\omega_\mathrm{s}}{dt}\right)\right| = \left|\frac{1}{\omega_\mathrm{s}\alpha_\mathrm{b}}\frac{d\alpha_\mathrm{b}}{dt} + \frac{1}{\omega_\mathrm{s}^2}\frac{d\omega_\mathrm{s}}{dt}\right| . \tag{5.10}$$

Neglecting the contribution of the first term in the sum Eq. 5.10 leads to the conventional adiabaticity criterion based on the change of the synchrotron frequency:

$$\alpha_\mathrm{ad} = \left|\frac{1}{\omega_\mathrm{s}^2}\frac{d\omega_\mathrm{s}}{dt}\right| . \tag{5.11}$$

However, in our case, the contribution of the first term in the sum in Eq. 5.10 is two orders of magnitude higher than the second, therefore it can not be neglected. Hence the classical adiabaticity criterion (Eq. 5.11) can not be applied.

On the other hand, neglecting the first term in 5.10 leads to an approximated adiabaticity criterion that is applicable to the phase slip:

$$\alpha_\mathrm{p} = \left|\frac{1}{\alpha_\mathrm{b}\omega_\mathrm{s}}\frac{d\alpha_\mathrm{b}}{dt}\right| \ll 1 . \tag{5.12}$$

This result highlights that the main contribution to the change in the longitudinal beam dynamics during a phase slip is not the synchrotron frequency change, but the change of the bucket area factor, which means trajectory shape and bucket area change. In other words, α_p measures the adiabaticity due to squeezing the beam into an accelerating and decelerating bucket, whereas it is insensitive to the change of the synchrotron frequency. The three adiabaticity parameters are compared in Fig. 5.5 for the proposed phase slip. The relation between the adiabaticity parameters according to the triangle inequality theorem is:

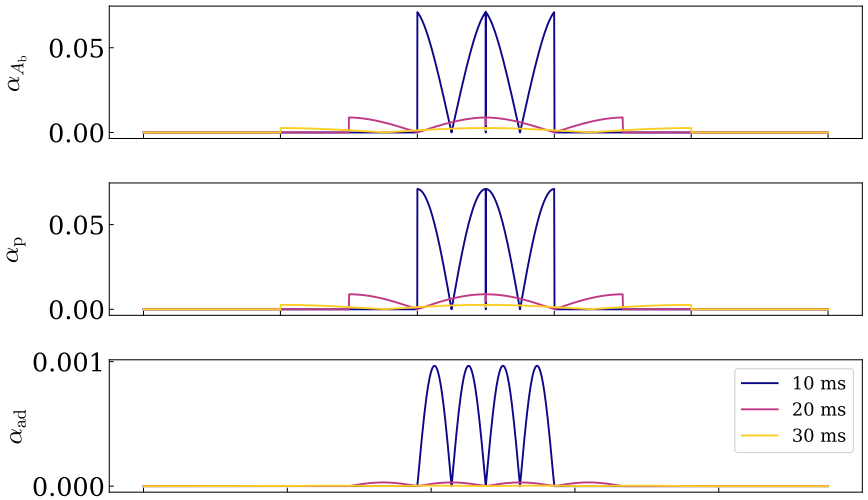

Figure 5.5: Comparison of the general adiabaticity parameter (top), the approximation valid for the phase slip operation (middle) and the conventional (bottom) one. It is clear that the main contribution comes from the change of the bucket area factor.

$$\alpha_{A_B} \leq \alpha_{ad} + \alpha_p \ . \tag{5.13}$$

A 10 ms long process is expected to be too short because the value of the relevant adiabaticity parameters is higher than 0.05, which usually indicates a non-adiabatic manipulation [124, p. 303], whereas in the other cases this value is much lower. Furthermore, the α_{A_b} and α_p curve suggests that by optimising the shape of the phase program, a faster manipulation can possibly be achieved by smoothing the discontinuity in the higher derivatives of the phase curve. This could achieve a somewhat lower peak adiabaticity.

With the analytical estimations being favourable when compared to the requirements mentioned in Table 5.1, macroparticle simulations were performed to investigate the operation further in the next section.

5.3 Simulations and benchmarking

Macroparticle simulations using the longitudinal beam dynamics code BLonD have been performed to investigate the phase slip after the beam is accelerated to 14 GeV/c flat top momentum. In addition, benchmarking with past measurements [222, 223] is also performed, since the accelerator complex was not available to test the proposed scheme with beam.

5.3.1 Benchmarking with past measurements

Validating the simulation code with previously conducted beam tests under very similar conditions in the PS in 2016 [222, 223] was possible. Although the energy of the beam and the RF frequency were different, the adiabaticity parameter range of the measurement and the current proposal is almost exactly the same as indicated in Table 5.3, hence a fair comparison can be made.

	Measurement parameter (2016)	Proposed parameter
Energy	26 GeV	14 GeV
RF frequency	40 MHz	7.6 MHz
Max. RF amplitude	100 kV	100 kV
Azimuthal change range	0–360°	0–22.5°
Time range of the manipulation	20–60 ms	10–30 ms
Peak synchrotron frequency	512 Hz	305 Hz
Adiabaticity parameter range	0.2 % – 6.4 %	0.3 % – 7.1 %

Table 5.3: Parameter comparison of the measurements in 2016 and the proposed and simulated parameters for barrier bucket synchronisation. Note the adiabaticity parameter is based on the change of the bucket area, see Eq. 5.7 and [37].

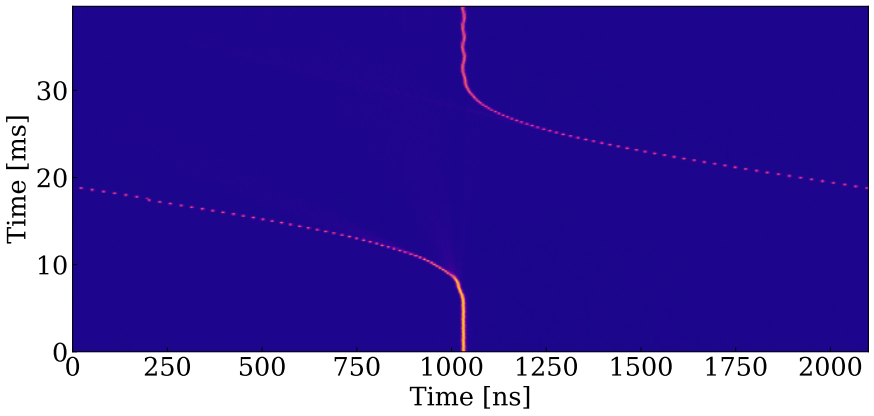

Figure 5.6: Longitudinal profile evolution during a 30 ms phase slip operation. Data from the 2016 measurements. The colours indicate the longitudinal line density from yellow (high) to blue (low).

The longitudinal line density evolution was available from the beam studies in 2016. Figures 5.7 and 5.8 provide a typical example of the longitudinal profile evolution in the simulated and measured case, for an adiabatic and non-adiabatic manipulation respectively. As Fig. 5.6 indicates, due to the high $h = 84$ harmonic number in the PS, the bunch is barely visible when looking at a whole

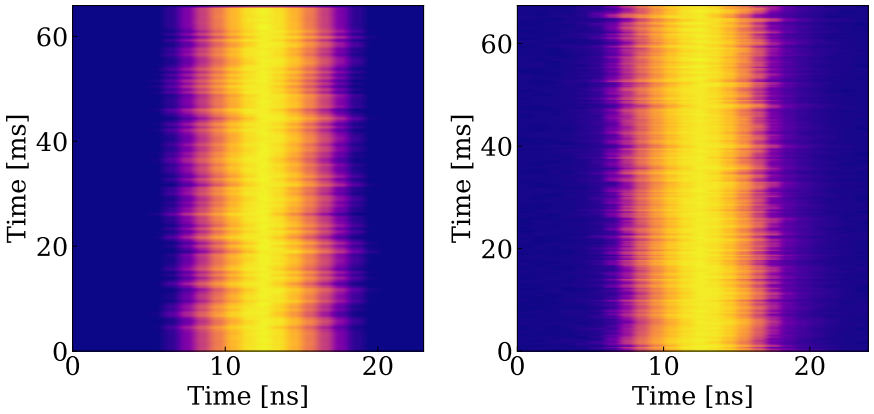

Figure 5.7: Profile evolution aligned in the coordinate system of the bunch with $\alpha_{A_\mathrm{b}} = 0.2\%$. The plot shows that with a slow manipulation the beam can follow both in the simulated (left) and in the measured (right) case, because the profile evolution is preserved. The colours indicate the longitudinal line density from yellow (high) to blue (low).

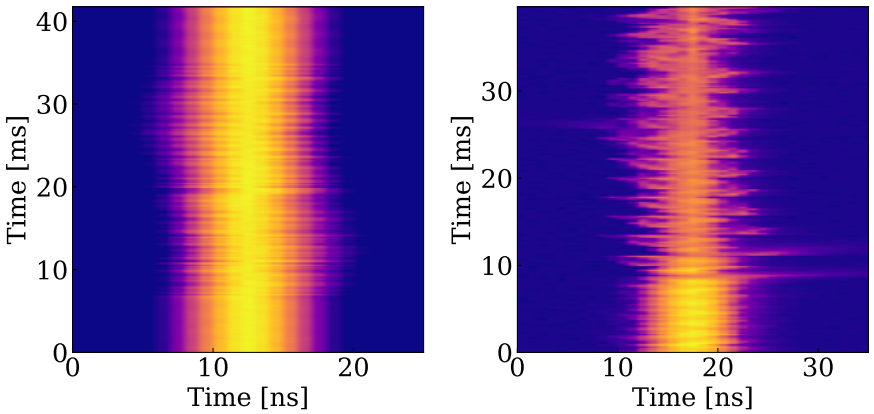

Figure 5.8: Profile evolution aligned in the coordinate system of the bunch with $\alpha_{A_\mathrm{b}} = 1.9\%$. The simulations on the left show oscillation after the manipulation. The measurements on the right show a that the beam is practically lost. This was attributed to technical problems found in the phase program. The colours indicate the longitudinal line density from yellow (high) to blue (low).

turn longitudinal profile evolution data of the phase slip. Therefore the comparison was achieved by detecting the bunch position in the whole turn profiles and aligning it along a straight line, effectively observing the manipulation in the coordinate system of the bunch.

In the case of the slow manipulations as shown in Fig. 5.7 the bunch evolution matches the measured one. This operation clearly preserves the shape of the bunch and does not excite any oscillations, which is also confirmed by the low adiabaticity parameter. The non adiabatic case of a short manipulation does not reproduce the simulation exactly as shown in Fig. 5.8. Problems with the phase program function for the measurement were found for faster manipulations. The azimuthal change was programmed as a phase change in RF harmonic number $h = 84$. During the already fast azimuthal change $h = 84$ cycles were skipped in the program according to the reconstruction, possibly causing an abrupt phase change leading to an even less adiabatic manipulation. Nevertheless, the adiabaticity parameter and the presence of the oscillations in the simulated case shows that this manipulation is unacceptably fast, anyway. Further beam tests are planned after the accelerator shutdown to test the operation.

5.3.2 Simulation results

With the 2016 measurement data analysed and the simulation code benchmarked, the proposed phase slip operation was programmed in BLonD as indicated by Table 5.3.

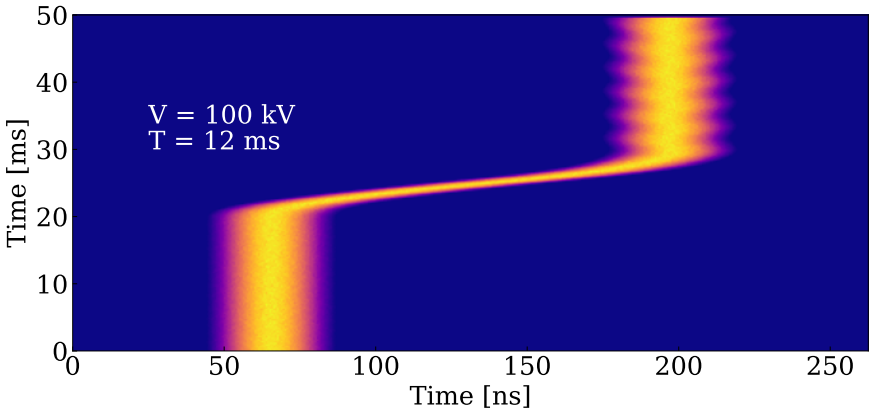

Figure 5.9: Simulated longitudinal profile evolution during a fast, 12 ms $h = 16$ displacement. This time is too short for the manipulation as shown by the oscillations. The colours indicate the longitudinal line density from yellow (high) to blue (low).

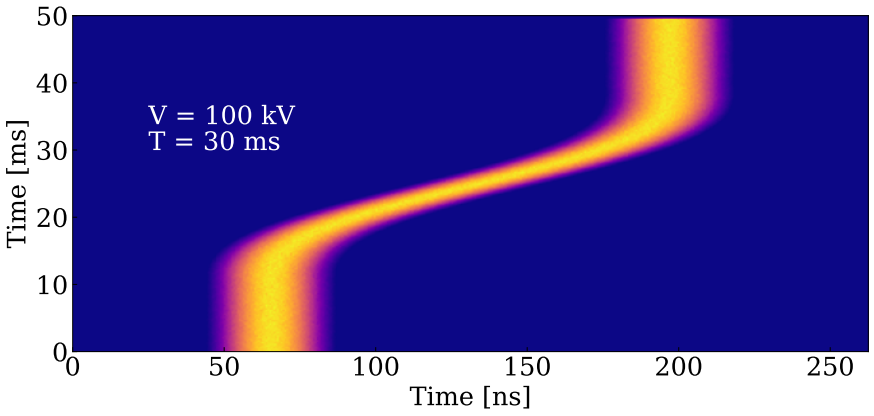

Figure 5.10: The simulated longitudinal profile evolution during a slower, 30 ms $h = 16$ displacement. This time is sufficient for the manipulation as shown by the lack of oscillations. The colours indicate the longitudinal line density from yellow (high) to blue (low).

A scan was performed for a manipulation in $10 - 36$ ms with an RF voltage of 100 kV, which already underestimates the current value in the fixed target cycle at flat top by 15%. However, the RF system in the PS can output a maximum of 200 kV providing a substantial margin.

Two example cases are shown for the simulated longitudinal profile evolution during an azimuthal displacement of a bunch by $2\pi/16$ ($h = 16$). Fig. 5.9 illustrates a worst, 12 ms case showing the highest oscillations in the probed range due to the fast bump coupling to the synchrotron oscillations of the beam.

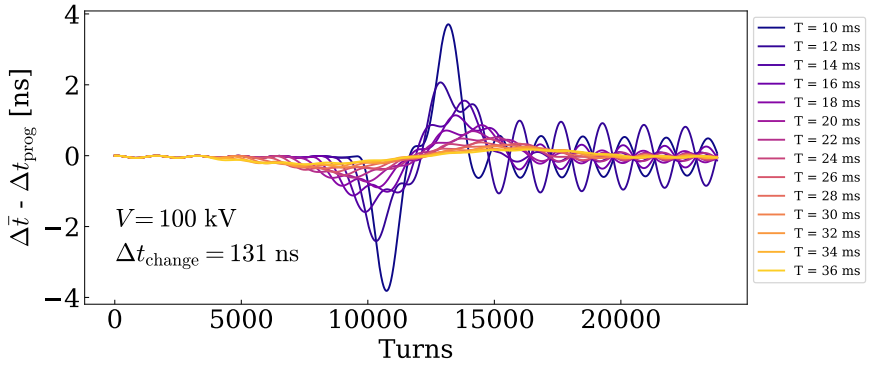

Figure 5.11: The time difference between the average bunch position and the programmed position for various durations of the phase shift manipulation. The initial oscillations are an artefact of the imperfect matching in the simulations.

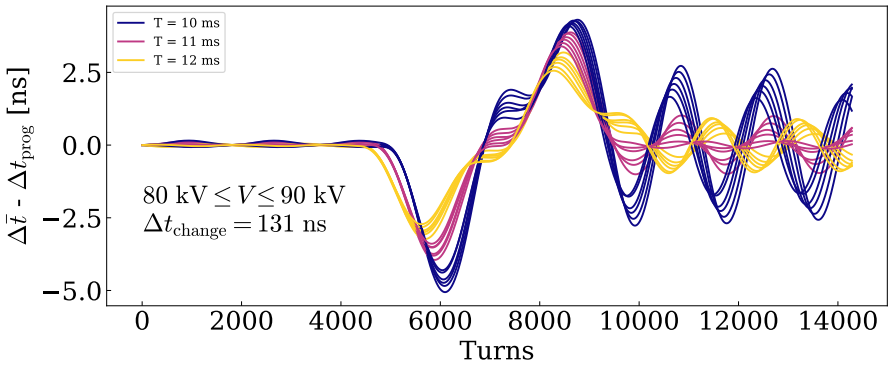

Figure 5.12: The dependence of the position on the voltage and time available. The higher the peak amplitude, the lower the amplitude of the oscillations and, in general, the longer the time, the lower the oscillations. Due to the non-linearity of the synchrotron oscillations bunch oscillations are very sensitive to the length of the manipulation.

For an almost three times longer manipulation with a duration of 30 ms, as depicted in Fig. 5.10, the situation is much improved. There are no noticeable dipole oscillations visible at the resolution of the plot.

To provide a more systematic picture on the time scale of the operation, the difference between the simulated and the expected mean position in time was calculated and the results shown in Fig. 5.11. Lower RF voltages and shorter times lead to stronger oscillations in general, but not always. For example a 12 ms manipulation causes slightly higher amplitude oscillations than the one executed in 10 ms, due to a resonance with the synchrotron frequency as mentioned earlier. However, beyond approximately 20 ms the bunch oscillations decrease for a longer manipulation. When reaching 30 ms in duration, the manipulation does not induce any noticeable degradation of the longitudinal beam quality. The initial oscillation is a result of an imperfect matching of the particles at the beginning of the simulation as it can be seen in Fig. 5.11. The same random seed was used to generate the initial conditions in this case such that the initial oscillations are the same.

A scan of the voltage shows (Fig. 5.12), as expected, that the lower voltages result in higher oscillations, because the bunch in this case occupies a larger area in the bucket and as the duration of the operation gets longer, non-linearity of the synchrotron oscillations, but it still degrades the longitudinal beam quality by causing an emittance increase. Following this campaign of simulations, a duration of 30 ms for the azimuthal alignment as part of the synchronisation seems adequate. Beam studies will be conducted to confirm this.

5.4 Implementation

The steps of the implementation are illustrated in Figs. 5.13 – 5.16 and summarised Table 5.4.

Upon arrival at the flat-top in the PS, the open loop revolution frequency of the PS is set to the one obtained from the measured bending field during the acceleration phase. Since the PS phase loop is initially closed, see Fig. 5.13, the effect of this synchronisation on the beam is not visible.

Once this is achieved, the radial phase loop gains are reduced to zero, see Fig. 5.14, thereby a fixed frequency is achieved. Because the phase loop is off, the resolution (LSB) of the phase program will cause a drift. Therefore, the resolution of the master clock [224] needs to be taken into account not to cause a larger than a few ns displacement in the gap position at extraction.

Assuming re-using the present hardware the LSB of the master clock is 0.23 Hz. This integrated over 200 ms amounts to less than 500 ps time difference of the expected and actual gap position in the worst case. Before performing the phase slip operation, the RF phase versus the extraction phase is measured in harmonic number 16, then an appropriate phase bump is applied to move the gap by the difference in phase, see Fig. 5.15. As a result, the beam is at the correct azimuthal position for barrier bucket generation modulo $2\pi/16$. The position of the gap is ideally the same as the setpoint of the phase bump, since the gap is to be generated between two bunches. Therefore this is known and can be controlled in the present firmware for the barrier bucket drive. The accuracy depends on the accuracy of the phase slip, which based on the simulations the beam can follow.

Since the azimuthal position of the beam does not have to be changed any more, the main RF voltage can be lowered and the transverse splitting can take place. At the end of this process, the barrier voltage is increased as the main RF voltage goes from a low value to zero and the re-bucketing is performed with the gap made at the correct azimuthal position.

The new manipulation would require only a little more time to be available in the cycle. Table 5.5 shows the estimated durations needed for the individual steps of the synchronisation process.

No.	Main sequence	Detailed steps
1	Establish pre-conditions for synchronisation	• Smooth switch from B-train frequency reference to SPS RF reference, see also Fig. 5.13. • Reduce phase loop gain to zero, see also Fig. 5.14. • Reduce radial loop gain to zero.
	Result	PS RF open-loop frequency is synchronous with SPS RF.
2	Move the bunch to the nearest gap position, see also Fig. 5.15.	• Perform phase measurement. • Program and perform phase bump by acting on the master clock frequency.
	Result	Gap between $h = 16$ buckets is in the correct position to be replaced by gap made by the barrier bucket.
3	Barrier bucket and transverse splitting, see also Fig. 5.16.	• Reduce main RF voltage from about 100 kV to about 12 kV. • Perform transverse splitting. • Set barrier bucket azimuth to gap position, which is automatically synchronous with the PS extraction kickers. • Re-bucketing: reduce main RF voltage from 12 kV to zero. Simultaneously increase barrier voltage to $2 - 4$ kV depending on gap size.
	Result	Gap in beam made synchronously with PS extraction kickers and SPS injection kickers.
4	Beam transfer	• Trigger beam transfer elements based on signals derived from SPS RF
	Result	PS extraction and SPS injection kickers switch simultaneously with gap in line density.

Table 5.4: Steps of the proposed synchronisation.

Manipulation	t_0	Duration (ms)
Match PS-SPS frequency at flat-top	t_0	5
Perform phase measurement	$t_0 + 5$	5
Phase bump	$t_0 + 10$	30
Barrier manipulation		no added time

Table 5.5: An example of the timings needed for the synchronisation.

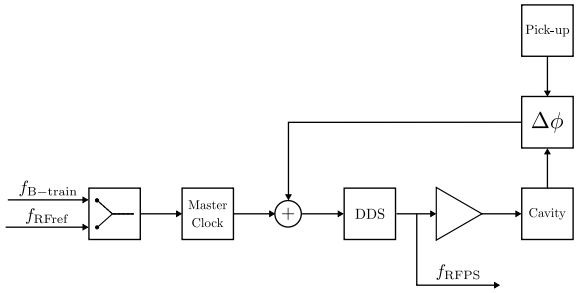

Figure 5.13: Step 1: Switch from B-train reference to external RF reference of the revolution frequency.

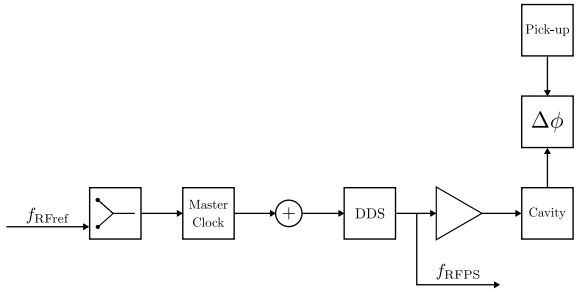

Figure 5.14: Step 2: Reduce phase and radial loop gain to zero.

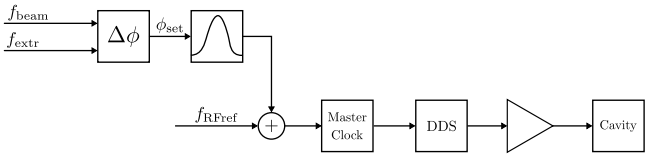

Figure 5.15: Step 3: measure phase difference and perform phase bump by acting on the frequency of the master clock.

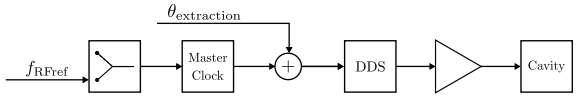

Figure 5.16: Step 4. Perform transverse splitting and generate barrier bucket by increasing the amplitude of the wide-band RF connected to the Finemet® cavity.

5.5 Summary

The proposed synchronisation scenario for the gaps generated by the barrier bucket system with azimuthal positions required for the beam in the SPS is different from a conventional bunch to bucket transfer. In order to align the gap in the PS, the mean energy of the beam has to be temporarily changed during unfavourable conditions such as: a relatively short time available for the manipulation; the low RF voltage available from all RF systems during the transverse splitting; the low synchrotron frequencies in barrier buckets and potentially small radial displacement allowed by the MTE on top of the usual aperture limitation. Short time and small radial displacement, in addition, are conflicting requirements. On the other hand, compared to a conventional bunch to bucket transfer, the accuracy of the synchronisation can be an order of magnitude lower.

A fast synchronisation by placing the barrier between two bunches is possible with the gaps generated between the $h = 16$ bunches. This allows for a short $2\pi/16$ azimuthal phase slip while achieving effectively a harmonic one synchronisation. Furthermore, the synchronisation is performed with the main RF system before the transverse splitting takes place, when sufficient RF voltage is still available to rapidly change the mean energy of the beam.

Analytical calculations of the bucket parameters during the phase bump showed that the operation is feasible within a few tens of milliseconds. These were complemented by macroparticle simulations of the manipulation, which confirmed the analytical estimates. The simulation code was successfully benchmarked against previous beam measurements in the PS.

The parameters used in the analytical calculations and in the simulations were conservative. An ideal manipulation would only require a maximum of $2\pi/32$ azimuthal change when two directional movement is applied around the circumference of the PS. Yet, the twice, $2\pi/16$ has been included with the assumption that the phase slip is only performed in one direction. Furthermore, the increased injection energy of the PS after LS2 should be able to provide further margin to accommodate the manipulations in this cycle.

Machine development studies to validate the steps of this synchronisation scheme are foreseen during the upcoming run of the accelerators at CERN.

Chapter 6

Conclusions

6.1 Summary of contributions

The three main contributions of this thesis are summarised in the following three sections: the implementation of the LLRF drive signal for barrier buckets in the PS, the subsequent commissioning and beam tests including the significant beam loss reduction at extraction and the proposal for synchronisation of barrier buckets between the PS and SPS.

6.1.1 Implementation

The requirements of the barrier parameters were analysed which confirmed the compatibility with the existing PS Finemet® cavity and its high power level RF installation. In order effectively reduce the losses, the duration of the pulse has to cover the kicker rise times, defining the bandwidth requirement. The amplitude has to be sufficiently high to contain the beam in the barrier bucket for a given pulse length. The emittance was measured during the cycle and cross-checked with simulations after de-bunching, form this the amplitude requirement was calculated.

The waveform shape to generate a stationary barrier bucket is essentially a free parameter as long as it has a flat part and has no DC component as detailed in Chapters 2 and 3. Following a comparison of a few typical waveform shapes, the isolated sine wave based implementation was chosen as a compromise between bandwidth and bucket height. A general smoothing scheme was also introduced to limit the bandwidth of any kind of waveform.

The concept of the waveform generator was developed and implemented in programmable logic. A beam synchronous, swept clock digital synthesizer with a remotely programmable arbitrary waveform look-up table [3] was selected,

because it is synchronous with conventional RF signals, flexible and it is easy to implement evolved manipulations such as moving barriers. It has the added benefit of compatibility with the existing low-level RF infrastructure in the PS. The hardware was installed and commissioned successfully.

A linear pre-distortion scheme was developed based on the transfer function measurement of the cavity and amplifier system. Since the behaviour of the cavity does not drift significantly with time nor with beam intensity, no further adjustments were necessary to this data-based model during the beam tests.

To simulate the behaviour of the beam in barrier buckets, all barrier tests were compared to extensive tracking simulations in BLonD with the same features as the hardware implementation, which allowed accurate simulations of the beam dynamics with beam loading.

6.1.2 Beam test and loss reduction

First beam tests with a single barrier were performed to validate the proof-of-principle and to calibrate its phase with respect to the beam. This initial commissioning was successful. Special cycles were set up at injection energy, which allowed to control the initial conditions of the beam in isolated and barrier buckets. This, in turn, allowed to conduct more sophisticated tests to compare the adiabaticity of the barrier compression and decompression against literature. The results were in agreement with predictions and beam tests performed in other laboratories as detailed in [2] and Chapter 4.

Following the low intensity and low energy beam tests, the energy and the intensity of the beam was increased to test the barrier bucket extraction scheme close to its foreseen operational conditions. The fixed target cycle was modified to remove the transverse splitting. This allowed to check the re-bucketing process from the $h = 16$ bunches to the barrier bucket at flat top in the PS with 14 GeV/c momentum. It was established that for symmetry reasons the gap made by the barrier has to be between two $h = 16$ bunches to obtain a symmetric bunch profile at extraction.

The barrier buckets were combined with the transversely split beam in the PS with great success, which is the main original result [1] of the present studies. Subsequently, the longitudinal beam profiles were analysed in detail and it was established that the extraction scheme scales works very well up to the highest beam intensity.

The analysis of the beam loss monitor data confirmed the significant loss reduction at extraction form the PS across all beam intensities.

6.1.3 Synchronisation

To benefit from the beam loss reduction scheme, the barrier bucket generation in the PS has to be synchronised with the injection in the SPS. For this to happen the beam has to be moved in azimuth, which requires slight acceleration and deceleration in the PS. The main constraint for acceleration is that very near to the extraction there is no sufficient RF voltage to accelerate or decelerate the beam with any of the RF systems available, because of the low momentum spread required for the Multi-turn Extraction.

Introducing additional time just before the transverse splitting takes place, where there is still sufficient voltage from the main, $h = 16$ RF system to move the bunches was explored. If the position of the barrier is locked to the gaps between the $h = 16$ bunches, then maximum only a $2\pi/16$ azimuthal movement of the beam is sufficient in the worst case to synchronise the gap with the SPS.

Analytical calculations were performed to investigate the adiabaticity of the operation. A phase slip in the order of few tens of milliseconds could move the beam adiabatically for the gap to be at the right position at extraction. Particle tracking simulations confirmed this, which were benchmarked with previous measurements in the PS as the accelerator complex was not available for beam measurements during LS2.

6.2 Future work

The feasibility of the barrier bucket operation for beam loss reduction in the PS was established and the natural next step is to put the scheme in operation.

Approximately 50 ms time seems to be reasonable for the complete synchronisation process. The time for this must be found within the fixed target cycle. Therefore, the post LS2 fixed target cycle in the PS has to be analysed and optimised to accommodate the synchronisation. This is foreseen to include an optimisation of the de-bunching process at the end of the fixed target cycle. The shape of the phase curve could be also tuned with respect to the adiabaticity criterion shown in Chapter 6, which could possibly shorten the time for the operation or improve the adiabaticity for the same duration.

Although the main steps of the synchronisation have been proposed in Chapter 5, further technical details remain to be elaborated. The steps of the smooth handover from the PS to the SPS frequency have to be established. The measurement of the phase after arrival on the flat top in the PS needs to be developed an implemented in detail. The question whether one phase measurement before the phase bump is sufficient or not has to be investigated also with beam. The technical details of the beam control of the frequency bump have to be

ascertained. Further integration of the barrier bucket drive in the sequence of synchronisation has to be established.

Following the path of the fixed target beam in the accelerator chain, after a successful synchronisation, the next step is acceleration in the SPS. The consequences of the gaps in the beam in the SPS and the impact on the experiments have to be analysed and studied with beam especially with respect to transient beam loading, since empty gaps have to be compensated by a larger line density to keep the total intensity equally high. In addition, the detailed analysis of the SPS ring performance for MTE beams in combination with the barrier bucket is needed with the goal of quantitatively assessing the overall performance of this new beam process.

Bibliography

1. M. Vadai, A. Alomainy, H. Damerau, S. Gilardoni, M. Giovannozzi, A. Huschauer. *Barrier bucket and transversely split beams for loss-free multi-turn extraction in synchrotrons. EPL* **128,** 14002. 7 p (2019).
2. M. Vadai, A. Alomainy, H. Damerau, Heiko, S. Gilardoni, M. Giovannozzi, A. Huschauer. *Beam manipulations with barrier buckets in the CERN PS.* 2019 J. Phys.: Conf. Ser. 1350 012088.
3. M. Vadai, A. Alomainy, H. Damerau. *Barrier bucket studies in the CERN PS.* Proc. 10th Int. Particle Accelerator Conf. (IPAC'19), Melbourne, Australia, May 2019, pp. 1128–1131. MOPTS106.
4. CERN. *NA58/COMPASS, COmmon Muon and Proton Apparatus for Structure and Spectroscopy, The CERN Experimental Programme, Grey Book database* Accessed: 07-01-2020. `https://greybook.cern.ch/greybook/experiment/detail?id=NA58`.
5. CERN. *NA61/SHINE, Study of Hadron Production in Hadron-Nucleus and Nucleus-Nucleus Collisions at the CERN SPS, The CERN Experimental Programme, Grey Book database* Accessed: 07-01-2020. `https://greybook.cern.ch/greybook/experiment/detail?id=NA61`.
6. CERN. *NA62, Proposal to Measure the Rare Decay K+ -> pi+ nu nu at the Cern SPS, The CERN Experimental Programme, Grey Book database* Accessed: 07-01-2020. `https://greybook.cern.ch/greybook/experiment/detail?id=NA62`.
7. CERN. *NA63, Electromagnetic Processes in strong Crystalline Fields, The CERN Experimental Programme, Grey Book database* Accessed: 07-01-2020. `https://greybook.cern.ch/greybook/experiment/detail?id=NA63`.
8. CERN. *NA64, Search for dark sectors in missing energy events, The CERN Experimental Programme, Grey Book database* Accessed: 07-01-2020. `https://greybook.cern.ch/greybook/experiment/detail?id=NA64`.

9. CERN. *NA65/DsTau, Study of tau neutrino production, The CERN Experimental Programme, Grey Book database* Accessed: 07-01-2020. https://greybook.cern.ch/greybook/experiment/detail?id=NA65.

10. A. Ceccucci, G. Mallot, L. Gatignon. *Fixed target, striking physics.* Accessed: 07-01-2020. https://cerncourier.com/a/fixed-target-striking-physics/.

11. Vretenar, M. *et al. Linac4 design report* (CERN Yellow Reports: Monographs 6/2020, CERN, Geneva).

12. E. Mobs. *The CERN accelerator complex - 8ust 2018. Complexe des accélérateurs du CERN - Août 2018.* 8 2018, Image ID: OPEN-PHO-ACCEL-2018-005, accessed: 07/01/2020. https://cds.cern.ch/record/2636343.

13. C. Bovet, D. Fiander, L. Henny, A. Krusche, G. Plass. *The Fast Shaving Ejection for Beam Transfer from the CPS to the CERN 300 GeV Machine. IEEE Transactions on Nuclear Science* **20,** 438 (June 1973).

14. D. C. Fiander, D. Grier, K. D. Metzmacher, P. Pearce. *A modulated fast bump for the CPS continuous transfer. IEEE Trans. Nucl. Sci.* **24,** 1340–2 (1977).

15. G. Arduini, G. Crockford, M. Giovannozzi, K. Hanke, D. Manglunki, M. Martini, G. Métral, C. Niquille. *TT2/TT10 Transfer Line Studies for the 14 GeV/C Continuous Transfer.* SL-Note-99-013-MD (Mar. 1999).

16. J. Borburgh, S. Dam1ovic, S. Gilardoni, M. Giovannozzi, C. Hernalsteens, M. Hourican, A. Huschauer, K. Kahle, G. Le Godec, O. Michels, G. Sterbini. *First implementation of transversely split proton beams in the CERN Proton Synchrotron for the fixed-target physics programme. Europhys. Lett.* **113,** 34001. 6 p (2016).

17. M. Giovannozzi et. al. *The CERN PS multi-turn extraction based on beam splitting in stable islands of transverse phase space: Design Report* CERN-2006-011 (CERN, Geneva, 2006).

18. R. Cappi, M. Giovannozzi. *Novel Method for Multiturn Extraction: Trapping Charged Particles in Islands of Phase Space. Phys. Rev. Lett.* **88,** 104801 (10 Feb. 2002).

19. Y. Suetsugu, K. Shibata, A. Morishige, Y. Suzuki, M. Tsuchiya. *Design study of a movable mask with low beam impedance. Phys. Rev. ST Accel. Beams* **9,** 103501 (10 Oct. 2006).

20. A. Franchi, S. Gilardoni, M. Giovannozzi. *Progresses in the studies of adiabatic splitting of charged particle beams by crossing nonlinear resonances. Phys. Rev. ST Accel. Beams* **12,** 014001 (1 Jan. 2009).

21. S. Abernethy, A. Akroh, H. Bartosik, A. Blas, T. Bohl, S. Cettour-Cave, K. Cornelis, H. Damerau, S. Gilardoni, M. Giovannozzi, C. Hernalsteens, A. Huschauer, V. Kain, D. Manglunki, G. Métral, B. Mikulec, B. Salvant, J.-L. Sanchez Alvarez, R. Steerenberg, G. Sterbini, Y. Wu. *Operational performance of the CERN injector complex with transversely split beams. Phys. Rev. Accel. Beams* **20,** 014001. 21 p (2017).

22. A. Huschauer, A. Blas, J. Borburgh, S. Dam1ovic, S. Gilardoni, M. Giovannozzi, M. Hourican, K. Kahle, G. Le Godec, O. Michels, G. Sterbini. *Transverse beam splitting made operational: Key features of the multiturn extraction at the CERN Proton Synchrotron. Phys. Rev. Accel. Beams* **20,** 061001. 15 p (2017).

23. A. Huschauer, M. Giovannozzi, O. Michels, A. Nicoletti, G. Sterbini. *Analysis of performance fluctuations for the CERN Proton Synchrotron multiturn extraction. Journal of Physics: Conference Series* **874,** 012072 (July 2017).

24. M. Giovannozzi et al. Results from the 2009 Beam Commissioning of the CERN Multi-turn Extraction. Proc. 1st Int. Particle Accelerator Conf. (IPAC'10), Kyoto, Japan, May 2010, paper THOBMH02, pp. 3619–3621.

25. M. Giovannozzi, J. Borburgh, S. S. Gilardoni, H. Bartosik, D. Bodart, R. J. Brown, S. Dam1ovic, C. Hernalsteens, M. Hourican, M. Widorski, B. Goddard. *Proposal of a Dummy Septum to Mitigate Ring Irradiation for the CERN PS Multi-Turn Extraction.* Proc. 3rd Int. Particle Accelerator Conf. (IPAC'12), New Orleans, LA, USA, May 2012, paper MOPPD059, pp. 499–501.

26. M. Giovannozzi, S. S. Gilardoni, C. Hernalsteens, A. Lachaize, G. Metral. *Modified Extraction Scheme for the CERN PS Multi-Turn Extraction.* Proc. 3rd Int. Particle Accelerator Conf. (IPAC'12), New Orleans, LA, USA, May 2012, paper MOPPD060, pp. 502–504.

27. L. N. Drosdal, A. Ulsroed, M. Giovannozzi, S. S. Gilardoni, H. Bartosik, C. Hernalsteens, A. Lachaize, Y. Papaphilippou. *Design and Beam Measurements of Modified Fast Extraction Schemes in the CERN PS for Installing a Dummy Septum to Mitigate Ring Irradiation.* Proc. 4th Int. Particle Accelerator Conf. (IPAC'13), Shanghai, China, May 2013, paper WEPEA056, pp. 2633–2635.

28. C. Hernalsteens, S. Dam1ovic, S. S. Gilardoni, M. Giovannozzi. *Numerical Simulations to Evaluate the Performance of CERN PS Dummy Septum to Reduce Irradiation for the Multi-Turn Extraction.* Proc. 4th Int.

Particle Accelerator Conf. (IPAC'13), Shanghai, China, May 2013, paper WEPEA057, pp. 2636–2638.

29. C. Bertone, J. Borburgh, D. Bodart, R. Brown, S. Burger, S. Dam1ovic, P. Demarest, R. Fernandez Ortega, J. A Ferreira Somoza, D. Gerard, S. Gibson, S. Gilardoni, M. Giovannozzi (ed.), G. Le Godec, C. Hernalsteens, M. Hourican, N. J urado, J.-M. Lacroix, S. Mataguez, G. Métral, C. Pasquino, E. Perez-Duenas, S. Persichelli, B. Salvant, R. Steerenberg, P. van Trappen. *Studies and implementation of the PS dummy septum to mitigate irradiation of magnetic septum in straight section 16* CERN-ACC-2014-0043 (Apr. 2014).

30. R. Garoby. *RF gymnastics in synchrotrons*. CAS - CERN Accelerator School: Specialised Course on RF for Accelerators; 8 - 17 Jun 2010, Ebeltoft, Denmark, 16 p (Dec. 2011).

31. S. Persichelli, M. Migliorati, M. M. Paoluzzi, B. Salvant. *Impedance Studies for the PS Finemet® Loaded Longitudinal Damper*. Proc. 5th Int. Particle Accelerator Conf. (IPAC'14), Paper TUPRI060, Dresden, Germany, Jun. 2014.

32. Hitachi Metals Ltd. *Nanocrystalline Soft Magnetic Material FINEMET®* Accessed: 07-01-2020. `https://www.hitachi-metals.co.jp/e/products/elec/tel/p02_21.html`.

33. M. Paoluzzi, H. Damerau. *Design of the PS longitudinal damper*. CERN-ACC-NOTE-2013-0019 (2013).

34. L. L. Foldy. *A method for expanding the phase-stable regime in synchronous accelerators. Il Nuovo Cimento (1955-1965)* **19,** 1116–1120. ISSN: 1827-6121 (Mar. 1961).

35. J. E. Griffin, C. Ankenbrandt, J. A. MacLachlan, A. Moretti. *Isolated Bucket RF Systems in the Fermilab Antiproton Facility*. Proc. 10th Particle Accelerator Conf. (PAC'83), Santa Fe, NM, USA, Mar. 1983, pp. 3502–3505.

36. S. Y. Lee, K. Y. Ng. *Particle dynamics in storage rings with barrier rf systems. Phys. Rev. E* **55,** 5992–6001 (5 May 1997).

37. K. Y. Ng. *Continuous multiple injections at the Fermilab Main Injector. Phys. Rev. ST Accel. Beams* **5,** 061002 (6 June 2002).

38. C. M. Bhat. *Barrier RF Systems in Synchrotrons*. Proc. 9th European Particle Accelerator Conf. (EPAC'04), Lucerne, Switzerland, Jul. 2004, paper THOBCH03.

39. C. M. Bhat. *Longitudinal momentum mining of beam particles in a storage ring. Physics Letters A* **330,** 481–486. ISSN: 0375-9601 (2004).

40. W. Chou, D. Capista, E. Griffin, K. Y. Ng, D. Wildman. *Fast Beam Stacking using RF Barriers*. Proc. 22nd Particle Accelerator Conf., Albuquerque, NM, USA, Jun. 2007, paper TUPAS014, pp. 1682–1684.

41. G. Jackson. *Operational Experience with the Permanent Magnet Recycler Ring at Fermilab*. Proc. 7th European Particle Accelerator Conf. (EPAC'00), Vienna, Austria, Jun. 2000, paper MOP5B01.

42. M. Hu. *The Fermilab Recycler Ring*. Proc. 19th Particle Accelerator Conf. (PAC'01), Chicago, IL, USA, Jun. 2001, paper MOPA006.

43. S. Mishra. *Status of the Fermilab Recycler Ring*. Proc. 8th European Particle Accelerator Conf. (EPAC'02), Paris, France, Jun. 2002, paper MOPLE035.

44. M. Hu, D. R. Broemmelsiek, B. Chase, J. L. Crisp, N. Eddy, P. W. Joireman, K. Y. Ng. *Uniform Longitudinal Beam Profiles in the Fermilab Recycler Using Adaptive RF Correction*. Proc. 22nd Particle Accelerator Conf. (PAC'07), Albuquerque, NM, USA, Jun. 2007, paper MOPAS011, pp. 458–460.

45. M. Fujieda, Y. Iwashita, A. Noda, Y. Mori, C. Ohmori, Y. Sato, M. Yoshii, M. Blaskiewicz, J. M. Brennan, T. Roser, K. S. Smith, R. Spitz, A. Zaltsmann. *Barrier bucket experiment at the AGS*. *Phys. Rev. ST Accel. Beams* **2,** 122001 (12 Dec. 1999).

46. M. Brennan, T. Roser. *High Intensity Performance of the Brookhaven AGS*. Proc. 5th European Particle Accelerator Conf. (EPAC'96), Sitges, Spain, Jun. 1996, paper TUP011G.

47. M. Blaskiewicz, J. M. Brennan. *A Barrier Bucket Experiment for Accumulating De-bunched Beam in the AGS*. Proc. 5th European Particle Accelerator Conf. (EPAC'96), Sitges, Spain, Jun. 1996, paper MOP002G.

48. M. Fujieda, Y. Iwashita,Y. Mori, H. Nakayama, C. Ohmori, K. Saito, Y. Sato, S. Sawada, A. Takagi, Y. Tanabe, M. Toda, T. Uesugi, M. Yamamoto, T. Yan, M. Yoshii. *An RF Cavity for Barrier Bucket Experiment in the AGS*. Proc. 1st Asian Particle Accelerator Conf. (APAC'98), Tsukuba, Japan, Mar. 1998, paper 5D012.

49. L. A. Ahrens, J. G. Alessi, M. M. Blaskiewicz, J. M. Brennan, K. A. Brown, C. J. Gardner, J. W. Glenn, T. Roser, K. S. Smith, W. K. van Asselt, S. Y. Zhang. *High Intensity Performance of the Brookhaven AGS*. Proc. 18th Particle Accelerator Conf. (PAC'99), New York, NY, USA, Mar. 1999, paper FRAR3.

50. C. Ohmori, M. Fujieda, S. Machida, Y. Mori, H. Nakayama, K. Saito, S. Sawada, Y. Tanabe, M. Yamamoto, E. Ezura, A. Takagi, M. Toda, M. Yoshii, T. Tanabe, T. Uesugi. *A Wideband RF Cavity for JHF Synchrotrons*. Proc. 17th Particle Accelerator Conf. (PAC'97), Vancouver, Canada, May 1997, paper 8P041.

51. M. Fujieda, S. Machida, Y. Mori, H. Nakayama, C. Ohmori, Y. Sato, A. Takagi, Y. Tanabe, M. Toda, T. Uesugi, M. Yamamoto, M. Yoshii, Y. Iwashita. *MA-Loaded Cavities For Barrier Bucket Experiment*. Proc. 6th European Particle Accelerator Conf. (EPAC'98), Stockholm, Sweden, Jun. 1998, paper TUP14G.

52. M. Fujieda, Y. Iwashita, A. Noda, Y. Mori, C. Ohmori, Y. Sato, M. Yoshii, M. M. Blaskiewicz, J. M. Brennan, T. Roser, K. S. Smith, R. Spitz, A. Zaltsman. *Magnetic Alloy Loaded RF Cavity for Barrier Bucket Experiment at the AGS*. Proc. 18th Particle Accelerator Conf. (PAC'99), New York, NY, USA, Mar. 1999, paper MOP81.

53. J.M. Brennan, J. Brodowski, M. Meth, K.A. Rogers, R. Spitz, M. Yoshii, A. Zaltsman. *Design of Ferrite Loaded High Voltage Barrier Cavity*. Proc. 6th European Particle Accelerator Conf. (EPAC'98), Stockholm, Sweden, Jun. 1998, paper TUP22G.

54. E. Ezura, M. Fujieda, Y. Mori, R. Muramatsu, H. Nakayama, C. Ohmori, Y. Sato, A. Takagi, M. Toda, T. Uesugi, M. Yamamoto, M. Yoshii, M. Kanazawa, K. Noda. High Field-Gradient Cavities Loaded with Magnetic Alloys for Synchrotrons. Proc. 18th Particle Accelerator Conf. (PAC'99), New York, NY, USA, Mar. 1999, paper THAL1.

55. K. Torikai, Y. Arakida, S. Inagaki, K. Ishibashi, J. Kishiro, K. Koseki, E. Nakamura, K. Takayama, T. Toyama, M. Wake. *Design Study of 1 MHz Induction Cavity for Induction Synchrotron*. Proc. 20th Particle Accelerator Conf. (PAC'03), Portland, OR, USA, May 2003, paper TPPB079.

56. C. M. Bhat. *A New Technique for Making Bright Proton Bunches using Barrier RF Systems*. Proc. 21st Particle Accelerator Conf. (PAC'05), Knoxville, TN, USA, May 2005, paper TPAP021.

57. C. M. Bhat, B. Chase, C. Gattuso, P. W. Joireman. *Longitudinal Momentum Mining of Antiprotons at the Fermilab Recycler: Past, Present, and Future*. Proc. 22nd Particle Accelerator Conf. (PAC'07), Albuquerque, NM, USA, Jun. 2007, paper WEOCKI04, pp. 1941–1943.

58. K. Y. Ng. *Stability of Barrier Buckets with Short or Zero Barrier Separations*. Proc. 21st Particle Accelerator Conf. (PAC'05), Knoxville, TN, USA, May 2005, paper TPAT018.

59. O. Boine-Frankenheim. *rf barrier compression with space charge. Phys. Rev. ST Accel. Beams* **13,** 034202 (3 Mar. 2010).

60. B. Beaudoin, I. Haber, R. A. Kishek. *Barrier Shock Compression with Longitudinal Space Charge.* Proc. 6th Int. Particle Accelerator Conf., Richmond, VA, USA, May 2015, pp. 646–648.

61. O. Boine-Frankenheim, V. Kornilov. *Implementation and validation of space charge and impedance kicks in the code PATRIC for studies of transverse coherent instabilities in the FAIR rings.* Proc. 9th Int. Computational Accelerator Physics Conf. (ICAP'06), Chamonix, Switzerland, Oct. 2006, paper WEA3MP04, pp. 267–270.

62. T. Kikuchi, J. Dietrich, T. Katayama, R. Maier, D. Prasuhn, H. Stockhorst. *Simulation Study of Simultaneous Use of Stochastic Cooling and Electron Cooling with Internal Target at COSY and HESR.* Proc. 7th Workshop on Beam Cooling and Related Topics (COOL'09), Lanzhou, China, 8.-Sep. 2009, paper THPMCP005, pp. 138–141.

63. O. Boine-Frankenheim, V. Kornilov. *3D Simulation of Coherent Instabilities in Long Bunches Induced by the Kicker Impedances in the FAIR Synchrotrons.* Proc. 22nd Particle Accelerator Conf. (PAC'07), Albuquerque, NM, USA, Jun. 2007, paper FRPMN014, pp. 3919–3921.

64. O. Boine-Frankenheim, O. Chorniy. *RF Barrier Compression with Space Charge for the FAIR Synchrotrons.* Proc. 23rd Particle Accelerator Conf., Vancouver, Canada, May 2009, paper TH5PFP021, pp. 3236–3238.

65. T. Katayama, M. Steck, R. Maier, D. Prasuhn, H. Stockhorst. *Electron Cooling of Heavy Ions Interacting with Internal Target at HESR of FAIR.* Proc. 4th Int. Particle Accelerator Conf. (IPAC'13), Shanghai, China, May 2013, paper MOPEA017, pp. 103–105.

66. H. Stockhorst, R. Maier, D. Prasuhn, R. Stassen, T. Katayama. *Status of Stochastic Cooling Predictions at the HESR.* Proc. 2nd Int. Particle Accelerator Conf. (IPAC'11), San Sebastian, Spain, Sep. 2011, paper THPS003, pp. 3430–3432.

67. H. Stockhorst, B. Lorentz, R. Maier, D. Prasuhn, R. Stassen, T. Katayama. *Simulation Study of Heavy Ion Beam Injection and Acceleration in the HESR for Internal Target Experiments with Cooling.* Proc. 5th Int. Particle Accelerator Conf. (IPAC'14), Dresden, Germany, Jun. 2014, pp. 768–770.

68. V.B. Reva, M.I. Bryzgunov, V.V. Parkhomchuk, V. Kamerdzhiev, T. Katayama, R. Stassen, H. Stockhorst. *Experimental Observation of Longitudinal Electron Cooling of DC and Bunched Proton Beam at 2425 MeV/c at COSY*. Proc. 10th Workshop on Beam Cooling and Related Topics (COOL'15), Newport News, VA, USA, Sep.-Oct. 2015, paper MOX-AUD02, pp. 10–14.

69. C. Dimopoulou, B. Franzke, T. Katayama, D. Möhl, F. Nolden, G. Schreiber, M. Steck. *Experimental Demonstration of Longitudinal Ion Beam Accumulation with Electron Cooling*. Proc. 11th European Particle Accelerator Conf. (EPAC'08), Genoa, Italy, Jun. 2008, paper THPP048, pp. 3470–3472.

70. M. Frey, P. HÃ, H. Klingbeil, D. Domont-Yankulova, K. Gross, J. Harzheim. *Prototype Results of the ESR Barrier-Bucket System*. Proc. 8th Int. Particle Accelerator Conf. (IPAC'17), Copenhagen, Denmark, May 2017, pp. 4133–4135.

71. P. Spiller, K. Blasche, O. Boine-Frankenheim, B. Franczak, P. Hülsmann, G. Moritz, H. Reich-Sprenger, P. Schütt. *Double Synchrotron Complex SIS100/200 for a New Research Facility at GSI*. Proc. 8th European Particle Accelerator Conf. (EPAC'02), Paris, France, Jun. 2002, paper THPLE078.

72. M. Frey, R. Balß, C. Christoph, O. Disser, G. Fleischmann, U. Hartel, P. Hülsmann, S. Jatta, A. Klaus, H. Klingbeil, H.G. König, U. Laier, D.E.M. Lens, D. Mondry, K.-P. Ningel, H. Richter, S. Schäfer, C. Thielmann, T. Winnefeld, B. Zipfel, K. Groß, H. Klingbeil. *Status of the Ring RF Systems for FAIR*. Proc. 6th Int. Particle Accelerator Conf. (IPAC'15), Richmond, VA, USA, May 2015, pp. 2789–2791.

73. A. Lehrach, F. Hinterberger, B. Lorentz, G. Hansen, R. Greven, F. M. Esser, F. Klehr, K. Bongardt, R. Tolle, T. Bergmark, S. Johnson, T. Johnson, G. Norman, A. Raccanelli, E. Senicheva, K. Rathsman, O. Felden, R. Maier, B. Gålnander, T. Lofnes, M. Steck, R. Stassen, H. Stockhorst, D. Prasuhn, J. Dietrich, M. Schmitt, D. Reistad, T. Peterson, Y. Senichev. *HESR at FAIR: Status of Technical Planning*. Proc. 22nd Particle Accelerator Conf. (PAC'07), Albuquerque, NM, USA, Jun. 2007, paper TUPAN024, pp. 1442–1444.

74. B. Lorentz, A. Lehrach, R. Maier, D. Prasuhn, H. Stockhorst, R. Tölle. *HESR Linear Lattice Design*. Proc. 11th European Particle Accelerator Conf. (EPAC'08), Genoa, Italy, Jun. 2008, paper MOPC112, pp. 325–327.

75. R. Maier. *The High-Energy Storage Ring (HESR).* Proc. 24th Particle Accelerator Conf. (PAC'11), New York, NY, USA, Mar.-Apr. 2011, paper THOCN2, pp. 2104–2106.

76. R. Stassen, F. J. Etzkorn, G. Schug, H. Stockhorst, T. Katayama, L. Thorndahl. *RF and Stochastic Cooling System of the HESR.* Proc. 3rd Int. Particle Accelerator Conf. (IPAC'12), New Orleans, LA, USA, May 2012, paper MOPPD008, pp. 385–387.

77. H. Stockhorst, R. Maier, D. Prasuhn, R. Stassen, T. Katayama. *Feasibility Study of Heavy Ion Storage and Acceleration in the HESR with Stochastic Cooling and Internal Targets.* Proc. 4th Int. Particle Accelerator Conf. (IPAC'13), Shanghai, China, May 2013, paper MOPEA018, pp. 106–108.

78. P. Beller, K. Beckert, C. Dimopoulou, A. Dolinskii, F. Nolden, M. Steck, J. Yang. *Layout of an Accumulator and Decelerator Ring for FAIR.* Proc. 10th European Particle Accelerator Conf. (EPAC'06), Edinburgh, UK, Jun. 2006, paper MOPCH074.

79. F. B. Petrov, T. Weiland, O. Boine-Frankenheim. *Electron Cloud Effects in Coasting Heavy-ion Beams.* Proc. 2nd Int. Particle Accelerator Conf. (IPAC'11), San Sebastian, Spain, Sep. 2011, paper MOPS053, pp. 724–726.

80. R. Stassen, F. J. Etzkorn, R. Maier, D. Prasuhn, H. Stockhorst, L. Thorndahl. *COSY as Ideal Test Facility for HESR RF and Stochastic Cooling Hardware.* Proc. 23rd Particle Accelerator Conf. (PAC'09), Vancouver, Canada, May 2009, paper TU5PFP022, pp. 861–863.

81. H. Stockhorst, T. Katayama, R. Maier, D. Prasuhn, R. Stassen. *Stochastic Momentum Cooling Experiments with a Barrier Bucket Cavity and Internal Targets at COSY-Jülich in Preparation for HESR at FAIR.* Proc. 1st Int. Particle Accelerator Conf. (IPAC'10), Kyoto, Japan, May 2010, paper MOPD068, pp. 846–848.

82. R. Stassen et al. *Recent Results of the HESR RF System.* Proc. 5th Int. Particle Accelerator Conf. (IPAC'14), Dresden, Germany, Jun. 2014, pp. 2094–2096.

83. R. Gebel, R. Brings, O. Felden, R. Maier. *Activities at the COSY/Jülich Injector Cyclotron JULIC.* Proc. 19th Int. Conf. on Cyclotrons and their Applications, Lanzhou, China, Sep. 2010, paper MOPCP010, pp. 63–65.

84. T. Katayama, T. Kikuchi, R. Maier, I.N. Meshkov, D. Prasuhn, R. Stassen, H. Stockhorst. *Bunched Beam Stochastic Cooling at COSY.* Proc. 1st Int. Particle Accelerator Conf. (IPAC'10), Kyoto, Japan, May 2010, paper MOPD064, pp. 834–836.

85. A. O. Sidorin, A. D. Kovalenko, I. N. Meshkov, G. V. Trubnikov. *Project of the Nuclotron-Based Ion Collider Facility (Nica) at JINR*. Proc. 1st Int. Particle Accelerator Conf. (IPAC'10), Kyoto, Japan, May 2010, paper MOPD011, pp. 693–695.

86. T. Katayama, I. N. Meshkov, G. V. Trubnikov. *Numerical Investigation of Stochastic Cooling at NICA Collider*. Proc. 8th Workshop on Beam Cooling and Related Topics (COOL'11), Alushta, Ukraine, Sep. 2011, paper TUIOB01, pp. 52–57.

87. A. Smirnov, A. Sidorin, D. Krestnikov, R. Pivin, D. Prasuhn, M. Wolke. *Simulation of Pellet Target Experiments with Betacool Code*. Proc. 21st Russian Particle Accelerator Conf. (RuPAC'08), Zvenigorod, Russia, Sep.-Oct. 2008, paper MOAPH04.

88. O. S. Kozlov, A. V. Smirnov, V. Volkov, T. Katayama, A. O. Sidorin, G. V. Trubnikov, I. N. Meshkov, E. Kenzhbulatov, G. Y. Kurkin, A. V. Eliseev, V. M. Petrov. *Storage, Acceleration and Short Bunched Beam Formation of 197Au+79 Ions in the NICA Collider*. Proc. 23rd Russian Particle Accelerator Conf. (RuPAC'12), Saint Petersburg, Russia, Sep. 2012, paper MOBCH01, pp. 30–32.

89. A. V. Smirnov, I. N. Meshkov, A. O. Sidorin, G. V. Trubnikov, A. V. Eliseev, T. Katayama. *Stacking Modes with Barrier Buckets Method in NICA Collider*. Proc. 9th Workshop on Beam Cooling and Related Topics (COOL'13), Mürren, Switzerland, Jun. 2013, paper WEPPO02, pp. 97–99.

90. E. Syresin,A. V. Eliseev,N. V. Mityanina,V. M. Petrov,E. Rotov,A. V. Smirnov,A. G. Tribendis. *Longitudinal Particle Dynamics in NICA Collider*. Proc. 10th Int. Particle Accelerator Conf. (IPAC'19), Melbourne, Australia, May 2019, pp. 455–457.

91. T. Katayama, I. N. Meshkov, G. V. Trubnikov. *Beam Cooling at NICA Collider*. Proc. 23rd Russian Particle Accelerator Conf. (RuPAC'12), Saint Petersburg, Russia, Sep. 2012, paper TUYCH02, pp. 53–57.

92. N. V. Mityanina, I. N. Meshkov, V. M. Petrov,E. Rotov, A. O. Sidorin, E. Syresin, A. G. Tribendis. *Longitudinal Particle Dynamics and Cooling in NICA Collider*. Proc. 12th Workshop on Beam Cooling and Related Topics (COOL'19), Novosibirsk, Russia, Sep. 2019, pp. 64–67.

93. K. Takayama et al. *Induction Synchrotron (3): Rapid Cycle Synchrotron and Slow Cycle Synchrotron (Hardware Components for the Upgrade of KEK 12 GeV-PS)*. Proc. 19th Particle Accelerator Conf. (PAC'01), Chicago, IL, USA, Jun. 2001, paper RPPH028.

94. Y. Shimosaki, K. Horioka, K. Koseki, M. Nakajima, E. Nakamura, K. Takayama, K. Torikai, T. Toyama, M. Watanabe. *Specific Beam Dynamics in Super-bunch Acceleration*. Proc. 9th European Particle Accelerator Conf. (EPAC'04), Lucerne, Switzerland, Jul. 2004, paper WEPLT110.

95. K. Takayama, K. Koseki, K. Torikai, A. Tokuchi, E. Nakamura, Y. Arakida, Y. Shimosaki, M. Wake, T. Kouno, K. Horioka, S. Igarashi, T. Iwashita, A. Kawasaki, J. Kishiro, M. Sakuda, H. Sato, M. Shiho, M. Shirakata, T. Sueno, T. Toyama, M. Watanabe, I. Yamane. *Observation of the Acceleration of a Single Bunch by Using the Induction Device in the KEK Proton Synchrotron*. *Phys. Rev. Lett.* **94,** 144801 (14 Apr. 2005).

96. K. Takayama, Y. Arakida, T. Dixit, T. Iwashita, T. Kono, E. Nakamura, K. Otsuka, Y. Shimosaki, K. Torikai, M. Wake. *Experimental Demonstration of the Induction Synchrotron*. *Phys. Rev. Lett.* **98,** 054801 (5 Jan. 2007).

97. K. Takayama, D.A. Arakawa, Y.A. Arakida, K. Horioka, S. Igarashi, T. Iwashita, A.K. Kawasaki, J. Kishiro, T. Kono, K. Koseki, E. Nakamura, M. Sakuda, H. Sato, M.S. Shiho, Y. Shimosaki, M.J. Shirakata, T. Sueno, A. Tokuchi, K. Torikai, T. Toyama, M. Wake, M. Watanabe, I. Yamane. *Induction Acceleration of a Single RF Bunch in the KEK PS*. Proc. 21st Particle Accelerator Conf. (PAC'05), Knoxville, TN, USA, May 2005, paper FPAE020.

98. K. Takayama et al. *Present Status of the Induction Synchrotron Experiment in the KEK PS*. Proc. 10th European Particle Accelerator Conf. (EPAC'06), Edinburgh, UK, Jun. 2006, paper MOPCH119.

99. T. S. Dixit, Y. Shimosaki, K. Takayama. *Adiabatic Damping During Acceleration in the Induction Synchrotron*. Proc. 22nd Particle Accelerator Conf. (PAC'07), Albuquerque, NM, USA, Jun. 2007, paper FRPMN033, pp. 4009–4011.

100. K. Takayama. *Induction Synchrotron Experiment in the KEK PS*. Proc. 22nd Particle Accelerator Conf. (PAC'07), Albuquerque, NM, USA, Jun. 2007, paper TUXC02, pp. 836–840.

101. A. V. Smirnov, C. Dimopoulou, D.A. Krestnikov, I.N. Meshkov, R. Pivin, G. Schreiber, A.O. Sidorin, M. Steck. *Particle Accumulation with a Barrier Bucket RF System*. Proc. 7th Workshop on Beam Cooling and Related Topics (COOL'09), Lanzhou, China, 8.-Sep. 2009, TUM2MCIO02, pp. 67–70.

102. K. Torikai, Y. Arakida, Y. Shimosaki, K. Takayama. *Fully Digitized Synchronizing and Orbit Feed-back Control System in the KEK Induction Synchrotron*. Proc. 10th European Particle Accelerator Conf. (EPAC'06), Edinburgh, UK, Jun. 2006, paper THPCH094.

103. T. Iwashita, T. Adachi, K. Takayama, K. W. Leo, T. Arai, Y. Arakida, M. Hashimoto, E. Kadokura, M. Kawai, T. Kawakubo, T. Kubo, K. Koyama, H. Nakanishi, K. Okazaki, K. Okamura, H. Someya, A. Takagi, A. Tokuchi, M. Wake. *KEK digital accelerator. Phys. Rev. ST Accel. Beams* **14,** 071301 (7 July 2011).

104. R. Yamada, J. Kishiro, Y. Shimosaki, K. Takayama, T. Toyama, M. Wake. *62-TeV Center of Mass Hadron Collider with Capability for Super Bunch Beams*. Proc. 19th Particle Accelerator Conf. (PAC'01), Chicago, IL, USA, Jun. 2001, paper RPAH138.

105. K. Takayama, J. Kishiro, E. Nakamura, T. Toyama, S. Arakawa, K. Koseki, T. Hatano, K. Iida, Y. Imanishi, T. Sakuma, N. Shimizu, S. Naitoh, A. Tokuchi, K. Horioka, M. Nakajima, M. Watanabe, *Induction Accelerating Devices for Induction Synchrotrons and the Superbunch VLHC*. Proc. 8th European Particle Accelerator Conf. (EPAC'02), Paris, France, Jun. 2002, paper MOPRI075.

106. K. Takayama, R. J. Briggs. *Induction accelerators* (Springer, Berlin, 2011).

107. T. Bohl, T. Linnecar, E. Shaposhnikova. *Barrier Buckets in the CERN SPS*. Proc. 7th European Particle Accelerator Conf. (EPAC'00), Vienna, Austria, Jun. 2000, paper THP2A10.

108. Bohl, T and Linnecar, Trevor Paul R and Shaposhnikova, Elena. *Thick barrier buckets using the SPS travelling wave structures*. CERN, Geneva, SL-Note-2000-032-HRF, May, 2000.

109. R. Stassen, K. Bongardt, F. J. Etzkorn, A. Schnase, H. Stockhorst. *The HESR RF-system and Tests in COSY*. Proc. 11th European Particle Accelerator Conf. (EPAC'08), Genoa, Italy, Jun. 2008, paper MOPC125, pp. 361–363.

110. J. Harzheim, D. Domont-Yankulova, K. Gross, H. Klingbeil, M. Frey. *Input Signal Generation for Barrier Bucket RF Systems at GSI*. Proc. 8th Int. Particle Accelerator Conf. (IPAC'17), Copenhagen, Denmark, May 2017, pp. 3359–3362.

111. K. Gross, D. Domont-Yankulova, J. Harzheim, H. Klingbeil, M. Frey. *Test Setup for Automated Barrier Bucket Signal Generation*. Proc. 8th Int. Particle Accelerator Conf. (IPAC'17), Copenhagen, Denmark, May 2017, pp. 3948–3950.

112. B. Ashmanskas, S. U. Hansen, T. Kiper, D. W. Peterson. *FPGA-Based Instrumentation for the Fermilab Antiproton Source*. Proc. 21st Particle Accelerator Conf. (PAC'05), Knoxville, TN, USA, May 2005, paper RPAT009.

113. E. Bayer, P. Zipf, A. Klaus, H. Klingbeil, G. Schreiber. *Fast FPGA Based Low-Trigger-Jitter Waveform Generator Method for Barrier-Bucket Electronics at FAIR*. Proc. North American Particle Accelerator Conf. (NA-PAC'13), Pasadena, CA, USA, Sep.-Oct. 2013, paper THPMA01, pp. 1352–1354.

114. K. Koseki, M. Wake, K. Takayama. *Significance of isolation impedance in a solid-state power modulator. Nuclear Instruments and Methods in Physics Research Section A: Accelerators, Spectrometers, Detectors and Associated Equipment* **554,** 64–74. ISSN: 0168-9002 (2005).

115. M. Wake et al. *Switching Power Supply for Induction Accelerators*. Proc. 22nd Particle Accelerator Conf. (PAC'07), Albuquerque, NM, USA, Jun. 2007, paper MOPAN042, pp. 251–253.

116. K. Horioka et al. *Rapidly Switched Accelerating Devices for Induction Synchrotrons*. Proc. 7th European Particle Accelerator Conf. (EPAC'00), Vienna, Austria, Jun. 2000, paper TUP4A14.

117. W. Chou, J. Griffin, K. Y. Ng, A. Takagi, D. Wildman, H. Zheng. *Barrier RF Stacking at Fermilab*. Proc. 20th Particle Accelerator Conf. (PAC'03), Portland, OR, USA, May 2003, paper RPAG016.

118. W. Chou, A. Takagi, D. Wildman, H. Zheng. *Barrier RF System and Applications in Main Injector*. Proc. 21st Particle Accelerator Conf. (PAC'05), Knoxville, TN, USA, May 2005, paper FPAE010.

119. J. Dey, S. Dris, T. Kubicki, J. Reid. *Linearization of the Fermilab Recycler High Level RF*. Proc. 20th Particle Accelerator Conf. (PAC'03), Portland, OR, USA, May 2003, paper TPAB011.

120. J. Harzheim, D. Domont-Yankulova, K. Gross, H. Klingbeil, M. Frey, D. E. M. Lens. *The ESR Barrier-Bucket LLRF System - Design and First Results*. Proc. 9th Int. Particle Accelerator Conf. (IPAC'18), Vancouver, Canada, Apr.-May 2018, pp. 4964–4966.

121. J. Harzheim, D. Domont-Yankulova, H. Klingbeil, R. Königstein, M. Frey. *Modeling and Simulation of Broadband RF Cavities in PSpice*. Proc. 7th Int. Particle Accelerator Conf. (IPAC'16), Busan, Korea, May 2016, pp. 392–395.

122. V. I. Veksler. *A new method of acceleration of relativistic particles. J. Phys.* **9,** 153–158 (1945).

123. B. W. S. L. Montague. *Single-particle dynamics-RF acceleration*. CERN-1977-013.63 (1977).

124. S. Y. Lee. *Accelerator physics; 4th ed.* (World Scientific, Singapore, 2019).

125. G. Dôme. *Theory of RF acceleration and RF noise*. CAS - CERN Accelerator School : Antiprotons for Colliding-beam Facilities, CERN, Geneva, Switzerland, 11 - 21 Oct 1983, pp.215-253 (CERN-1984-015) (1984).

126. S. H. Strogatz. *Nonlinear dynamics and chaos: With applications to physics, biology, chemistry, and engineering* (Westview Press, Boulder, Colorado, 2015).

127. C. Lanczos. *The variational principles of mechanics; 4th ed.* (Dover, New York, NY, 1986).

128. H. Wiedemann. *Particle accelerator physics; 4th ed.* (Springer, Berlin, 2015).

129. CERN. *CERN Beam Longitudinal Dynamics code BLonD* Accessed: 07-07-2018. `http://blond.web.cern.ch`.

130. *IEEE Standard for Floating-Point Arithmetic. IEEE Std 754-2019 (Revision of IEEE 754-2008)* (2019).

131. J. L. Laclare. *Coasting beam longitudinal coherent instabilities*. `https://cds.cern.ch/record/398299` (1994).

132. M. Migliorati, S. Persichelli, H. Damerau, S. Gilardoni, S. Hancock, L. Palumbo. *Beam-wall interaction in the CERN Proton Synchrotron for the LHC upgrade. Phys. Rev. ST Accel. Beams* **16,** 031001 (3 Mar. 2013).

133. O. Boine-Frankenheim, I. Hofmann. *Space charge effects and coherent stability limits in barrier buckets. Phys. Rev. ST Accel. Beams* **6,** 034207 (3 Mar. 2003).

134. L. Wang, Y. Li. *Analysis of the longitudinal space charge impedance of a round uniform beam inside parallel plates and rectangular chambers. Phys. Rev. ST Accel. Beams* **18,** 024201 (2 Feb. 2015).

135. T. Schilcher. *RF applications in digital signal processing*. Accessed: 01-08-2019. `https://cds.cern.ch/record/1100538` (2008).

136. J. Tierney, C. M. Rader, B. Gold. *A Direct Digital Synthesizer*. IEEE Transactions on Audio and Electroacoustics, Vol. AU-19, NO.1., March 1971.

137. V. F. Kroupa (ed.) *Direct digital frequency synthesizers* (IEEE Press, 1999).

138. L. Sermeus, M. J. Barnes, T. Fowler. *The Kicker Systems for the PS Multi-turn Extraction*. Proc. 1st Int. Particle Accelerator Conf. (IPAC'10), Kyoto, Japan, May 2010, paper WEPD091, 3311–3313.

139. H. Schmickler. *Accelerator Controls Part 1: CERN Accelerator Controls* Accessed: 11/01/2020. `http://cas.web.cern.ch/sites/cas.web.cern.ch/files/lectures/divonne-2009/schmickler-1.pdf`.

140. S. Deghaye, E. Fortescue-Beck. *Introduction to the BE-CO Control System*. CERN-ACC-NOTE-2020-0069 (Dec. 2020).

141. T. Kikuchi, R. Maier, M. Steck, R. Stassen, H. Stockhorst, T. Katayama, D. Prasuhn, I. N. Meshkov. *Beam Accumulation with Barrier Voltage and Stochastic Cooling*. Proc. 1st Int. Particle Accelerator Conf. (IPAC'10), Kyoto, Japan, May 2010, paper MOPD065, pp. 837–839.

142. C. Lanczos. *Applied analysis* (Prentice-Hall, Englewood Cliffs, NJ, 1956).

143. R. Garoby. *Low level rf building blocks*. CERN-PS-91-44-RF, 31 p (1991).

144. B. E. Chase, B. Barnes, K. Meisner. *Digital Low Level RF Systems for Fermilab Main Ring and Tevatron*. 17th Particle Accelerator Conference, Vancouver, Canada, 12 - 16 May 1997, pp.2326.

145. T. Hayes, M. Harvey, G. Narayan, F. Severino, K.S. Smith, S. Yuan. *A High Performance DAC / DDS D8hter Module for the RHIC LLRF Platform*. Proc. 24th Particle Accelerator Conf. (PAC'11), New York, NY, USA, Mar.-Apr. 2011, paper MOP284, pp. 648–650.

146. M. Bousonville, J. Rausch. *Reference Signal Generation with Direct Digital Synthesis for FAIR*. Proc. 11th Int. Conf. on Heavy Ion Accelerator Technology (HIAT'09), Venice, Italy, Jun. 2009, paper A–01, pp. 218–222.

147. A. Caruso, L. Calabretta, G. Cosentino, A. Spartà, F. Speziale. *DDS-based Control Loops for the RF System at INFN - LNS*. Proc. 17th Int. Conf. on Cyclotrons and Their Applications, Tokyo, Japan, Oct. 2004, paper 20P23.

148. J. DeLong, J. M. Brennan, W. Fischer, T. Hayes, K. S. Smith, S. Valentino. *Synthesizer Controlled Beam Transfer from the AGS to RHIC*. Proc. 19th Particle Accelerator Conf. (PAC'01), Chicago, IL, USA, Jun. 2001, paper TPAH133.

149. X. Pei. *Longitudinal Rf Matching During AGS-RHIC Beam Transfer*. Proc. 15th Particle Accelerator Conf. (PAC'93), Washington D.C., USA, Mar. 1993, pp. 1424–1427.

150. T. Hayes, M. Harvey, G. Narayan, F. Severino, K. S. Smith, S. Yuan. *A High Performance DAC / DDS D8hter Module for the RHIC LLRF Platform*. Proc. 24th Particle Accelerator Conf. (PAC'11), New York, NY, USA, Mar.-Apr. 2011, paper MOP284, pp. 648–650.

151. J. Volder. *The CORDIC Computing Technique* in *Managing Requirements Knowledge, International Workshop on* **1** (IEEE Computer Society, Los Alamitos, CA, USA, 1959), 257.

152. H. Damerau, D. Perrelet. *Upgrade of the Beam-synchronous RF Source System in the CERN PS* Accessed: 19-07-2019. `https://public.cells.es/workshops/www.llrf2017.org/pdf/Posters/P-66.pdf`.

153. D. Perrelet, H. Damerau. *New CERN PS 10 MHz Cavity One-turn Feedback Hardware and Beam Tests* Accessed: 19-07-2019. `https://conferences.lbl.gov/event/27/session/23/contribution/21/material/poster/0.pdf`.

154. S. Persichelli, M. Migliorati, M. M. Paoluzzi, B. Salvant. Impedance Studies for the PS Finemet® Loaded Longitudinal Damper. Proc. 5th Int. Particle Accelerator Conf. (IPAC'14), Dresden, Germany, Jun. 2014, pp. 1708–1710.

155. S. Persichelli, M. Migliorati, M. M. Paoluzzi, B. Salvant. *Finemet cavity impedance studies*. CERN-ACC-NOTE-2013-0033.

156. J. Belleman. *WCM03 Installation* Accessed: 2017-09-11. `https://psring.web.cern.ch/psring/misc/wcm03.shtml`.

157. D. Belohrad. *Beam Charge Measurements. Conf. Proc.* **C11-05-16.4.** CERN-BE-2011-019, WEOC01. 5 p (May 2011).

158. T. P. R. Linnecar. *The high frequency longitudinal and transverse pick-ups in the CERN SPS accelerator. IEEE Trans. Nucl. Sci.* **26.** CERN-SPS-ARF-78-17, 3409–3411. 99 p (Aug. 1978).

159. R. Cappi, G. Cyvoct, J. Durant, M. Ruette, E. C. Schulte. *Single shot longitudinal shape measurements of nanosecond particle bunches*. CERN-PS-87-31-PSR, 4 p (Mar. 1987).

160. R. J. Steinhagen, S. Bart-Pedersen, J. Belleman, T. Bohl, H. Damerau. *Wall-Current-Monitor based Ghost and Satellite Bunch Detection in the CERN PS and the LHC Accelerators. Conf. Proc.* **C1204151.** CERN-ATS-2012-249, WEDP01. 4 p (Apr. 2012).

161. J. Belleman, W. Andreazza, A. Nosych. *A New Wall Current Monitor for the CERN Proton Synchrotron*. Proc. 5th Int. Beam Instrumentation Conf. (IBIC'16), Barcelona, Spain, Sep. 2016, pp. 143–146.

162. J. M. Belleman. *FT16.UES208* Accessed: 2020-09-26. http://jeroen.web.cern.ch/jeroen/tt2wbespu/ues208.shtml.

163. J. M. Belleman. *The TT2 Wideband Electrostatic Pick-Ups* Accessed: 2020-09-26. http://jeroen.web.cern.ch/jeroen/tt2wbespu/.

164. J. M. Belleman. *Pre-amplifier schematic diagram* Accessed: 2020-09-26. http://jeroen.web.cern.ch/jeroen/tt2wbespu/preampschematics.shtml.

165. J. M. Belleman. *A Four-Decade Bandwidth Hybrid Coupler*. AB-Note-2006-005. CERN-AB-Note-2006-005. CERN-PS-BD-Note-99-09 (Feb. 2006).

166. G. Sterbini. *LIU Toolbox*. Version 0.3. unpublished.

167. K. Wittenburg. *Beam loss monitors* Accessed: 2020-09-07. https://cds.cern.ch/record/1213279.

168. R.E. Shafer. *A tutorial on beam loss monitoring* https://ab-div-bdi-bl-blm.web.cern.ch/Beam_loss_detectors/Literature/schaefer_biw02_tutorial.pdf.

169. CERN. *Geant 4* Accessed: 2020-09-07. https://geant4.web.cern.ch/.

170. J. Allison et al. *Geant4—a simulation toolkit. Nuclear Instruments and Methods in Physics Research Section A: Accelerators, Spectrometers, Detectors and Associated Equipment* **506,** 250–303. ISSN: 0168-9002 (2003).

171. J. Allison et al. *Geant4 developments and applications. IEEE Transactions on Nuclear Science* **53,** 270–278 (2006).

172. J. Allison et al. *Recent developments in Geant4. Nuclear Instruments and Methods in Physics Research Section A: Accelerators, Spectrometers, Detectors and Associated Equipment* **835,** 186–225. ISSN: 0168-9002 (2016).

173. CERN. *FLUKA* Accessed: 2020-09-07. https://fluka.cern/about.

174. C. Zamantzas et al. *Injectors' BLM system: PS ring installation at EYETS* Accessed: 2020-09-08. https://indico.cern.ch/event/648710/contributions/2637394/attachments/1483809/2302429/20170627_LIU-PS_BLMINJ_EYETS.pdf.

175. E. Regenstreif. *The CERN Proton Synchrotron* doi:10.5170/CERN-1959-029 (CERN, Geneva, 1959).

176. H. Damerau et al. *LHC Injectors Upgrade, Technical Design Report, Vol. I: Protons* CERN-ACC-2014-0337. CERN-ACC-2014-0337 (Dec. 2014).

177. S. S. Gilardoni, S. Aumon, E. Effinger, J. Gil Flores, U. Wienands. *Beam Loss Monitors Comparison at the CERN Proton Synchrotron*. Proc. 2nd Int. Particle Accelerator Conf. (IPAC'11), San Sebastian, Spain, Sep. 2011, paper TUPC135, pp. 1341–1343.

178. V. Agoritsas, F. Beck, G.P. Benincasa, J. P. Bovigny. *A microprocessor-based system for continuous monitoring of radiation levels around the CERN PS and PSB accelerators. Nuclear Instruments and Methods in Physics Research Section A: Accelerators, Spectrometers, Detectors and Associated Equipment* **247,** 44–49. ISSN: 0168-9002 (1986).

179. W. Vigano, M. Alsdorf, B. Dehning, M. Kwiatkowski, G. G. Venturini, C. Zamantzas. *10 orders of magnitude current measurement digitisers for the CERN beam loss systems. Journal of Instrumentation* **9,** C02011–C02011 (Feb. 2014).

180. C. Zamantzas, M. Alsdorf, B. Dehning, S. Jackson, M. Kwiatkowski, W. Vigano. *System Architecture for measuring and monitoring Beam Losses in the Injector Complex at CERN.* Proc. 1st Int. Beam Instrumentation Conf. (IBIC'12), Tsukuba, Japan, Oct. 2012, paper TUPA09, pp. 347–350.

181. W. Vigano, B. Dehning, E. Effinger, G. G. Venturini, C. Zamantzas. *Comparison of Three Different Concepts of High Dynamic Range and Dependability Optimised Current Measurement Digitisers for Beam Loss Systems.* Proc. 1st Int. Beam Instrumentation Conf. (IBIC'12), Tsukuba, Japan, Oct. 2012, paper MOPA09, pp. 66–70.

182. S. Hancock, P. Knaus, M. Lindroos. *Tomographic Measurements of Longitudinal Phase Space Density; 1998 ed.* CERN-PS-98-030-RF, 4 p (July 1998).

183. G. Favia, H. Damerau, V.D. Desquiens, S. Energico, M. Morvillo, D. Perrelet, C. Rossi. *The PS 10 MHz High Level RF System Upgrade.* Proc. 7th Int. Particle Accelerator Conf. (IPAC'16), Busan, Korea, May 2016, pp. 622–625.

184. H. C. Grassmann, R. 1kovsky, W. Pirkl. *New RF system for the 28 GeV proton synchrotron at CERN. Siemens Rev.* **44,** 164–70 (1977).

185. CERN. *The CERN Experimental Programme* `https://greybook.cern.ch/greybook/` (2020).

186. W. Bartmann, J. Borburgh, S.S. Gilardoni, B. Goddard, A. Newborough, S. Pittet, R. Steerenberg, C.H. Yu. *CERN PSB-to-PS Transfer Modifications for the 2 GeV Upgrade.* Proc. 3rd Int. Particle Accelerator Conf. (IPAC'12), New Orleans, LA, USA, May 2012, paper MOPPD057, pp. 493–495.

187. W. Bartmann, J. Borburgh, J.R.T. Cole, S.S. Gilardoni, B. Goddard, O. Hans, M. Hourican, L. Sermeus, R. Steerenberg, C.H. Yu. *Upgrades for the CERN PSB-TO-PS Transfer at 2 GeV.* Proc. 4th Int. Particle Accel-

erator Conf. (IPAC'13), Shanghai, China, May 2013, paper MOPFI054, pp. 404–406.

188. L. Michelotti. *Integral for longitudinal phase space tomography on equilibrium distributions. Phys. Rev. ST Accel. Beams* **6,** 024001 (2 Feb. 2003).

189. G. Van Rossum, F. L. Drake. *Python 3 Reference Manual* ISBN: 1441412697 (CreateSpace, Scotts Valley, CA, 2009).

190. T. E. Oliphant. *A guide to NumPy* (Trelgol Publishing USA, 2006).

191. P. Virtanen et. al. *SciPy 1.0: Fundamental Algorithms for Scientific Computing in Python. Nature Methods* **17,** 261–272. `https://rdcu.be/b08Wh` (2020).

192. The pandas development team. *pandas-dev/pandas: Pandas* Feb. 2020. `https://doi.org/10.5281/zenodo.3509134`.

193. J. D. Hunter. Matplotlib: A 2D graphics environment. *Computing in Science & Engineering* **9,** 90–95 (2007).

194. M. Waskom and the seaborn development team. *mwaskom/seaborn seaborn.violinplot* Sept. 2020. `https://doi.org/10.5281/zenodo.592845`.

195. A. V. Oppenheim, R. W. Schaefer, J. R. Buck. *Discrete-time signal processing* (Upper Saddler River, NJ: Prentice Hall., 1999).

196. The SciPy community. *scipy.signal.resample_poly* Accessed: 2020-09-08. `https://docs.scipy.org/doc/scipy/reference/generated/scipy.signal.resample_poly.html`.

197. Julius O. Smith III. *Introduction to Digital Filters with Audio Applications* Accessed: 2020-09-08. `https://ccrma.stanford.edu/~jos/fp/Forward_Backward_Filtering.html` (Sept. 2007).

198. F. Gustafsson. *Determining the initial states in forward-backward filtering. IEEE Transactions on Signal Processing* **44,** 988–992 (1996).

199. The SciPy community. *scipy.signal.filtfilt* Accessed: 2020-09-08. `https://docs.scipy.org/doc/scipy/reference/generated/scipy.signal.filtfilt.html`.

200. The SciPy community. *numpy.correlate* Accessed: 2020-09-08. `https://numpy.org/doc/stable/reference/generated/numpy.correlate.html`.

201. A. Hofmann, F. Pedersen. *Bunches with Local Elliptic Energy Distribution.* Accessed: 01/08/2019. `https://cds.cern.ch/record/890555` (1979).

202. A. Lasheen. PS Longitudinal Impedance Model (2020). DOI:10.5281/zenodo.4420903 (Jan. 2021).

203. R. Garoby. *Timing aspect of bunch transfer between circular machines: State of the art in the PS complex*. CERN-PS-RF-Note-84-6 (1984).

204. W. A. Pellico, R. C. Webber. *RF Cogging in the FNAL Booster Accelerator*. Proc. 18th Particle Accelerator Conf. (PAC'99), New York, NY, USA, Mar. 1999, paper TUA13.

205. D. A. Herrup. *Cogging in the Fermilab Booster*. Proc. 18th Particle Accelerator Conf. (PAC'99), New York, NY, USA, Mar. 1999, paper TUA11.

206. R. M. Zwaska, S. E. Kopp, W. Pellico, R. C. Webber. *Synchronization of the Fermilab Booster and Main Injector for Multiple Batch Injection*. Proc. 9th European Particle Accelerator Conf. (EPAC'04), Lucerne, Switzerland, Jul. 2004, paper THPLT130.

207. R. M. Zwaska, S. E. Kopp, W. Pellico. *Cycle-to-Cycle Extraction Synchronization of the Fermilab Booster for Multiple Batch Injection to the Main Injector*. Proc. 21st Particle Accelerator Conf. (PAC'05), Knoxville, TN, USA, May 2005, paper FPAE022.

208. K. Seiya, C. C. Drennan, W. Pellico, A. K. Triplett, A. M. Waller. *Momentum Cogging at the Fermilab Booster*. Proc. 3rd Int. Particle Accelerator Conf. (IPAC'12), New Orleans, LA, USA, May 2012, paper THPPP023, pp. 3782–3784.

209. F. G. G. Garcia, W. Pellico. *Current and Planned High Proton Flux Operations at the FNAL Booster*. Proc. 52nd ICFA Advanced Beam Dynamics Workshop on High-Intensity and High-Brightness Hadron Beams (HB'12), Beijing, China, Sep. 2012, paper WEO3A04, pp. 378–380.

210. K. Seiya, S. Chaurize, C. C. Drennan, W. Pellico, A. K. Triplett, A. M. Waller. *Development of Cogging at the Fermilab Booster*. Proc. 5th Int. Particle Accelerator Conf. (IPAC'14), Dresden, Germany, Jun. 2014, pp. 2109–2111.

211. K. Seiya et al. *Beam Studies for the Proton Improvement Plan (PIP) - Reducing Beam Loss at the Fermilab Booster*. Proc. 6th Int. Particle Accelerator Conf. (IPAC'15), Richmond, VA, USA, May 2015, pp. 4027–4029.

212. K. Seiya, S. Chaurize, C. C. Drennan, W. Pellico. *Injection Bucket Jitter Compensation Using Phase Lock System at Fermilab Booster*. Proc. 8th Int. Particle Accelerator Conf. (IPAC'17), Copenhagen, Denmark, May 2017, pp. 1999–2001.

213. P. Baudrenghien, T. P. R. Linnecar, D. Stellfeld, U. Wehrle. *SPS Beams for LHC: RF Beam Control to Minimize Rephasing in the SPS*. CERN-SL-98-027-RF, 3 p (1998).

214. J. N. Bai, R. Baer, D. Beck, O.K. Kester, D. Ondreka, C. Prados, W.W. Terpstra, T. Ferrand. *Bunch to Bucket Transfer System for FAIR*. Proc. 15th Int. Conf. on Accelerator and Large Experimental Physics Control Systems (ICALEPCS'15), Melbourne, Australia, Oct. 2015, pp. 980–983.

215. P. Martin, J. Dinkel, R. J. Ducar, C. R. Kerns, Q. A. Kerns, K. G. Meisner, H. W. Miller, J. Reid, S. R. Tawzer, D. Wildman. *Antiproton acceleration in the Fermilab main ring and Tevatron*. 12th IEEE Particle Accelerator Conference, Washington, DC, USA, 16 - 19 Mar 1987, pp.47-49.

216. K. G. Meisner, H. Edwards, J. Fitzgerald, Q. A. Kerns. *A low level rf system for the Fermilab Tevatron*. 11th IEEE Particle Accelerator Conference, pt.1, Vancouver, Canada, 13 - 16 May 1985, pp.1687.

217. D. Trbojevic, L.A. Ahrens, M. Bai, M. Blaskiewicz, M. Brennan, P. Cameron, J. Cardona, R. Connolly, A. Drees, W. Fischer, R.P. Fliller, G. Ganetis, J.W. Glenn, H. Hahn, T. Hayes, J. Kewisch, A. Lehrach, W.W. MacKay, S. Peggs, V.I. Ptitsyn, T. Roser, T. Sa. *Commissioning of the Relativistic Heavy Ion Collider*. Proc. 19th Particle Accelerator Conf. (PAC'01), Chicago, IL, USA, Jun. 2001, paper RPAH124.

218. M. Meisner. *RF Synchronous Transfer Into Specific Buckets Between Fermilab Main Ring And Tevatron Accelerators*. 15th IEEE Particle Accelerator Conference, Washington, DC, USA, 17 - 20 May 1993, pp.2522.

219. J.M. Jowett, R. Alemany-Fernandez, P. Baudrenghien, D. Jacquet, M. Lamont, D. Manglunki, S. Redaelli, M. Sapinski, M. Schaumann, M. Solfaroli Camillocci, R. Tomas, J.A. Uythoven, D. Valuch, R. Versteegen, J. Wenninger. *Proton-nucleus Collisions in the LHC*. Proc. 4th Int. Particle Accelerator Conf. (IPAC'13), Shanghai, China, May 2013, paper MOODB201, pp. 49–51.

220. J.M. Jowett, R. Alemany-Fernandez, G. Baud, P. Baudrenghien, R. De Maria, R. De Maria, D. Jacquet, M.A. Jebramcik, A. Mereghetti, T. Mertens, M. Schaumann, H. Timko, M. Wendt, J. Wenninger. *The 2016 Proton-Nucleus Run of the LHC*. Proc. 8th Int. Particle Accelerator Conf. (IPAC'17), Copenhagen, Denmark, May 2017, pp. 2071–2074.

221. C. Bovet, R. Gouiran, I. Gumowski, K. H. Reich. *A selection of formulae and data useful for the design of A.G. synchrotrons; rev. version* (CERN, Geneva, 1970).

222. T. Ferrand, H. Klingbeil, H. Damerau. *Synchronization of Synchrotrons for bunch-to-bucket Transfers*. Sep. 2015, CERN-ACC-NOTE-2015-0025.

223. T. Ferrand, H. Klingbeil, O. Bachmann, J. N. Bai, H. Damerau. *Progress in the Bunch-to-Bucket Transfer Implementation for FAIR*. Proc. 8th Int. Particle Accelerator Conf. (IPAC'17), Copenhagen, Denmark, May 2017, paper THPVA041, pp. 4525–4527.

224. J. P. H., Sladen. *High Frequency Direct Digital Synthesizer and Clock Generator Modules*. CERN, Geneva, 2004, CERN-AB-Note-2004-046.

Appendix A

Synthesis using half revolution frequency harmonics

An alternative synthesis method using the basic symmetries of the barrier bucket pulses is presented. A property of such a pulse is a difference of two, phase shifted harmonic components at the half of the original harmonic frequency, which can be used to generate the pulses in the frequency domain.

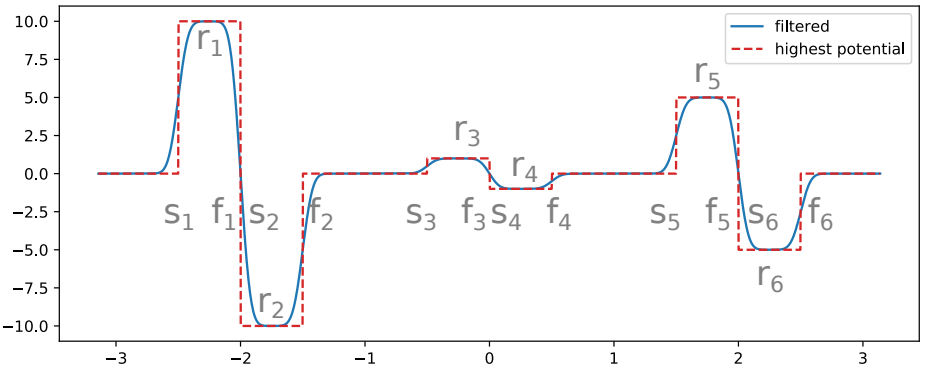

Figure A.1: s_i - start of the pulse, f_i - end of the pulse, r_i - the magnitude of the pulse

To derive the synthesis method, the notations of Fig. A.1 are going to be used. The Fourier coefficients for the i-th pulse in the pulse train can be found by direct integration:

$$c_0 = \frac{r}{\pi}(f_i - s_i) \quad c_{n,i} = \frac{rj}{n\pi}\left(e^{-jnf_i} - e^{-jns_i}\right) \tag{A.1}$$

To limit the amplitude of the higher harmonics, if this is needed, a low pass filter can be added, which in this case is the σ factor as also introduced in Chapter 3. The synthesizer formula for M pulses and N Fourier terms becomes:

$$V(t) = \sum_{i=1}^{M} \frac{r_i}{\pi} \left\{ f_i - s_i + j \sum_{n=1}^{N-1} \frac{\sigma_{n,m}}{n} \left[e^{jn(\omega t - f_i)} - e^{jn(\omega t - s_i)} \right] \right\} \tag{A.2}$$

The σ is defined as the following:

$$\sigma_{n,m} = \mathrm{sinc}^m \frac{n\ \pi}{2\,(N+1)} \tag{A.3}$$

A symmetric barrier consists of two bumps of equal height and equal width. Given s_0, f_0 and r_0 and the symmetry, s_1, f_1, r_1 are all uniquely determined.

$$s_1 = f_0 \quad f_1 = 2f_0 - s_0 \quad r_1 = -r_0 \tag{A.4}$$

To express the symmetry in the formula, introducing $b = f_0$ for the barrier centre and the barrier width as $w = 2(f_0 - s_0)$. Applying eq. A.2 the offset cancels.

$$V(t) = \frac{r}{\pi j} \sum_{n=1}^{N-1} \frac{\sigma}{n} \left[e^{jn(\omega t - b - \frac{w}{2})} + e^{jn(\omega t - b + \frac{w}{2})} - 2e^{jn(\omega t - b)} \right] \tag{A.5}$$

This is the same as:

$$V(t) = \frac{r}{\pi j} \sum_{n=1}^{N-1} \frac{\sigma}{n} \left[e^{jn\left(\frac{\omega}{2} t - \frac{2b-w}{4}\right)} - e^{jn\left(\frac{\omega}{2} t - \frac{2b+w}{4}\right)} \right]^2 . \tag{A.6}$$

Where w corresponds to the width of the barrier bucket generating waveform. The b corresponds to the azimuthal position. σ acts as a low-pass filter and ω is the revolution angular frequency, t the time, N the number of harmonic components.

The merit of this formula is that the Fourier coefficients do not have to be calculated, since the waveform is generated from two, clean complex exponentials. At the core of the waveform generator formula is a difference of two harmonics at the half of the Fourier harmonic frequencies. The Fourier harmonics correspond to the revolution frequency harmonics in a synchrotron. Therefore the fundamental, phase shifted barrier components are at the half of the revolution frequency. The revolution frequency harmonics are "restored" by squaring the components or mixing them with themselves. Then a smoothing window is applied. The process is illustrated in Fig. A.2.

An alternative implementation using whole revolution frequency harmonics can be achieved by grouping the terms in the bracket:

$$V(t) = \Im\left\{\frac{r}{\pi}\sum_{n=1}^{N-1}\frac{\sigma}{n}\left[e^{jn(\omega t-b)} - e^{jn(\omega t-b-\frac{w}{2})} + e^{jn(\omega t-b)} - e^{jn(\omega t-b+\frac{w}{2})}\right]\right\}. \tag{A.7}$$

The multiplication by $1/j$ and taking the negative of the imaginary part are interchangeable, hence the slightly different formalism in Eqs. A.7 and A.5.

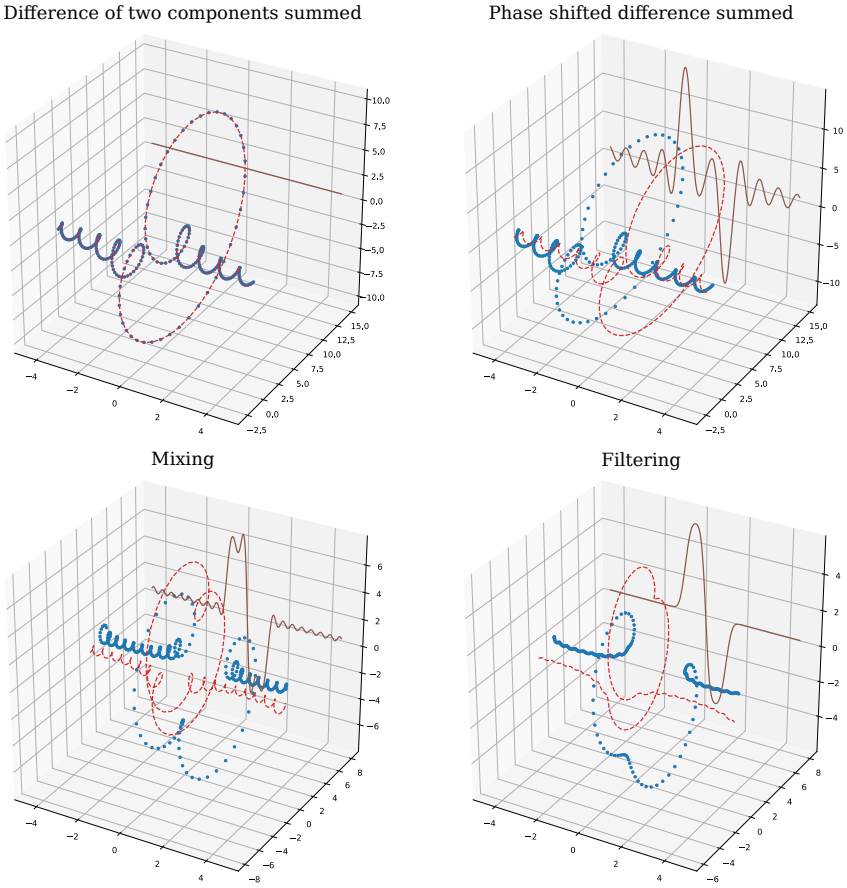

Figure A.2: The illustration of equation A.5. The sum is performed at each step to highlight the mechanism. The top left graph shows the difference of the two frequency components at half of the revolution frequency summed up on their own when there is no phase shift between them. The sum has only graphical significance, the components cancel individually and the result is zero. Then a phase shift in the half frequency components is introduced (top right) which makes a pair of pulses when the components are added. Then these components are squared and summed with the standard Fourier method (bottom left) and the modified or filtered version (bottom right) using the σ factors. It is clear from the formula and the images that the magnitude of the phase shift is the main factor in determining the width of the potential barriers.

Appendix B

Location of firmware and software

The GitLab repositories related to the PhD work are listed below for reference.

- Firmware for the FPGA: `https://gitlab.cern.ch/BE-RF-PLDesign/PS/EDA-02175-V2-BarrierBuckets`.
- Additional routines for barrier bucket generaion in Python: `https://gitlab.cern.ch/mivadai/barrierbucket`.
- Initial re-bucketing simulations: `https://gitlab.cern.ch/mivadai/BLonD`.
- The analytical calculations and simulations related to the synchronisation: `https://gitlab.cern.ch/mivadai/PSBBSynchronisation`.
- Accelerator related re-usable calculations, general helper routines: `https://gitlab.cern.ch/mivadai/mkit`.
- Versioned .svg diagrams: `https://gitlab.cern.ch/mivadai/diagrams`.